Investigation of Biological Flows through Particle Image Velocimetry (PIV) Combined With Several Imaging Techniques

by

Fazil Emre Uslu

A Thesis Submitted to the
Graduate School of Sciences and Engineering
in Partial Fulfillment of the Requirements for
the Degree of

Master of Science
in
Mechanical Engineering

January 18, 2017

To peace

ABSTRACT

Biological flows are important components of biological systems including cardiovascular, respiration or neural systems of species. Biological flows affect different systems by interacting with endothelial cells in vessels or receptor neurons in olfactory organ. In this thesis, four different biological flows are investigated. First one is hemodynamics in right vitelline artery (RVA) of chicken embryo. Second research is the investigation of suction and pumping flows at mussels. Third research is to explore suction feeding in zebrafish embryo. Last research is to investigate the effect of fluid dynamics on the olfaction of zebrafish embryo.

In first research, we investigated the role of hemodynamics forces on the developing cardiovascular system of chicken embryo. Furthermore, clinical experience suggests that perturbed flow disrupts the normal vascular growth process as one etiology for congenital heart diseases (CHD) and for fetal adaptation to CHD. However, the relationships between hemodynamics, gene expression and embryonic vascular growth are poorly defined due to the lack of concurrent, sequential *in vivo* data. In this study, a long-term, time-lapse optical coherence tomography (OCT) imaging campaign was conducted to acquire simultaneous blood velocity, pulsatile micro-pressure and morphometric data for 3 consecutive early embryonic stages in the chick embryo. In conjunction with the *in vivo* growth and hemodynamics data, *in vitro* reverse transcription polymerase chain reaction (RT-PCR) analysis was performed to track changes in transcript expression relevant to histogenesis and remodeling of the embryonic arterial wall. Our non-invasive extended OCT imaging technique for the microstructural data showed continuous vessel growth. OCT data coupled with the PIV technique revealed significant but intermitted increases in wall shear stress (WSS) between first and second assigned stages and a noticeable decrease afterwards.

For the suction and pumping performance of mussels, Hydrodynamic performance of marine mussel, Mytilus galloprovincialis, is studied with time-resolved particle image velocimetry. We evaluated inhalant flow, exhalant jet flow, suction performance, and flow control capabilities of the mussels quantitatively. Inhalant flow structures of mussels are measured at the coronal plane first time in literature. Nutrient fluid is convected into the mussel by three-dimensional sink flow. Inhalant velocity reaches its highest magnitude inside of the mussel mantle while accelerating outward the mussel. We calculated pressure gradient at the coronal plane. As inhalant flow approaches mussel shell tip, suction force generated by the inhalant flow increases and becomes significant at shell tip. Likewise, exhalant jet flow regimes are studied for 17 mussels. Mussels can control their exhalant jet flow structure from single potential core region to double one or vice versa. Peak exhalant jet velocity generated by the mussels changes between 2.77 cm/s and 11.1 cm/s as a function of mussel cavity volume. Measurements of hydrodynamic dissipation, at the sagittal plane, revealed no interaction between the inhalant and exhalant jet flow, indicating energy efficient synchronized pumping mechanism. This efficient pumping mechanism is associated with the flow-turning angle between inhalant and exhalant jet flows, ~90^o (s.d. 12^o).

In the third research, the hydrodynamics of suction feeding is investigated. Suction feeding is critical for the survival of fish larvae; failure to capture food during the onset of autonomous feeding can rapidly lead to starvation and mortality. Fluid mechanics experiments that investigate the suction feeding of suspended particles are limited to adult fishes, which operate at large Reynolds numbers. This manuscript presents the first literature results in which the external velocity fields generated during suction feeding of early zebra fish larvae (2500 to 20000 μm total length) are reported using time-resolved microscopic particle image velocimetry (μPIV). For the larval stages studied, the maximum peak suction velocity of the inflow bolus is measured at a finite distance from the mouth tip and ranges from 1 to 8 mm/s. The average pressure gradient and the velocity profile proximal to the buccal (mouth) cavity are calculated and two distinct trends are identified. External recirculation regions and reverse flow feeding cycles are also observed and quantified. One of the unresolved questions in fish suction feeding is the shape and dynamics of the buccal (mouth) cavity during suction feeding; optical coherence tomography (OCT) imaging is found to be useful for reconstructing the mouth kinematics. The projected area of the mouth cavity during the feeding cycle varies up to 160% and 22% for the transverse and midsagittal planes, respectively. These findings can inspire novel hydrodynamicaly efficient biomedical and microfluidic devices.

Olfaction system of zebrafish embryo is also subject of fluid dynamics. Neural cells and motile cilia on top of it cover olfactory organ of the embryos. Motile cilia generate flow around the nose of zebrafish embryo. In our research, we showed that spatially organized motile cilia beat asymmetrically and generated three-dimensional flow around nose. We also showed that the flow generated by motile cilia attracts odor to nose at stagnant environments. Our results showed that the flow improves the sensitivity and temporal resolution of olfactory computation.

ÖZETÇE

Biyolojik akışlar, kardiyovasküler, solunum veya türlerin sinir sistemleri dahil olmak üzere biyolojik sistemlerin önemli bileşenleridir. Biyolojik akışlar damarlarda endotel hücreleriyle veya koku organında reseptör nöronlarıyla etkileşerek farklı sistemleri etkiler. Bu tezde dört farklı biyolojik akış incelenmiştir. Birincisi, tavuk embriyosunun sağ vitellin arterindeki (RVA) hemodinamiktir. İkinci araştırma, midyelerde emme ve pompalama akışlarının incelenmesidir. Üçüncü araştırma, zebra balığı embriyosundaki emme yoluyla beslenmenin incelenmesidir. Son çalışma, akış dinamiklerinin zebra balığı embriyosunun koku alma ve sinir sistemi üzerine olan etkisini araştırmaktır.

İlk araştırmada hemodinamik kuvvetlerin tavuk embriyosunun gelişmekte olan kardiyovasküler sistemi üzerindeki rolünü araştırdık. Klinik deneyimler, pertürbe akışın normal vasküler büyüme sürecini konjenital kalp hastalıkları (CHD) ve CHD için fetal adaptasyon için etyoloji olarak bozduğunu düşündürmektedir. Bununla birlikte, hemodinamik, gen ifadesi ve embriyonik vasküler büyüme arasındaki ilişkiler, eşzamanlı, ardışık in vivo veri eksikliği nedeniyle zayıf olarak tanımlanabilmiştir. Bu çalışmada, tavuk embriyosunda 3 ardışık embriyonik evre için eş zamanlı kan hızı, pulsatil mikro basınç ve morfometrik veriler elde etmek için uzun süreli, zaman atlamalı optik koherens tomografi (OCT) görüntülemesi gerçekleştirildi. In-Vivo büyüme ve hemodinamik verilerle bağlantılı olarak, in vitro revers transkripsiyon polimeraz zincir reaksiyonu (RT-PCR) analizi, embriyonik arteryel duvarın histojenezi ve yeniden şekillendirilmesi ile ilgili transkript ekspresyonundaki değişiklikleri izlemek için gerçekleştirildi. Mikro yapısal veriler için invazif olmayan OCT görüntüleme tekniği ile damar büyümesi görüntülendi. OCT verileri PIV tekniğiyle birleştiğinde, birinci ve ikinci evreler arasındaki duvar kayma gerilmesinde (WSS) önemli artışlar olmakla birlikte engellendi ve daha sonra gözle görülür bir düşüş oldu.

Midyelerin emme ve pompalama performansı için, deniz midyesi, Mytilus galloprovincialis'in hidrodinamik performansı, parçacık görüntülemeli hız ölçümü ile incelenmiştir. Midyelerin giriş akışı, çıkış jet akışı, emme performansı ve akış kontrol mekanizmalarını nicel olarak değerlendirdik. Midyelerin giriş akış yapıları koronal düzlemde literatürde ilk kez ölçüldü. Besinleri de taşıyan giriş akışı, midye içine üç boyutlu akış içeren konveksiyonla gönderilir. Giriş akış hızı, midye dışında hızlanmaya başlarken, midye kabuğunun içinde en yüksek değere ulaşır. Aynı zamanda basınç gradiyentini koronal düzlemde hesapladık. Giriş akışı midye kabuğu ucuna yaklaştıkça, emme kuvveti artar ve kabuk ucunda önemli hale gelir. Ayrıca, çıkış jet akış rejimleri 17 midye için incelenmiştir. Midyeler, çıkış jet akış yapısını tek potansiyel çekirdeği bölgesinden çift bölgeye değiştirebilir. Midye tarafından üretilen en yüksek çıkış jet hızı, midye boşluğu hacminin bir fonksiyonu olarak 2.77 cm/s ile 11.1 cm/s arasında değişir. Hidrodinamik enerji kaybının sajital düzlemde ölçümü, giriş akışı ile çıkış jet akışı arasında hiçbir etkileşim olmadığını ortaya koydu; bu ölçüm, midyelerin enerji tüketimi açısından verimli ve senkronize pompalama mekanizmasına sahip olduğunu gösteriyor. Bu verimli pompalama mekanizması, giriş akışı ile çıkış jet akışı arasındaki akış dönüş açısı ile ilişkilidir. Bu açı yaklaşık olarak 90^o (s.d. 12^o)'dir.

Üçüncü araştırmada, zebra balığının emme yoluyla beslenmesinin hidrodinamiği araştırılmıştır. Emme yoluyla beslenme balık larvalarının hayatta kalması için kritik önem taşır; beslenme sırasında gıda yakalama esnasındaki başarısızlık hızla açlık ve ölüme neden olabilir. Emme yoluyla beslenmeyi araştıran akışkanlar mekaniği çalışmaları, büyük Reynolds sayılarındaki akışlarla beslenen yetişkin balıklarla sınırlıdır. Bu çalışmayla, zebra balığı larvalarının (2500 - 20000 μm toplam uzunluk) emme yoluyla beslenmesi sırasında oluşan dış akış yapıları mikroskobik parçacık görüntülemeli hız ölçümü (μPIV) kullanılarak literatürde ilk kez sunulmuştur. Maksimum emme hızı 1 mm/s ila 8 mm/s arasında değişir. Aynı zamanda ortalama basınç gradiyenti ve ağız boşluğuna yakın bölgedeki hız profili hesaplandı. Balıkların emme beslenmesindeki cevabı olmayan sorulardan biri olan, emme beslenme sırasında ağız boşluğunun şekli ve dinamiğini çalışmak için; Optik Koherens Tomografi (OCT) görüntülemenin ağız kinematiğini elde etme konusunda yararlı olduğu bulundu. Beslenme döngüsü boyunca ağız boşluğunun öngörülen alanının sırasıyla enine ve sajital düzlemler için % 162 ve % 22'ye kadar değiştiğini ortaya çıkardık. Bu bulgular hidrodinamik açıdan verimli biyomedikal ve mikro akışkan cihazlarının tasarımına ilham verebilir.

Zebra balığı embriyonunun koku alma ve sinir sistemi de akışkanlar dinamiğinin bir konusudur. Hareketli tüyler ve sinir hücreleri embriyoların koku organının en üst tabakasında yer alır. Hareketli tüyler,

zebra balığı embriyonunun burnunun etrafında akış oluşturur. Araştırmamızda, asimetrik olarak çalışan tüylerin burun çevresinde üç boyutlu akış oluşturduğunu gösterdik. Ayrıca, hareketli tüyler tarafından üretilen akışın durgun ortamlarda burun kokusu çektiğini gösterdik. Sonuçlarımız, akışın sinir sisteminin gerçekleştirdiği hesaplamanın hassasiyetini ve zamansal çözünürlüğünü geliştirdiğini gösterdi.

ACKNOWLEDGEMENTS

I would like to acknowledge my advisor, Dr. Kerem Pekkan for his precious support and assistance over the course of graduate studies.

I would like to thank my father, mother, and brother for their precious life-time support. My lovely thanks goes to Ece for her invaluable support and patience during my studies.

I would like to thank all of my lab mates for their assistance during my thesis work and great time out of research. I also like to thank my close friends from “Saddening Grads” group for their mental and academic support.

I would like to thank European Research Council (ERC) for scholarship provided.

Also, I would like to thank Graduate School of Science & Engineering, Koç University for their administrative and logistical support.

Table of Contents

List of Figures

List of Tables

List of Abbreviations

CBF	Ciliary Beating Frequency
CCD	Charged-Coupled Device
HH	Hamilton Hamburger
IPA	Isopropyl Alcohol
MCC	Multiciliated Cells
OCT	Optical Coherence Tomography
ORN	Olfactory Receptor Neurons
PC-MRI	Phase Contrast Magnetic Resonance Imaging
PIV	Particle Image Velocimetry
RBC	Red Blood Cell
Re	Reynolds Number
RVA	Right Vitelline Artery
sCMOS	scientific Complementary Metal-Oxide-Semiconductor
WSS	Wall Shear Stress

Chapter 1. Introduction

Biological flows have important impact on biological systems of species in nature. The biological flow might be blood flow in cardiovascular system, suction flow of water in respiratory system, or water flow affecting the neural system of an animal. By studying biological flows, we can explore the evolutionary rules of nature. Other important aspect of studying biological flows is to inspire designs in nature for constructing engineering products.

1.1. Hemodynamics in Cardiovascular System of Chicken Embryo

Cardiovascular systems of embryos are crucial to study. We can explain the reasons of congenital heart diseases and find treatment by studying cardiovascular system of chicken embryo as a model. Blood flow influences the cellular signaling during the development of cardiovascular system of the embryo[1]. Blood flow generates Wall Shear Stress (WSS) at the vessel walls and endothelial cells are affected by WSS [2]. Different quantitative methods to study hemodynamics in cardiovascular system is applied in past [3, 4]. Poelma et al. studied hemodynamics of developing vascular networks in chicken embryo by using μ-PIV and they compared two different methods to calculate WSS in vascular networks [4]. In their following study, they also used red blood cells (RBCs) as PIV particles and found similar WSS values with previous μ-PIV study [5]. Optical coherence tomography (OCT) is also good instrument for non-invasively imaging the vascular network of embryos [6, 7]. Chen et al. developed a novel methodology by combining OCT and particle image velocimetry (PIV) [8]. In all of the studies, genetic expressions, vascular growth, and hemodynamics were not simultaneously studied. We simultaneously studied genetic expressions, vascular growth, and hemodynamic in right vitelline artery (RVA). We explored the complex interactions between hemodynamics and genetic responses of cardiovascular cells.

1.2 Suction Feeding and Pumping in Mussels and Zebrafish Embryo

Mussels have unique pumping mechanisms. They efficiently filter large amount of water during feeding and pumping[9-11]. Mussels have cilia networks in their shell and they are classified as hydrodynamic pumps[12]. As an important element of suction feeding, many studies were conducted about cilia networks inside mussels[13, 14]. Seo et al. studied water circulation generated by cilia networks inside the mussel shells by using PC-MRI[15].

On the other hand, mussels generate unique external flow structures, which is the subject of our research. PIV was applied to explore external flow structure of different bivalves by Frank et al. [16]. Troost et al. also studied inhalant flows generated by three different suspension feeders[17], but they did not studied exhalant flows. Riisgård et al. studied exhalant flow in detail without studying inhalant flow[18]. Previous studies did not examine the possible interactions between inhalant and exhalant flows. We hypothesized that investigating the interaction between the flows is important. Then we conducted PIV experiments in multiple planes including sagittal plane and coronal plane. At sagittal plane, we visualized exhalant flow and inhalant flows together. Then we visualized inhalant flow in coronal plane for the first time in the literature. We measured flow-turning angle in sagittal plane and found that there is 90^{o} angle between inhalant and exhalant flows. For the possible interaction, we calculated the energy dissipation rate in sagittal plane and did not detect any interaction, which may be the reason for efficient suction feeding of mussels.

Suction feeding is also an important phenomenon for zebrafish embryos. Mortality rates are high in zebrafish embryos even though they live in an environment with abundant food. Previous studies suggest that high mortality rates may be result of hydrodynamic regimes where the embryos dwell[19-21]. Embryos generate flow to capture their prey. The suction flow is

generated by the buccal (mouth) expansion of their mouth[20, 21]. Suction flow is visualized for adult fishes in previous studies[22]. Suction flow is found to be unsteady measured as more than 3 m/s[23, 24]. Reynolds number (Re) is measured as lower than 100. There is no study investigating suction flow of zebrafish embryos. To explore the details of low Re suction flow of the embryos, we used high-speed microscopic visualization system to capture the images of prey (PIV particles) and calculate velocity. At the same time, we visualized buccal cavity with OCT.

1.3. Role of fluid dynamics in olfaction

Cilia cover body surfaces of most of the vertebrates [25]. Motile cilia beat and generate directional flows. These flows are critical for sensory organs[26]. The flows have several functions on different systems. Cilia mediated flow delivers the nutrient and signaling molecules in brain ventricles [27]. Also protective mucus and clearance of toxic substances are controlled by cilia-mediated flow [28]. But we still do not know cilia-mediated flow generated by motile cilia located on the surface of nose. In our study, we used several imaging techniques including confocal microscopy, ligh-sheet microscopy and two photon microscopy to investigate the function of cilia-mediated flow in olfaction. We compared fluid mechanics results and neurol cell responses to explore the function of the flow.

Chapter 2. Characterization of pulsatile wall shear stress at the vitelline artery during early embryonic development

2.1. Introduction

Embryonic blood vessel development (vasculogenesis and angiogenesis) is regulated through continuous synthesis and remodeling processes. Inter- and intra-cellular signaling, under the influence of blood flow, regulates vascular microstructure and regenerative cascade of events, and thus the morphogenetic fate for the embryonic vessel network through genetic pathways [1]. The key regulatory processes are greatly influenced by changes in hemodynamic loading on the great arteries and veins, as well as by the growth factors that are important in arterial and venous differentiation [29, 30]. The genetic coding during embryonic vasculogenesis is controlled mostly by the endothelial cells, which respond to mechanical stimuli through various adaptive mechanisms depending on their vascular origin [31]. As a consequence, the arteries exhibit their unique identity during development compared to the veins [32].

In the early embryonic vasculature system, newly-formed endothelial cells are under the influence of blood shear stress and circumferential stress as physiological mechano-regulatory stimuli [2]. It is well known that cells react differently to these orthogonal forces [33]. It is crucial to choose appropriate imaging modality for visualization of vessels. One of the most useful modalities for embryonic cardiovascular biology studies is the optical coherence tomography (OCT), which enables non-invasive visualization of the vessels to 1-2 mm depth without the use of fluorescent markers, *in ovo* [6, 7]. Besides its superior capability in locating and quantifying the vascular structures, *in vivo* real-time OCT imaging technology has recently gained momentum in

detecting the developmental malformations instead of routine and tedious pathological analyses [34]. When coupled with particle image velocimetry (PIV), OCT technique can yield the hemodynamics data for the normal and disturbed cardiac flows due to diseased state with high sensitivity [8].

Besides the 3D visual tracking of morphogenetic formations and deformations in early embryonic cardiovascular systems using OCT methodology, several attempts have been made to investigate the normal blood flow properties and their proximal relation to other morphogenetic parameters. In one of those studies, hemodynamics of fetal great arteries in mice was quantified through computational fluid dynamics (CFD) simulations, and it was seen the vessel size and flow-induced shear loading varied for different gestational periods [35]. It is also known that the altered hemodynamics within the microcirculation system causes changes in the genetic mechanisms in the developing embryos [36, 37].

Morphometric cues are dependent on intimate interplay among gene regulatory networks, flow-induced forces and the vascular growth mechanisms. Although it is difficult to draw direct implications between these factors, correlative scenarios may be of significant importance. Using chick embryo as model system, an OCT-based particle image velocimetry (PIV) system was used to obtain the hemodynamic parameters in the right vitelline arteries (RVAs). The flow- and growth-induced remodeling of the RVAs were investigated at three distinct embryonic stages, where rapid morphological changes were expected to occur. Here, we aim to unravel the complex interactive relations between the genetic response of the early embryonic cardiovascular cells and concurrent vessel growth under normal morphogenesis conditions.

2.2. Material and Methods

2.2.1. Optical coherence tomography imaging and morphometric analysis of embryos

An optical coherence tomography (OCT) system (Thorlabs Spectral Domain Ganymede, Thorlabs, Inc., NJ), enclosed in a custom-built environmental chamber maintained at 37°C and 60% humidity, was used for imaging and 3D reconstruction of the vascular RVA lumen *in ovo* as previously described [38]. During the time-lapsed experiments, embryos were continuously imaged through a 12 bit high-sensitivity CCD camera attached to the system.

We acquired 2D single-time-point OCT images at HH16, 17.5, and 19 for additional radius measurements at these three stages. A long-axis view at the center of the vessel was used and we took 10 radius measurements per RVA. A total of n = 15 embryos were measured per stage. Measurements were normalized to the mean HH16 value for analysis.

2.3. Assessment of hemodynamics parameters

2.3.1. Velocity Profiles

Images obtained by time-resolved OCT-particle image velocimetry (PIV) technique were used to evaluate velocity profiles within the right vitelline arteries at stages HH16, HH17.5 and HH19 [8, 39]. Velocity data was extracted with DaVis 8.1.0 software (LaVision, Inc., Germany). Single frames taken at the center of the vessels were acquired with OCT technique and time series of single frames PIV algorithm was used as the vector calculation method. The vessel region was manually traced and a mask was applied to constrain vector calculation. Smoothing was applied to improve the vectors. Poor neighboring vectors were removed if greater than the 2 root mean square (RMS) magnitude and multi-pass post-processing median filtering was reinserted for vectors less than 3 RMS of neighboring vectors [8]. A multi-pass interrogation window was used with decreasing size. The size of the first interrogation window was 128x128 pixels with 50% overlap (1 pass), and the size of the second interrogation window was 48x48 pixels with 75% overlap (2 passes). During the vector post processing, median filter was applied.

2.3.2. Wall Shear Stress Calculation

Blood flow data were collected at different frame speeds for each embryo: 200 frames at 67 frames per second (fps), 200 frames at 55 fps, and 100 frames at 33 fps including 6-7 cardiac cycles. Data sets with 67 fps were used for hemodynamics calculations. Each cardiac cycle included approximately 25 time points. Mean velocities of the time points were acquired by averaging the velocity vector distribution. Phase-locked averaging was performed over each time series to obtain a single cardiac cycle per embryo. The same procedure was applied for the 55 fps and 33 fps data to validate results obtained from the cardiac cycle at 67 fps.

Mean peak wall shear stress (WSS) for each stage was calculated from phase-locked averages of cardiac cycles at each stage (n = 5). The flow in the vessels was laminar and possessed Poiseuille flow profile in each frame of the data used for analyses. Mean peak velocities of phase-locked averages of cardiac cycle for each stage were used as V_{mean} for the calculation of the peak WSS values. Dynamic viscosity values used during peak WSS calculations were extracted from literature [40]. Fluctuations in the cardiac cycles were investigated via calculating percentage backflow and Oscillatory Shear Index [41].

2.4. Results

2.4.1. Mechanical Loading in the RVA

The supplementary file in S1 Movie demonstrates the pulsatile nature of the blood flow within the chick embryonic RVAs. The pulsatile phase-locked cardiac cycle at HH17.5 is shown in Fig 3, where the time points are the average of velocity magnitudes of parabolic flow profile and variations in mean velocities are presented at each phase-locked time point in the cardiac cycle. Negative back flow was observed in all embryos (12%, 3.64%, and 5.29% backflow for HH16,

HH17.5, and HH19, respectively). It was seen that the mean velocity values mostly deviated when forward pumping of the embryonic heart has started. The peak velocity region of forward flow (positive velocity field of cardiac cycle) remained at around 2 mm/s for approximately 0.12 seconds.

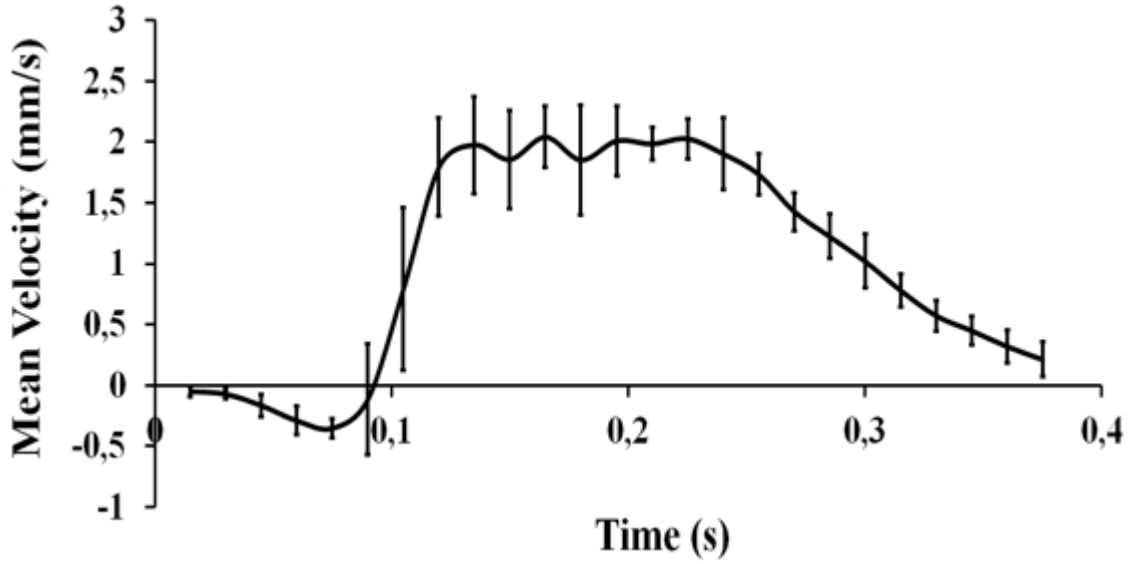

Figure 2.1. Representative phase-locked average of a cardiac cycle at stage HH17.5 (n = 5). Cardiac cycles are composed by average velocity values of velocity field at 25 time points whose standard deviations are depicted with error bars.

The cardiac period at HH16 was 0.46 ± 0.01 s, which then decreased significantly towards HH17.5 (0.39 ± 0.02 s), and remained almost unchanged afterwards. There were no significant changes in OSI between the stages (data not shown for brevity). The peak WSS increased significantly from HH16 to HH17.5 (p = 0.0004), and decreased significantly from HH17.5 to HH19 (p = 0.007) (Fig 4A). Likewise, the mean right vitelline arterial pressures for stages HH16, HH17.5 and HH19 were recorded as 2.87 ± 0.15 mmHg, 3.59 ± 0.22 mmHg, and 3.72 ± 0.15 mmHg, respectively (n = 4). The pressure increase from embryonic stage HH16 to HH17.5 was significant (p = 0.013) (Fig 4B).

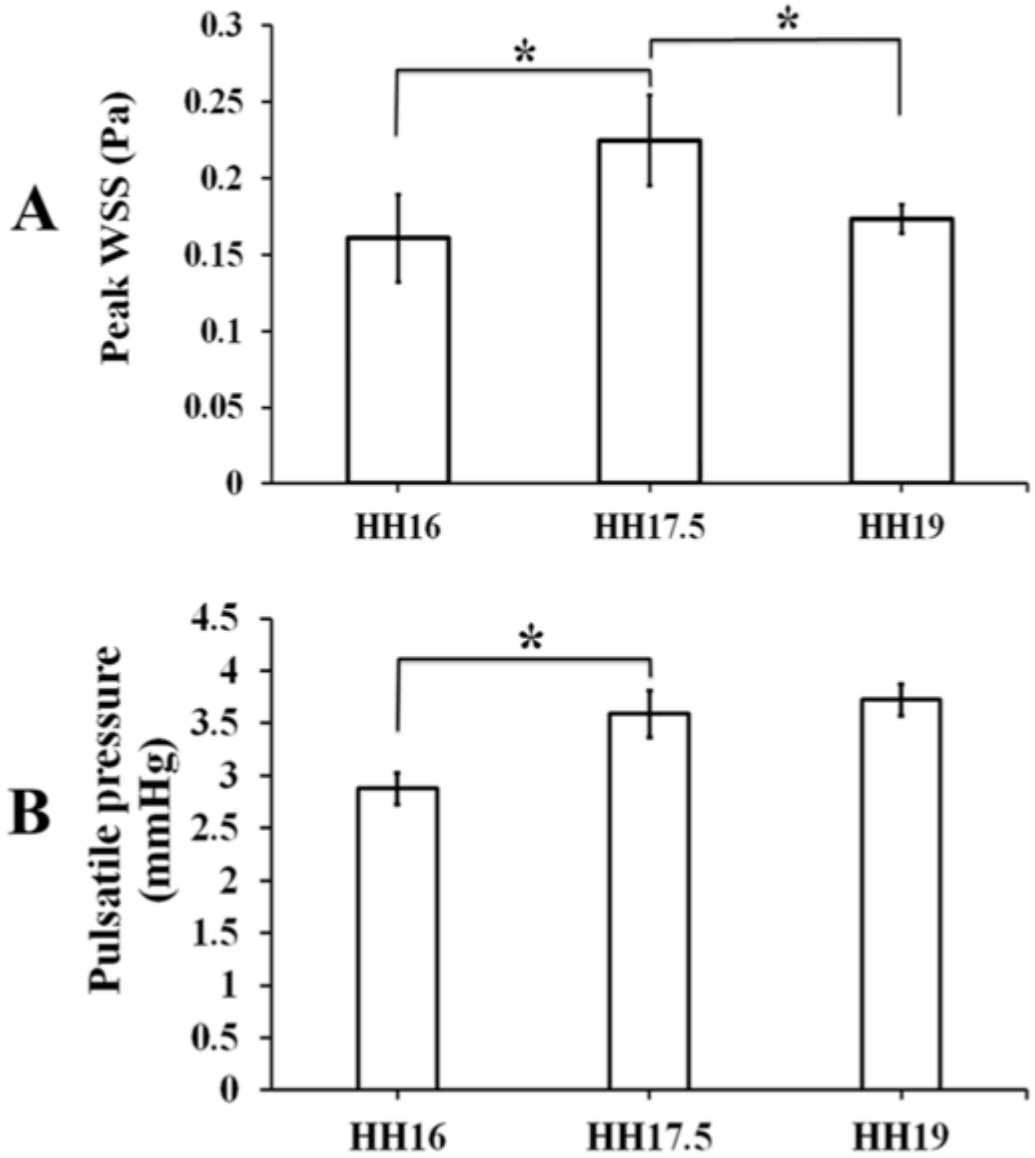

Figure 2.2. (A) Wall shear stress (WSS) values reached within the right vitelline arteries at stages HH16, HH17.5 and HH19 (n = 5). (B) The mean pulsatile blood pressure values measured for the right vitelline artery vessels at stages HH16, HH17.5 and HH19. Solid circumferential stress is known to be directly proportional with pressure values. The mean pressure, thus the circumferential stress values, increased significantly towards HH17.5, then remained insignificantly changed when HH19 was reached (n = 4). * denotes statistically significant differences ($p < 0.05$).

2.5. Discussion

Various approaches to quantify the flow parameters in the chick embryo have made it a valuable model to explore vasculogenesis and angiogenesis relevant to humans [42-44]. While the majority of our results are consistent with previous studies, a few proved to be contradictory.

It was reported earlier that the steady laminar flow was not achieved in the early chick embryo before stage HH12 and the flow demonstrated backflow and mixing until then [45]. However, the flow measurements extracted from our PIV processing methodology showed 12% backflow for stage HH16, then less backflow in blood stream at stage HH17.5, and further less for stage HH19. This was indicative of the continuity of fluctuations and unsteady flow profiles in blood flow until later stages than HH12.

The individual time-lapsed hourly growth curves consistently show a general increasing trend and the rate of change in vessel radius of the RVAs remained nearly constant throughout the growth period. However, a significant difference in RVA radius was not observed from 2D measurements of a larger sample size possibly due to the accuracy of OCT. Note that the steady growth rate, is a "slope calculation" based on "multiple" time-points whereas the diameter measurements are obtained for one single instant during development. Furthermore, the increase in blood velocity and shear stress values along the vessel towards stage HH17.5, and the subsequent decrease may not be at critical levels to generate a growth response [46]. In addition, at these early embryonic stages, there may be an intrinsic stimulus for vascular growth, mitigating any biomechanical response to changes in shear stress.

Chapter 3. Mytilus Galloprovincialis as a smart micro-pump

3.1. Introduction

Suspension-feeding bivalves filter large volumes of water very efficiently through a variety of biological pumping and feeding characteristics [10, 13, 47-52]. Among many alternative pumping configurations employed by the bivalves, mussels are classified as "hydrodynamic pumps" due to their organized ciliary network and synchronized microscopic beating patterns [12]. For example, the low Reynolds (Re) number particle retention mechanism of *Mytilus Edulis* (blue mussel) is shown to be critical for internal flow performance [11, 53].

Ciliary structures of mussel gills have an important biological function, which is to generate flow circulation inside the mussel cavity. The internal flow is generated by the lateral cilia located at interfilament canals [15]. Propulsion characteristics of cilia have been studied to understand how flow through the interfilament canals and frontal surface currents are generated at the micro-scale. Latero-frontal cilia located at the entrance of the interflament canals can retain particles that are above 4 μm diameter [13]. Separated particles are sent to surface currents generated by frontal cilia[53]. Frontal surface currents take the particles separated by latero-frontal cilia to the nutrient groove [14]. While several research groups investigated the morphology and evolution of mussel gills in order to understand the flow mechanics through the interflament canals and frontal surface currents [54-58], these studies lacked real-time flow measurements. This present study is unique in that it visualized and quantified the velocity field at the coronal plane during suction feeding through a particle image velocimetry technique. As such, artificial cilia models were employed to understand the contribution of individual cilia to the flow circulation [59, 60]. As highlighted in the present study, the ciliary propulsion mechanism of mussel gills is also crucial for the generation of

external inhalant suction and the exhalant jet flow regimes.

In addition to the internal flow performance, the external flow structures generated proximal to the bivalve mantle is hypothesized to be equally critical for the long-term sustained flow efficiency, non-interacting and simultaneously generated inhalant and exhalant jet flows without excessive hydrodynamic energy dissipation. The mantle shape, exhalant and inhalant siphons are the major functional components influencing the external flow performance. In earlier "qualitative" investigations, using dyes as flow tracers, streamlines generated by the siphon components were visualized [61, 62]. In a quantitative study, Frank, Ward [16] employed PIV to compare the external velocity fields generated by five different bivalve suspension feeders without studying inhalant flow and its interaction with the exhalant jet. Likewise, Troost, Stamhuis [17] only investigated inhalant flow fields created by three suspension feeders and presented detailed inhalant velocity field information through PIV. For the exhalant flow side, Riisgård, Jørgensen [18] presented flow measurements focusing on the exhalant flow of *Mytilus Edulis,* but without including detailed analyses on inhalant flow as performed in the present study. We hypothesized that the interaction between inhalant flow and exhalant jet is important; we thus conducted the present experimental campaign to investigate the degree of external flow interaction between inhalant and exhalant flow streams. To evaluate if any flow interaction exists, we studied exhalant jet flow and inhalant flow simultaneously through multiple measurement planes.

In summary, previous investigations that focused on suspension feeders did not study the jet flow angle between the inhalant and exhalant flow, which is hypothesized to be important for efficient feeding. To our knowledge, this is also the first literature to suggest that the mantle shape may be important for the optimal inflow and exit flow; to investigate this we acquired flow fields at multiple planes. Furthermore, we studied how mussels can dynamically change their exhalant jet flow type over time to demonstrate the tremendous changes in shape and maximum velocity values

of the exhalant jet flow.

3.2. Materials and Methods

3.2.1. Experimental set-up

The Mediterranean mussel, *Mytilus Galloprovincialis* is adopted as a model organism because it is a good representation of the genre and is locally available. Mussels were cultured in a custom aquarium (15 x 40 x 30 cm) containing seawater within 15 minutes after collecting them from the Bosphorus Strait (Istanbul, Turkey) from 6-10 m depth. Mussels were not subjected to any cross-flow in the experimental chamber, which was located on a vibration-isolated table. Exhalant and inhalant flow characteristics of mussels are presented in an inert water environment. We performed experiments in fresh and natural seawater collected from where mussels live. While mussels stay in our experiment chamber in their natural fresh water for a brief period, we verified their viability and performed qualitative filtration rate tests by using organic particles and micro planktons before PIV experiments. PIV experiments were performed when mussels pump water at the maximum filtration rate. We rarely observed coughing and excessive pulsatile jets but these cases were not included in our results and analyses. Experiments were performed on 17 mussels of different sizes. Mussels were released back into the ocean after completing the experiments. The mussels' cavity volumes range from 7 cm^3 to 34 cm^3 and the mussels' shell lengths range from 4.88 cm to 7.58 cm.

A cartoon representation of the experimental set-up is sketched in Fig. 3.1. A shuttered continuous wave laser (LaVision GmbH, Gottingen, Germany) with 1W output power was used as the laser source at 532 nm wavelengths. Laser guiding arm optics were used to direct the laser to the intended positions and the location of the endpoint of the arm was adjusted through translational stages. A LaVision Imager sCMOS camera (LaVision GmbH, Germany), which is synchronized with the laser, was used to record PIV images using double frame mode. We used

Fluoro-Max Dyed red fluorescent polymer microspheres (Thermo Fisher Scientific Inc., Massachusetts) with a diameter of 3.2 μm for the PIV experiments performed in the sagittal plane. Fluoro-Max Dyed red fluorescent polymer microspheres (Thermo Fisher Scientific Inc, Massachusetts) with diameter of 1 μ were used for PIV experiments in the coronal plane due to smaller field of view (FOV) and higher magnification. Laser pulse separation between 8000 μs and 14000 μs was applied, depending on the FOV.

A mussel alignment apparatus was produced in-house from plexiglass with the purpose of aligning the mussel accurately on the laser plane and stabilizing the mussel in its native configuration (Fig. 3.1). Mussels were adjusted with an external magnet to precisely align their exhalant and inhalant siphons with a planar (1x1 mm) squared grid that is employed for focusing the camera and PIV calibration.

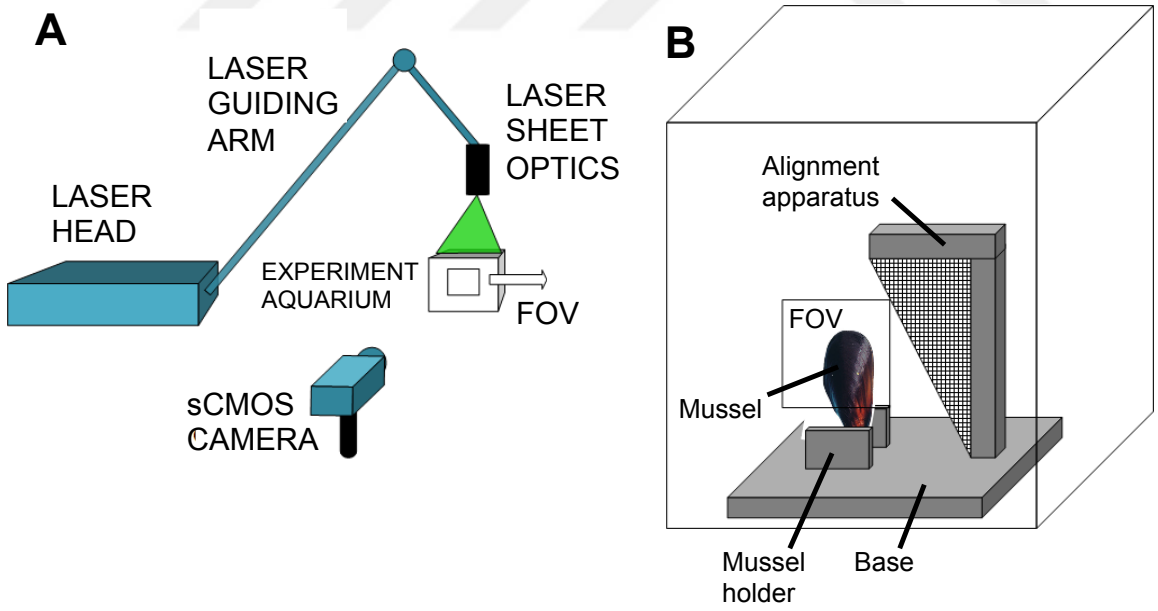

Figure 3.1. (A) Schematic of the particle image velocimetry setup to study isolated mussel flow structures. Main components of the experimental setup include a shuttered CW laser, articulated sheet optics arm, and an sCMOS camera operating at 25 fps in double frame mode. (B) Close-up of the experimental flow chamber and its custom made calibration/alignment apparatus oriented along the sagittal plane field of view (FOV).

3.2.2. PIV protocol and velocity vector field

The raw double-frame particle images were post-processed using Davis 8.2 (LaVision GmbH, Germany) to obtain the velocity profiles similar to our earlier work [63-65]. Five data sets were acquired for each mussel. Each raw data set includes at least 100 image pairs acquired continuously. 100 image pairs are found to be adequate for converged velocity values and also not too long to represent an instantaneous velocity value as a measurement time point. Thus, the presented exhalant jet velocity values in this manuscript are an average of 100 image pairs of corresponding time points of measurement. During the processing of velocity vectors, a mask was applied to segment the mussel cavity. A multi-pass algorithm with decreasing interrogation sizes from 96x96 to 48x48 pixels, both with 50% overlap, was employed. Smoothing and median filters were applied to avoid bad vectors.

3.2.3. Suction force calculation

Calculation of the pressure gradient provides an estimate of suction force generated by the mussel. Suction force can be calculated from the equation provided in our earlier work [65]. To explore the mussels' suction performance, experiments were conducted in the coronal plane. Suction experiments were performed for three mussels. Three data sets were obtained for each sample and data sets include 100 pairs of images. Time-averaged velocities were considered for pressure gradient calculations through the y-momentum equation [65]. The pressure gradient was calculated by assuming 2D flow in the downward suction direction between mussel shells that corresponds to the inside of the mussel in the coronal plane (see Fig. 3.3A). We employed spatial averaging of pressure gradients in the interspace to obtain smooth trends [65, 66].

3.2.4. Energy dissipation rate

The hydrodynamic dissipation rate was computed from the sagittal plane measurements using the

following formula:

$$E_{diss} = 2\nu\left(\left(\frac{\partial V_x}{\partial x}\right)^2 + \left(\frac{\partial V_y}{\partial y}\right)^2\right) + \nu\left(\left(\frac{\partial V_y}{\partial x} + \frac{\partial V_x}{\partial y}\right)^2\right) \quad \text{(E3.1)}$$

To estimate the dissipation rate in the sagittal plane, we used 2D spatial energy dissipation [67, 68].

3.3. Results

3.3.1. External flow structures

Mussels can simultaneously generate the exhalant jet and inhalant suction. The associated main flow structures are illustrated qualitatively in Fig. 3.2, based on our flow visualization experiments. Both the exhalant jet regime and inhalant flows are distinct for most flow states. The exhalant flow resembles a low Re number jet flow, which emerges as a single or double potential core region. Determination of an exact Re number is challenging due to the dynamic changes in the exhalant siphon effective orifice area, but are estimated to range between 50 and 500. Whereas for the inlet, a sink type inhalant flow is observed with lower Re numbers (Re < 90). Sink flow occurs along line absorbing fluid inwards and the inhalant siphon corresponds to the line where the fluid is absorbed. The radial flow area spanned by the exhalant siphon is significantly smaller than the inhalant siphon area, as also reported by Troost, Stamhuis [17], resulting in higher exhalant jet velocities.

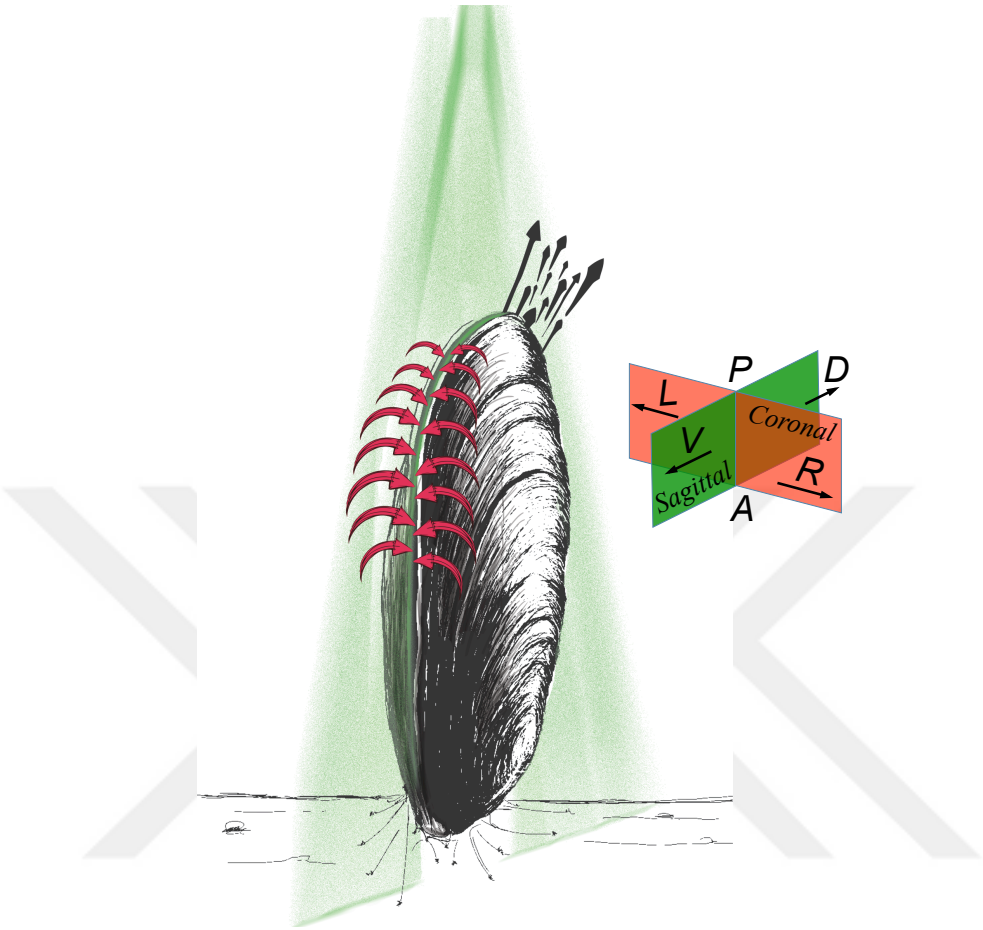

Figure 3.2. A cartoon representation of the main flow structures generated by *Mytilus Galloprovincialis* as observed during our experiments. Sink type inhalant flow is shown with red streamlines. Black arrows illustrate the exhalant jet flow. A laser sheet oriented along the sagittal plane is plotted in green. Body directions and anatomical planes where the measurements are performed are represented in the right side of the mussel. The Sagittal plane is represented with a green plane showing ventral (V) and dorsal (D) directions. The Coronal plane is represented with a red plane showing left (L) and right (R) directions. The posterior (P) and anterior (A) sides are also labeled. This plot is generated through qualitative dye-visualization experiments in addition to the PIV.

3.3.2. Inhalant Flow Field

The velocity field acquired in the coronal plane is presented in Fig. 3. Suction flow starts to accelerate proximal to the mantle curvature. While the exact acceleration region outside the mussel changes from subject-to-subject, primary acceleration is induced inside of the mussel, and the flow reaches a maximum velocity of 1.8 cm s^{-1} (Fig. 3.3).

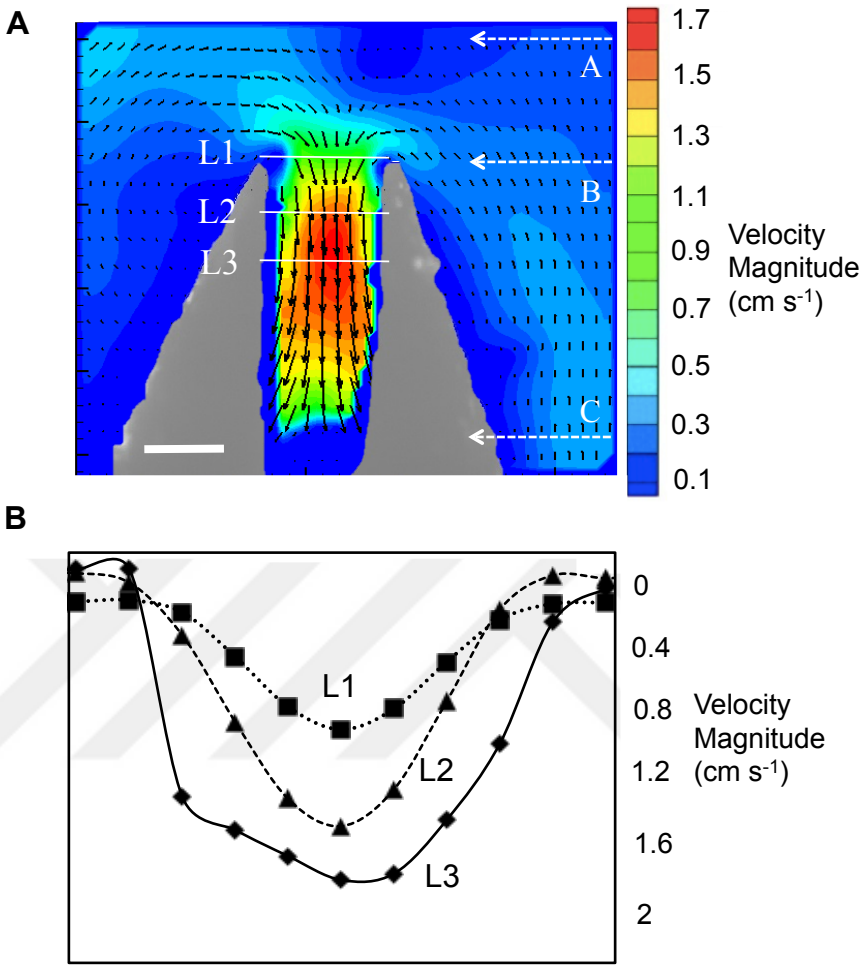

Figure 3.3. Vector field measurements at the coronal plane during suction feeding are presented**.** (A) PIV velocity field of mussel (volume of 34 cm^3) inhalant flow along the coronal plane. Dashed lines represented with A, B and C labels show the locations referred to in Figure 3. Scale bar is 0.5 cm. (B) Velocity profiles at L1 (squares with dotted line), L2 (triangles with dashed line) and L3 (diamonds) are plotted. Horizontal axis spans the entire length of lines L1, L2 and L3. Velocities sampled at L1, L2 and L3 correspond to the velocity magnitude of posterior-anterior velocity components. Corresponding lines; L1, L2 and L3 are shown in Fig. 3.3A.

Velocity profiles (magnitudes) that are acquired at 3 axial locations are plotted in Fig. 3.3B, illustrating the inflow velocity development. Velocity increases with decreasing distance to the mussel and reaches the global maximum inside the mussel. All velocity profiles are roughly parabolic, but the peak velocity increases close to the mantle core and reaches its maximum value of 1.8 cm s^{-1}. Nutrient water coming inside the mussel shell through suction feeding diffuses to

both the left and right sides of the mussel's interior. Fig. 3.4 displays the relationship between the velocity and pressure gradient at the centerline of the coronal plane. When velocity reaches its spatial maximum, the corresponding pressure gradient becomes zero inside the mussel mantle; in turn, the pressure gradient that corresponds to the suction force reaches its maximum at the entrance of the mussel cavity.

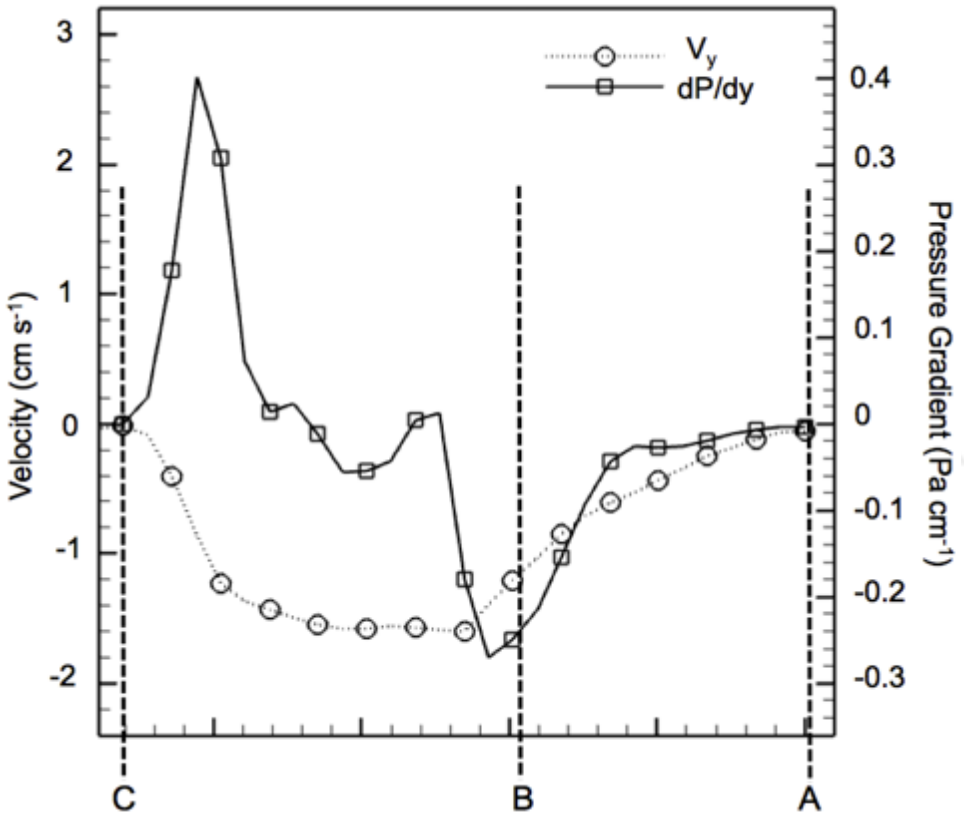

Figure 3.4. Average pressure gradient (dP/dy) and average inflow velocity distribution [69] is plotted along the inhalant suction streamline. y-direction corresponds to posterior-anterior direction. Horizontal axis is shown with A, B, and C letters. Locations of A, B and C are denoted in Fig. 3.3A. Location of B corresponds to the point where inhalant flow comes inside the mussel cavity.

3.3.3. Time-dependent exhalant jet flow regime

The exhalent flow occurred in non-periodic long-duration cycles. The peak velocities of the exhalant flow cycle are plotted in Fig. 3.5 for different mussel cavity sizes. Each point corresponds to the maximum exhalant jet velocity value averaged over 100 image pairs recorded during a period of relatively steady flow. We observe that exhalant jet flow peak velocity increases with

increasing volume ($R^2 = 0.46$). The highest recorded value of the peak exhalant velocity is 11.1 cm s^{-1}, corresponding to a mussel volume of 28 cm^3. The smallest value of peak exhalant velocity is 2.77 cm s^{-1} with a volume of 10 cm^3. As such, the samples are grouped in three based on their peak exhalant jet velocities (Table 3.1). These groups generate 4.78 cm s^{-1}, 6.83 cm s^{-1} and 9.52 cm s^{-1} average peak velocity with volume between 7-10 cm^3, 16-20 cm^3, and 27-34 cm^3, respectively.

Table 3.1. Three volume groups of mussels are studied through PIV. Number of mussels in each group, their average velocities and standard deviations are summarized for each size group.

Sample Number	Mantle volume range (cm^3)	Average peak exhalant flow velocity (cm s^{-1})	Standard deviation of peak exhalant flow velocity (cm s^{-1})
4	7-10	4.78	1.42
8	16-20	6.83	2.35
5	27-34	9.52	1.68

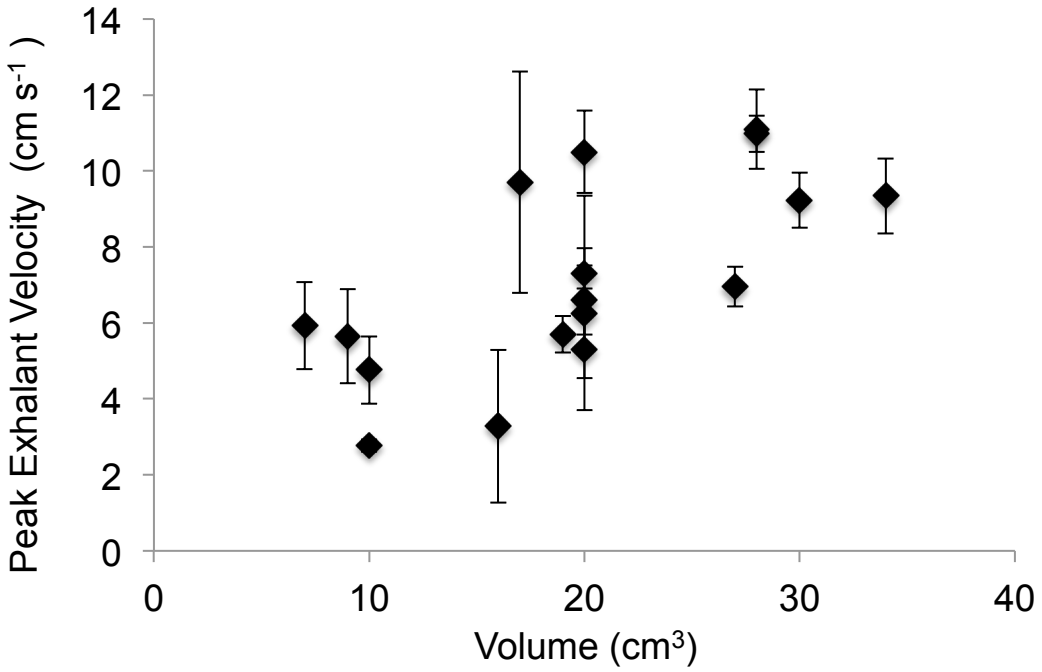

Figure 3.5. Peak exhalant velocities of *Mytilus Galloprovincialis* are plotted as a function of mantle cavity volume. A linear fit formula is obtained as y = 0.2244x + 2.7161 having an R^2 value of 0.46. Error bars indicate one standard deviation of peak exhalant velocities for each mussel during the time course of measurements (~4 seconds).

Fig. 3.6 presents the consecutively recorded instantaneous exhalant jet flow fields for a mussel having a volume of 28 cm^3. While a continuous stream of data is available, selected velocity fields are plotted to illustrate the observed exhalant jet flow structures. There was no periodicity in the flow patterns. The exhalant jet flow stream typically has a single core region during the initial phase of the exhalant flow cycle. The mussel converts the exhalant flow from a single core region of jet to a double core region, as can be observed from the instantaneous velocity fields of the last two time points (Fig. 3.6). 53% of the mussels generated double core jet regions for a finite duration during the velocimetry measurements. The separation of the jets randomly changes with the shape of the exhalant siphon, as is the case for the mussel depicted in Fig. 3.6 across all time points. The peak velocity of the exhalant flow is 6.21 cm s^{-1} at the initial measurement time point. Peak Velocity increases to 11.1 cm s^{-1}. After a 14 min time lapse, the peak velocity dramatically decreases to 4.5 cm s^{-1}. The largest decrease in peak velocity is observed at this time point because exhalant jet velocity is also decelerating at this instant. The mussel jet changes from the single-core to a double-core structure. Peak exhalant velocities at the time points shown in Fig. 6 are 6.21 cm s^{-1}, 11.1 cm s^{-1}, 9.95 cm s^{-1}, 4.5 cm s^{-1}, 8.6 cm s^{-1}, and 7.5 cm s^{-1}, respectively.

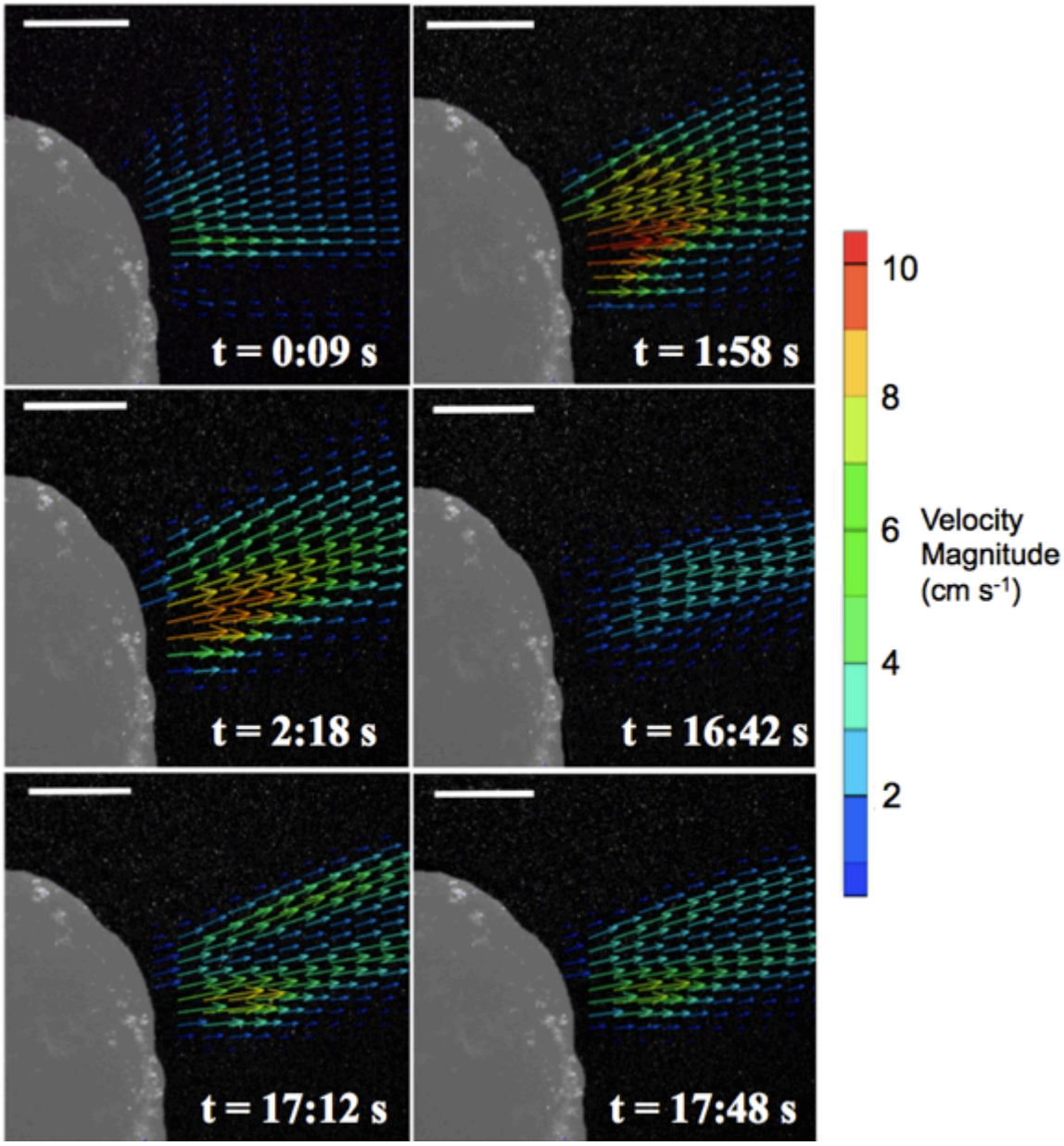

Figure 3.6. Jet flow types observed during a typical exhalant flow cycle of the mussel (volume of 28 cm^3). These exhalant jet flow configurations are observed at different time points. The mussel generates a single potential jet core region, typically during the start of the exhalant cycle between 9 s and 16 min. 42 s. Later, this jet is converted to a jet having a double potential core region, likely modulated through the flexible siphon apparatus at time point of 17 min. 12 s. Scale bars represent 1 cm.

Fig. 3.7 displays the peak velocity recordings for exhalant flow as a function of time for two different sized mussels with volumes of 7 and 10 cm^3 respectively. We obtained the peak velocity data at uniform time intervals. The peak exhalant flow velocity for the 7 cm^3 mussel was initially recorded as 3.1 cm s^{-1} and increased by a factor of 2, to 5.8 cm s^{-1}. The peak exhalant flow

velocity for the 10 cm^3 mussel was initially recorded as 2.77 cm s^{-1} and decreased to 1.7 cm s^{-1}. We did not find a periodic signal produced by the peak velocity of exhalant flow. Each mussel may demonstrate differences in the exhalant jet flow behavior and the peak velocity of exhalant flow.

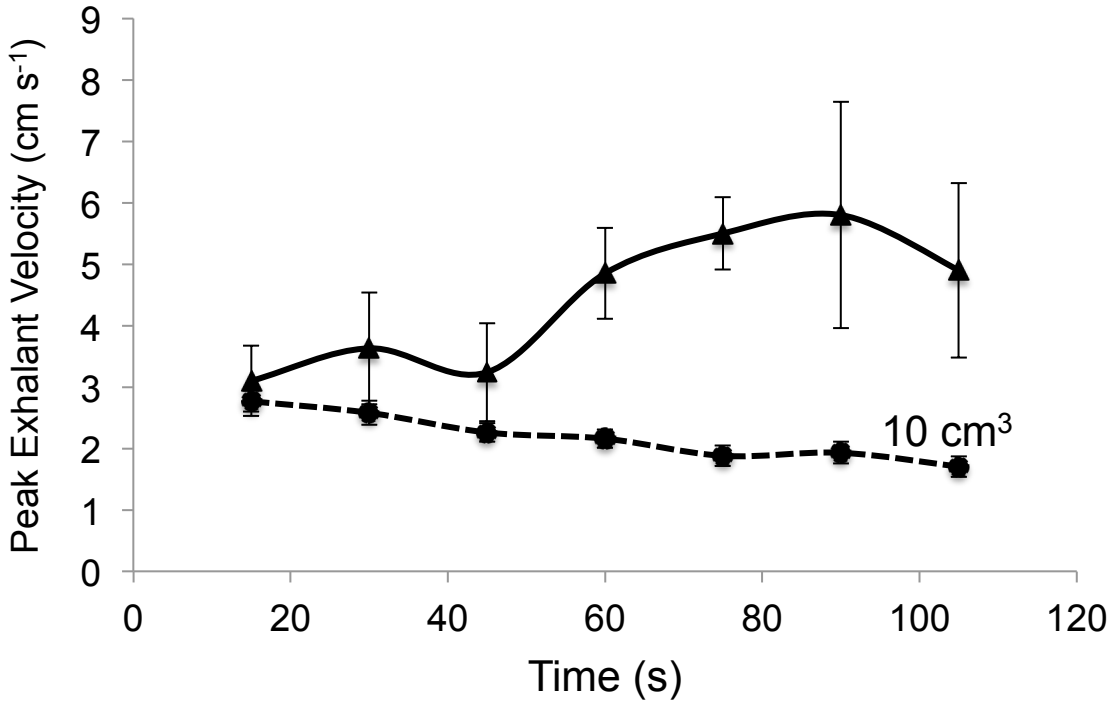

Figure 3.7. The time-resolved peak exhalant flow cycles and peak velocity magnitudes are compared for two mussel samples having different sizes (volumes of 10 and 7 cm^3). Peak exhalant flow velocities of two different mussels are tracked at the same time intervals. Error bars indicate one standard deviation of peak exhalant velocities for each mussel during the time course of measurements (~4 seconds).

3.3.4. Flow turning angle

We define the Flow Turning Angle (FTA) as the angle between the exhalant jet core direction and the inhalant maximum velocity vector. FTA is measured in the sagittal plane. For angle measurements, we selected the data set that has maximum peak velocity of exhalant jet flow for each mussel. Average FTA remains fairly constant at 90^o with a standard deviation of 12^o (Fig. 3.8).

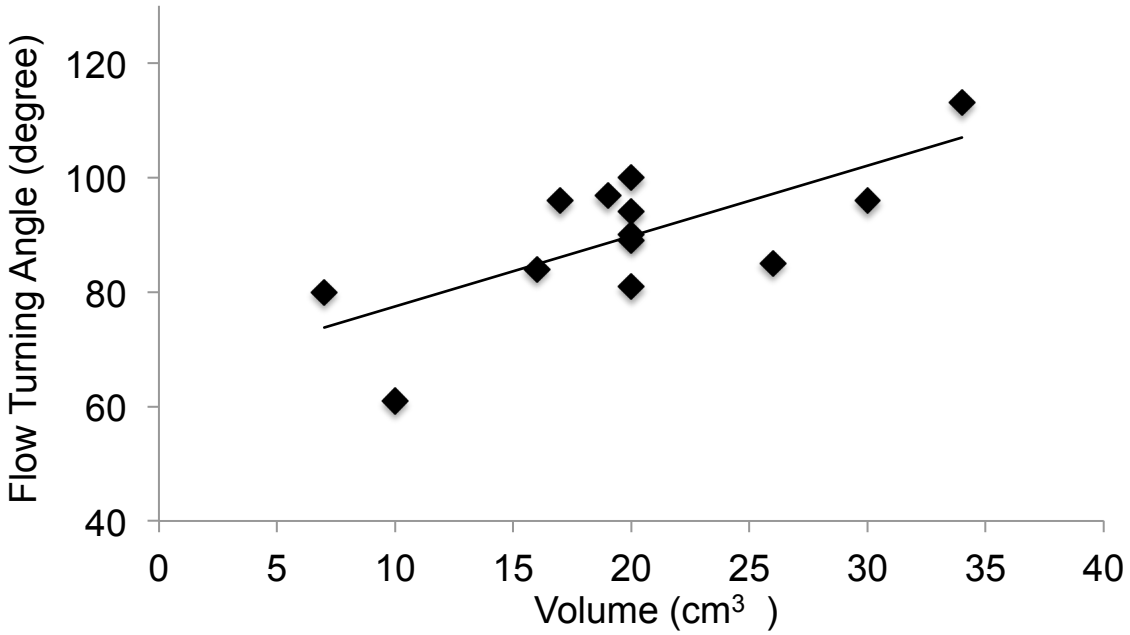

Figure 3.8. Flow-turning angle (FTA) vs. mussel volume is plotted. FTA is defined between the exhalant jet and the direction of peak inhalant flow. Least-squares linear fit formula of flow turning angle is y= 1.2296x+65.183 and R^2 value is 0.51.

3.3.5. Energy dissipation rate

We calculated the hydrodynamic dissipation to show that there is no interaction between the inhalant and exhalant jet flows for the measured FTA. The contour map of the time-averaged energy dissipation rate on the sagittal plane resembles a single core exhalant jet, as plotted in Fig. 3.9. The simultaneous inhalant flow region is also indicated with a yellow dashed line in Fig. 3.9, and is found to span a significantly larger flow area than the outflow.

In spite of its close proximity, the simultaneous inhalant flow did not interfere significantly with the outflow jet, while the peak dissipation close to the inhalant flow region is slightly lower than the undisturbed jet boundary layer (see Fig. 3.9). Lower inflow speed due to a larger flow area and the FTA result in an optimal energy dissipation field. It is also observed that the dissipation rate of the developed exhalant jet is lower and becomes unstable. We observe fluctuations in instantaneous energy dissipation rate values of the exhalant flow, particularly along the jet boundary layer. Hydrodynamic dissipation map presents energy efficient pumping even tough the

inhalant and exhalant jet flows are simultaneously generated and compete with each other.

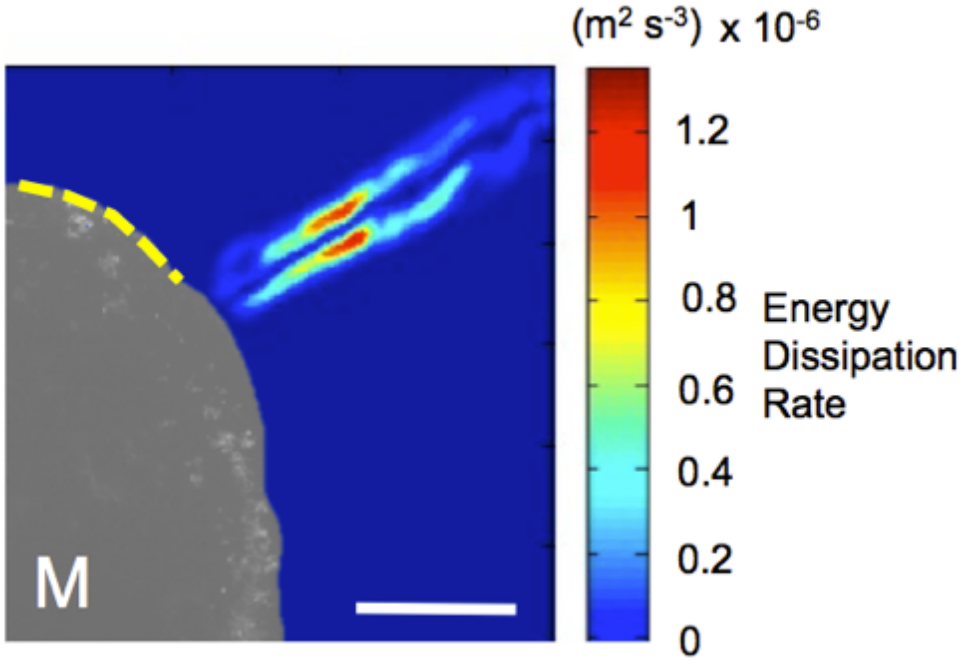

Figure 3.9. Distribution of the energy dissipation rate of exhalant jet and inhalant flows plotted on the sagittal plane external to the mussel (M). High dissipation rates are localized along the exhalant jet boundary layer. Yellow dashed line marks the region of inhalant suction flow, which is simultaneously generated with the exhalant jet. Scale bar is 1 cm. Mussel volume is 16 cm^3.

3.4. Discussion

3.4.1. Inhalant Suction Flow

Inhalant suction flow has a three-dimensional flow structure. In our experiments we minimized the out-of-plane flow velocity component (Dorsal-Ventral direction) by coinciding the coronal plane with the inhalant flow region, which is closest to the posterior-dorsal direction side of mussel. This is a typical approach to present complex 3D flow structures and sufficient to understand the present flow regime.

The inhalant flow regime determines the nutrient seed capture performance. Inhalant flow also sets the characteristic operating point for the internal pumping apparatus of the mussel. The suction apparatus operates intermittently and provides a bolus of seawater to mussel gills for particle retention. In a recent study the internal flow circulation of *Mytilus Galloprovincialis* [15]

was analyzed using phase-contrast magnetic resonance imaging (PC-MRI). PC-MRI sequences involve inherent averaging and could not capture the transient flow behavior as reported in the present study. As such, the detailed quantitative analysis of external flow structures provided in the present study supplemented the "internal" PC-MRI measurements of mussels. The exhalant jet and inhalant suction velocity values measured through PIV are of the same order as reported by the PC-MRI measurements [15], which is critical for the validation of both experimental approaches. Furthermore, investigation of the inhalant flow along both the coronal and sagittal planes is novel, and provided crucial insight on the nutrient capture biomechanics. Nutrient capture biomechanics reveals important properties of suction feeding that is characterized by the suction force which is estimated from the velocity field measurements and pressure gradient calculations. The coronal plane provided a window of opportunity, where the velocity field deep inside the mussel's suction apparatus is measured through a quantitative measurement technique for the first time in the literature.

Suction feeding flow dynamics have been studied extensively in active feeding of vertebrates [65]. The acceleration trend of the inhalant flow showed a similar behavior as the active suction feeding response of fish larvae operating at lower Re numbers [70]. Inhalant flow accelerates while approaching the mussel, but gains its highest velocity value inside the mussel. After reaching its highest velocities, water is distributed to both the right and left gills (Fig. 3.3A), towards the interflamentary cavities powered by lateral cilia [15]. Pressure gradient generated by the mussel determines the suction force acting on the food particles. The pressure gradient increases proximal and internal to the mussel mantle. Compared to the inefficient low Re number in larval fish feeding [70], the suction force in mussels influences a larger area proximal to the mussel mantle (Fig. 3.4) and is significantly more functional due to continuous circulation.

The coronal plane PIV experiments demonstrated novel flow regimes of inhalant flow in

Mytilus Galloprovincialis that have not been previously reported (Fig. 3.3A). These flow regimes reveal an important concept of non-interacting inhalant and exhalant jet flow behavior. The inhalant flow resembles a low velocity sink type 3D flow field that is highly curved at the mussel mantle, while the exhalant flow is more concentrated as a higher velocity jet (Fig. 3.6). Lower values of energy dissipation are observed at the interface where exhalant and inhalant flows would otherwise interact and result in energy loss hot spots. As such, the highest dissipation rates are localized only at the borders of the exhalant jet core boundary layer. This configuration is beneficial to maintain efficient simultaneous exhalant jet and inhalant flows, reducing high-dissipative interference between these two flow streams. Flow Turning Angle (Fig. 3.8) is also important for efficient simultaneous exhalant jet and inhalant flow, and is found to be relatively constant for the sizes studied. We hypothesize that the flow turning angle between inhalant and exhalant flow is critical for energy efficient filtration. Our study suggests that there is a unique angle between exhalant jet and inhalant flow streams, which maintains kinematic similarity.

3.4.2. Flow control components of mussels

There are numerous functional components in the mussel that are used for inhalant and exhalent flow control. The bulk flow rate, i.e. large amount of water moved by the inhalant and exhalant flows, is modulated through the gape that is adjusted by the shell movement. This can increase and decrease the flow rates of both the exhalant jet and the inhalant flow simultaneously. Inside the shell, we observed that mussels can change the characteristic of exhalant flow from a single core jet to a double core, possibly through conformational changes of the internal exhalant siphon. However, our experimental set-up did not allow us to record the siphon configuration simultaneously with the velocity field, as the siphon is located inside the mussel shells and cannot be seen in the sagittal laser plane (velocity field). However we have observed the dynamic configuration of the exhalant siphon and illustrated it in a sample movie. The third control element

is achieved through the zippering property of the inlet duct of gills that specifically modulates the inhalant flow rate. We observed the coaptation of left and right dorsal edges of mussel gills resembling a fine zipper for suction control. A substantial portion of the flow area can be reduced through this dynamic coaptation region, while the inhalant velocity decreases as 0.8 cm s^{-1}, which is related to filtration rate. Another control element is the edge of the mantle, which has plus shaped fringes. They are inside the left and right shells of the mussel as exhalant and inhalant siphons, but there are no fringes at the exhalant siphon. Ciliary structures are also important components of control for exhalant jet flow. The quantity of generated flow can be changed by activation and deactivation of different lateral cilia regions [15].

3.4.3. Exhalant jet flow

While it is observed that the particles larger than 2 μm are retained by the gill filament network of certain mussel species [71], in our experiments the exhalant jet is fully-seeded with the tracer particles. For accurate PIV analyses, the number of particles as low as 10-15 is found to be sufficient for each interrogation window of size, 48x48 pixels. During our experiments only a few of the samples pump partially "empty" water devoid of particles, but these are not included in our manuscript. Further to guarantee reliable PIV analyses for low particle density exhalant jets, we reduced the size of the PIV interrogation window, 96x96 pixels to 48x48 pixels, and demonstrated identical velocity fields.

Peak exhalant flow measurements recorded in the present study for isolated mussels (Fig. 3.5) are similar to the earlier values presented in the literature: See Frank, Ward [16] and Riisgård, Jørgensen [18], even though mussel species are different. A linear correlation with a low R^2 value is observed between the peak exhalant velocity and mantle volume; therefore, we organized the mussels in our experiments into three groups based on their volumes. Table 3.1 shows these three size groups, their corresponding average velocities, and standard deviation values. Mussels with

bigger volumes are capable of producing higher exhalant flow velocities (Table 3.1). In addition, the standard deviation of peak exhalant velocities increases with increasing volume.

Water quality and presence of algal cells may strongly influence the opening degree, and too many cells may cause overloading and result in coughing, production of pseudofaeces, reduction of shell opening and cessation of filtration rate, resulting in wide variation in clearance rate. To prevent measuring non-optimal pumping performance of mussels, we performed auxiliary filtration tests before each experiment for confirmation of the normal steady filtration rate. Long-term monitoring of the peak exhalant jet velocity indicated no periodicity in either the exhalant or inhalant flow, as previously reported [15]. Time resolved peak exhalant jet velocity also does not show any specific pattern (Fig. 3.7). Two mussels present different peak exhalant jet behavior. Beyond the periodicity, mussels can change the jet profile from a single core jet to a double core, or visa versa. Changing jet profile was observed in half of the mussels used in these experiments. Jet profile changes should be studied in detail to investigate the exact reason for this phenomenon. While transitionary flow structures are fully captured through the present 2D PIV methodology, a 3D tomographic set-up would elucidate the three dimensional effects. Likewise, the exhalant flow direction is regulated frequently through the exhalant siphon apparatus.

In conclusion, time-lapsed PIV measurements allowed us to understand and quantify the fluid dynamics of exhalant and inhalant flow in *Mytilus Galloprovincialis*. Major biological components associated with flow control function were also identified. PIV was applied in two different planes. Coronal plane velocity measurements illustrated that mussels create sink type inhalant flow, which allowed us to estimate the suction feeding performance of mussels. Pressure gradient is calculated from the measured vector field on the coronal plane, which is used to estimate the suction force. Suction force quantifies the biomechanical characteristic of suction feeding. The velocity field along the sagittal plane was measured to simultaneously investigate the

dynamics of exhalant jet and inhalant flow. This measurement plane also allowed us to measure the angle between the exhalant jet and the inhalant flow. FTA is important for optimum pumping as it prevents interaction of inhalant and exhalant flows and found to be independent of mantle size. Simultaneous energy efficient pumping is demonstrated through the hydrodynamic dissipation map computed from the PIV vector field in the sagittal plane (Fig. 3.9). The peak velocities and dynamics are reported for both flow regimes as a function of size, which provide pumping performance. Mussels should be considered as smart micro-pumps because they can pump their inhalant and exhalant jet flows without any major energy dissipation. Moreover, mussels can change both the velocity and type of exhalant jet, and velocity of inhalant flow using their multiple flow control elements.

Chapter 4. Characterization of zebrafish larvae suction feeding flow using μPIV and optical coherence tomography

4.1. Introduction

Larval fish experience extreme mortality rates during the first days of their lives. In the wild, over 90% of a typical brood can perish during this "critical period". Somewhat surprisingly, larval mortality is also extremely high in mariculture facilities, where food is abundant and conditions are stable. It has recently been suggested that this mortality could be attributed to the hydrodynamic regime in which larvae dwell [19-21]. Like most aquatic vertebrates, larval fish exploit a physical reality by suction feeding to exert a hydrodynamic force on their prey. This is done by rapid expansion of the buccal cavity, which results in decreasing intra-oral pressure, thereby creating a flow of water external to the mouth. The spatio-temporal properties of the fluid flow generated due to this buccal expansion determine the efficiency of food intake [20, 21], and that efficiency detrimental for the survival of fish larvae [72]. While much is known about these patterns in juvenile and adult fishes, no direct measurements are yet available for fish larvae (reviewed in [20, 22])

Flow visualization experiments with adults from several species reveal stereotypical spatial and temporal patterns of the suction flows [22]. Suction flows are characteristically unsteady, attaining fast flows (> 3 m/s) within very short time frames (>20 ms) [23, 24, 73, 74]. Steep pressure and velocity gradients are also characteristic, with flows decaying to <1% of their speed within a distance of one mouth (orifice) diameter [23, 24, 73-75]. Flows typically start at the onset of mouth opening, and inwards flow occurs consistently until the mouth closes. Peak flow speed is usually attained when the mouth is fully open, usually very close to the time of maximum gape

[23, 24, 73, 74]. However, CFD modeling and tracking of food particles suggests that some of these patterns may change in larval fish due to the dominance of viscous forces in low Reynolds (Re<100) conditions. Therefore, the present research paper experimentally investigates the low *Re* number pulsatile creeping flow performance for the larval stages of zebrafish. The development of established animal models with complete genomes, such as the zebrafish, can facilitate interdisciplinary investigations of coupled neurobiology and fluid dynamics relating to taste and smell through the use of transgenic function-controlled larvae and can help improve our understanding of the suction feeding process.

A high-speed microscopic flow visualization system equipped with time-resolved optical dissection imaging capability during the suction feeding period is necessary to elucidate the coupling effect between the rapid cranial movements and spatial synchronously induced flow fields. In this study, a new hydrodynamic approach is introduced to better address this hallmark behavior of teleost fishes.

4.2. Methodology

Nine individual zebra fish larvae (*Danio rerio*), belonging to 3 developmental groups, were used in the experiments. These subjects span early-development larvae with a total length less than 5 mm (Group 1), medium size with a total length between 5 and 10 mm (Group 2), and mature subjects with total length up to 2 cm (Group 3). A biocompatible flow tracer of mashed raw egg yolk was prepared with distilled water to reach a solution concentration of 1%. The feeding cycle was identified by tracking the tip of the lower jaw and gill flap movements. Fish larvae were placed in a petri dish and subsequent imaging was performed dorsally, using a Leica MZ 16 FA stereomicroscope (10× magnification) with a 2×objective and a high-speed CMOS camera (Photron SA4, Photron Limited, Japan) at 1024 ×1024 image resolution for data acquisition. Image series during spontaneous feedings were typically acquired at 500 Hz, as described in an earlier

publication [76]. Post-processing employed 32×32-pixel interrogation windows for the first pass and 16×16 for the second pass.

Optical coherence tomography (OCT) imaging was performed in a temperature and humidity controlled chamber using an interferometric technique [77]. Acquisition was performed at 67 Hz using a spectral domain system with a 4.3 μm resolution (Ganymede, Thorlabs, Germany). The light source consisted of a super luminescent diode with a center wavelength of 930 nm. The interferogram was detected using a linear CCD array-based spectrometer. For further details of our in-house OCT system, please refer to References [77, 78].

4.3. Results and Discussion

4.3.1. Buccal Cavity Kinematics

The Buccal volume was imaged through time-resolved OCT to provide anatomical evidence on how buccal expansion regulates suction flows. OCT allowed us to identify the active regions of the buccal volume and to distinguish between the disparate feeding and respiration cycles. Representative three-dimensional gross dimensions of the mouth cavity were measured for the zebrafish in Group 2 (see Figure 4.1). We observed rapid mouth opening and closing movements associated with the feeding cycle. These movements occurred proximal to the mouth cavity, reaching a maximum 162% increase in projected area locally, at cross-sections similar to those shown in Figure 4.1A. The jaw opening cycle was also verified based on the lateral movies recorded separately (see Figure 4.1B). Along the mouth towards the tail, the wall motion during the feeding cycle reduced significantly, resulting in a 22% increase in the total projected cavity area. During the suction feeding cycle, a short section of the buccal cavity, located proximal to the mouth, is observed to move significantly more than the other internal mouth regions. This short active mouth cavity region could be associated with the reduced low Reynolds number suction

performance.

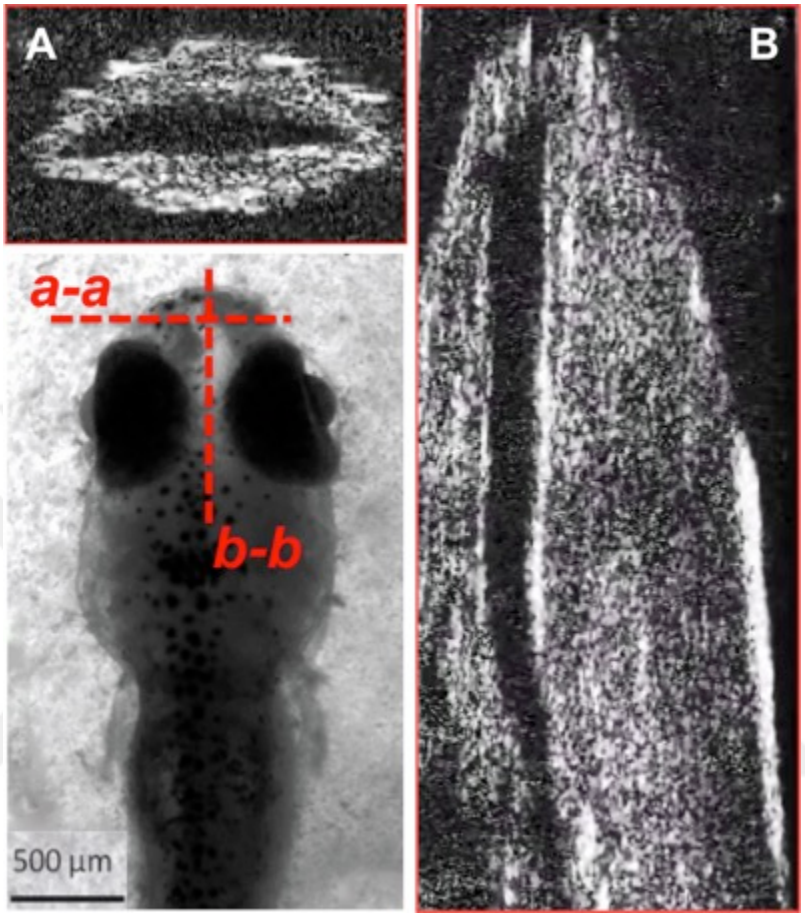

Figure 4.1. Optical coherence tomography images of zebra fish larvae mouth cavity at maximum opening (see Supplementary Movie 2: OCT Transverse Plane and Supplementary Movie 3: OCT Mid-Sagittal Plane). (A) Section a-a, axial slice of mouth cavity (B) Section b-b, anterior/posterior view of mouth cavity.

One of the unresolved questions in fish suction feeding is the shape and dynamics of the buccal (mouth) cavity during suction feeding, though OCT imaging has proven useful to reconstruct the 3D mouth kinematics. To our knowledge, this information has not been available in the literature for both the adult and the larval stages. Thus, the present quantitative three-dimensional imaging approach will expand upon the earlier descriptive studies of jaw kinematics, which focus entirely on the external anatomical elements using high-speed cameras [21, 79].

4.3.2. Flow Structures

Peak inflow velocity vector fields for three representative zebrafish larvae sizes are plotted in Figure 4.2. Data was recorded by viewing the top of the fish with a clear particle flow showing particles flowing both in and out of the fish. The velocity field during a typical burst event was also acquired as shown in Figure 4.3, and occurred at a slightly different PIV plane than the suction. Topology of the body geometry around the mouth, in particular its symmetry or lack thereof, contributes to the three-dimensional external flow structures. This particle flow had several interesting characteristics including its symmetry and consistency, indicating that it was not necessarily flowing through the mouth. For example, we observed two symmetric recirculation zones located symmetrically proximal to the mouth, whose strength diminished as the fish grew (see Figure 4.4 for the close-up view). These external vortical structures are reported for the first-time in the literature, and will influence feeding performance significantly. As a result, analogous external recirculation zones can be employed in pulsatile inflow biomedical devices to augment low Re internal flow; this should also prompt future studies. As the fish grew older, the inlet suction sometimes occurred through two distinct flow pathways, as shown in Figure 4.2. For larger fish, higher peak velocities and longer feeding cycle periods are recorded and summarized in Figure 4.5. A fully developed zebrafish larvae can extend its jaw to increase induced flow velocity to a maximum of 8 mm/s when prey is within its proximity. These measurements are in agreement with a recent tomographic PIV study of *adult* zebrafish during strike feeding, where velocity magnitudes of 45-60 mm/s are reported [80].

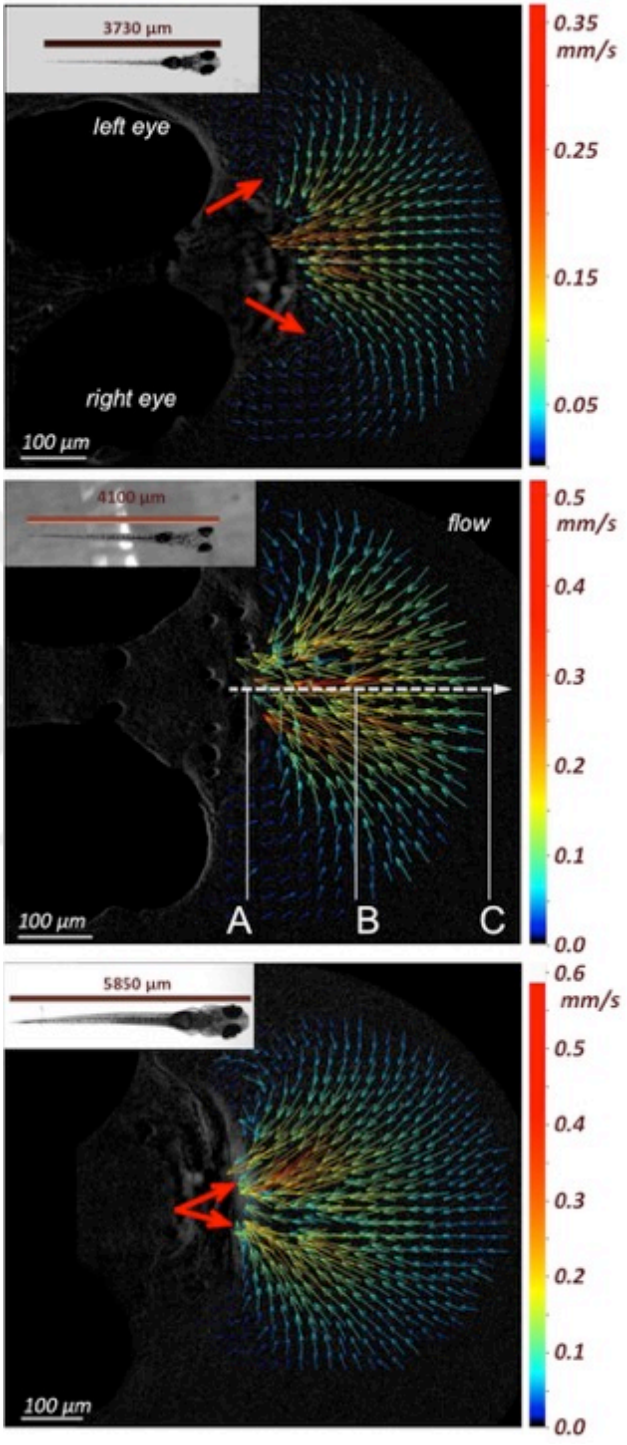

Figure 4.2. Processed µPIV results showing the induced flow field by suction feeding movement of a zebrafish larva. Sample inflow velocity vector fields close to the mouth for increasing body sizes (top to bottom). µPIV measurements correspond to the frontal plane that is aligned with the mouth opening. Inserts show the corresponding full length of the zebrafish samples. Arrows refer to major flow patterns discussed in the text. The dashed line corresponds to the central streamline through A, B, and C with increasing *x*-coordinate. Pressure gradient is computed at seven lines, where the central streamline is in the middle (please see Figure 4.5).

4.3.3. Suction Force on Prey

The momentum equation along the central inflow streamline of the mouth aperture provides an estimate of the suction force during feeding, as shown in Figure 4.2.

$$F_{pg} = -\frac{dp}{dx} L_x A_f \qquad \text{(E4.1)}$$

L_x and A_f denote the effective length and frontal area of the prey (seeding particles), respectively. The pressure gradient can be computed from the velocity field, including two-dimensional effects [81];

$$\frac{dp}{dx} = -\rho \left(V_x \frac{\partial V_x}{\partial x} + V_y \frac{\partial V_x}{\partial y} \right) + \mu \left(\frac{\partial^2 V_x}{\partial x^2} + \frac{\partial^2 V_x}{\partial y^2} \right) \qquad \text{(E4.2)}$$

For a better estimation of the suction force, the pressure gradient is averaged along the control volumes, which include the central inflow centerline represented in Figure 4.2. In Figure 4.6, a typical relationship between the pressure gradient and the induced flow field are plotted; two distinct suction flow trends are observed. At the far field of the mouth aperture, the pressure gradient and the spatial velocity are correlated, indicating a substantial suction force for prey recruitment (Point C to B). The maximum streamwise velocity is reached at point B, which almost coincides with a local peak of the pressure gradient. Proximal to the mouth aperture and through the deceleration region (Point B to A), the pressure gradient drops rapidly, following an oscillatory trend, which could potentially enable prey engulfment.

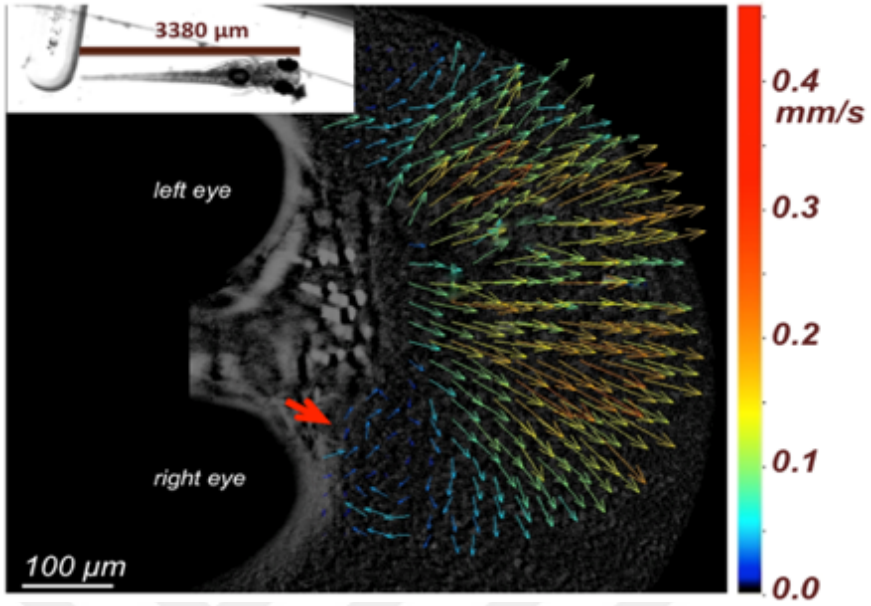

Figure 4.3. The peak velocity field captured during a typical burst event for a zebra fish larva from the small size group. This outflow phenomenon occurs occasionally during feeding. Arrow indicates the recirculation zones generated.

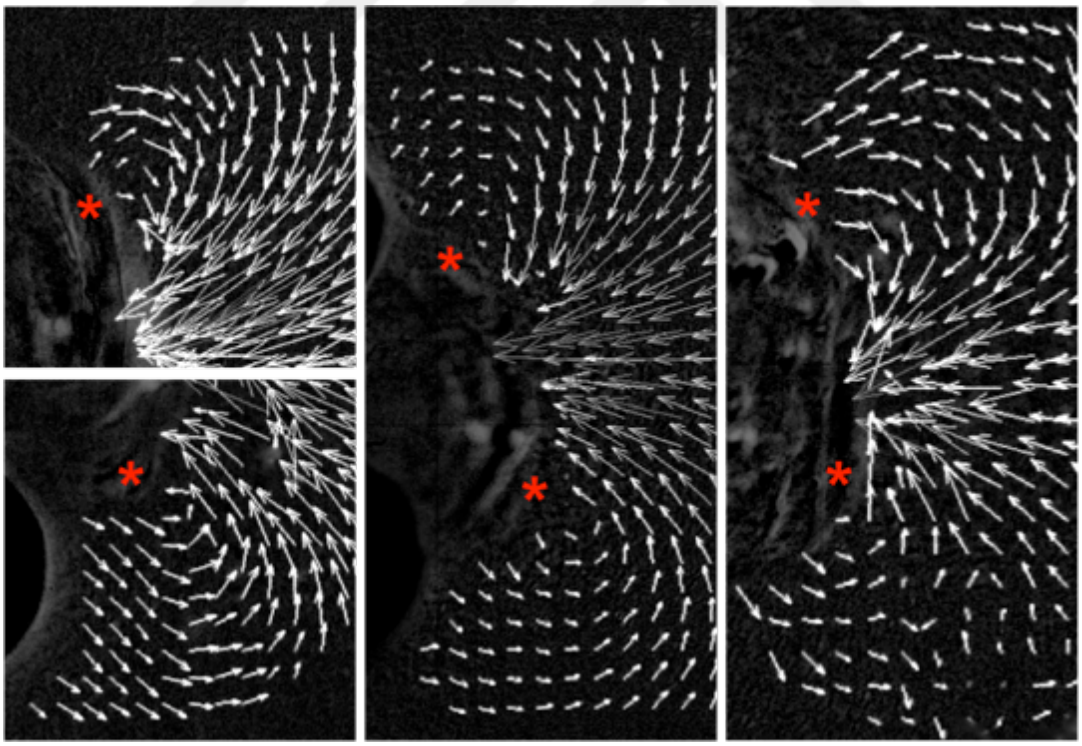

Figure 4.4. Close-up views of the recirculating velocity vectors recorded from 4 different samples during the suction feeding cycle (marked with asterix). Both symmetric as well as asymmetric recirculation zones are observed.

Computational fluid dynamics simulations of adult fish regimes show that the peak flow is located very close to the mouth while our measurements indicate that this is not necessarily true for larval

fish.

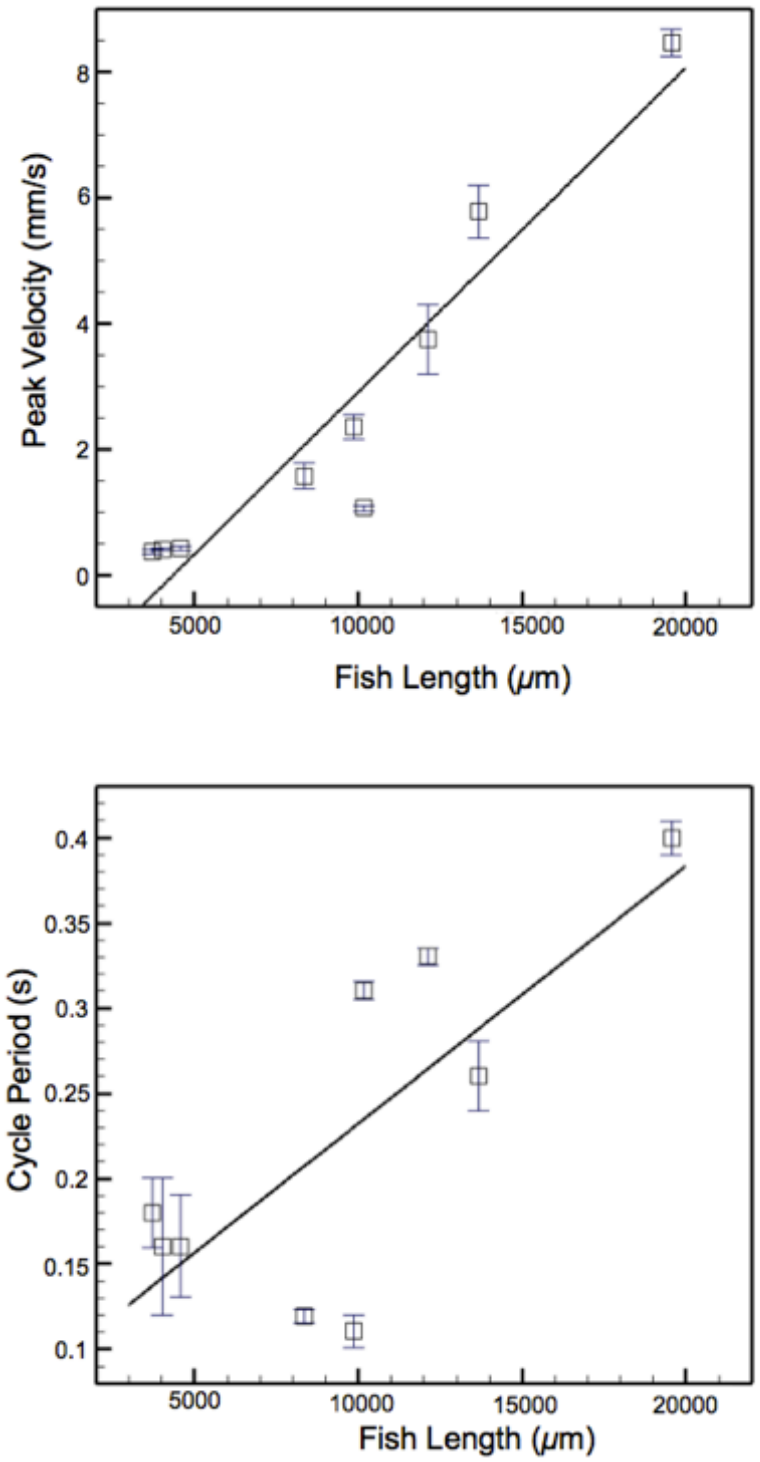

Figure 4.5. Peak inflow suction velocity (V_{peak} = -2.249 + 0.0005158L, R^2=0.90) and feeding cycle period ($T_{feeding}$ = 0.08085 + 1.514e-05*L, R^2=0.60) for increasing zebra fish larval size and development age. The linear regression fit for each parameter is plotted.

Further experiments are needed to show whether the low-pressure gradient between points B-C is due to some hydrodynamic phenomena specific to larval stages (e.g. the mouth vortex in Figure 4.2 and 4.4, or the low larval tissue compliance of the zebrafish introducing time-delays in the inflow bolus), or whether it is due to the near-wall limitation of our μPIV measurements, which were made closer to the mouth. The near-wall limitation is due to the use of discretized/partial PIV interrogation windows situated closer to the wall region and is further challenged by the 3D flows that follow the body contour in our application.

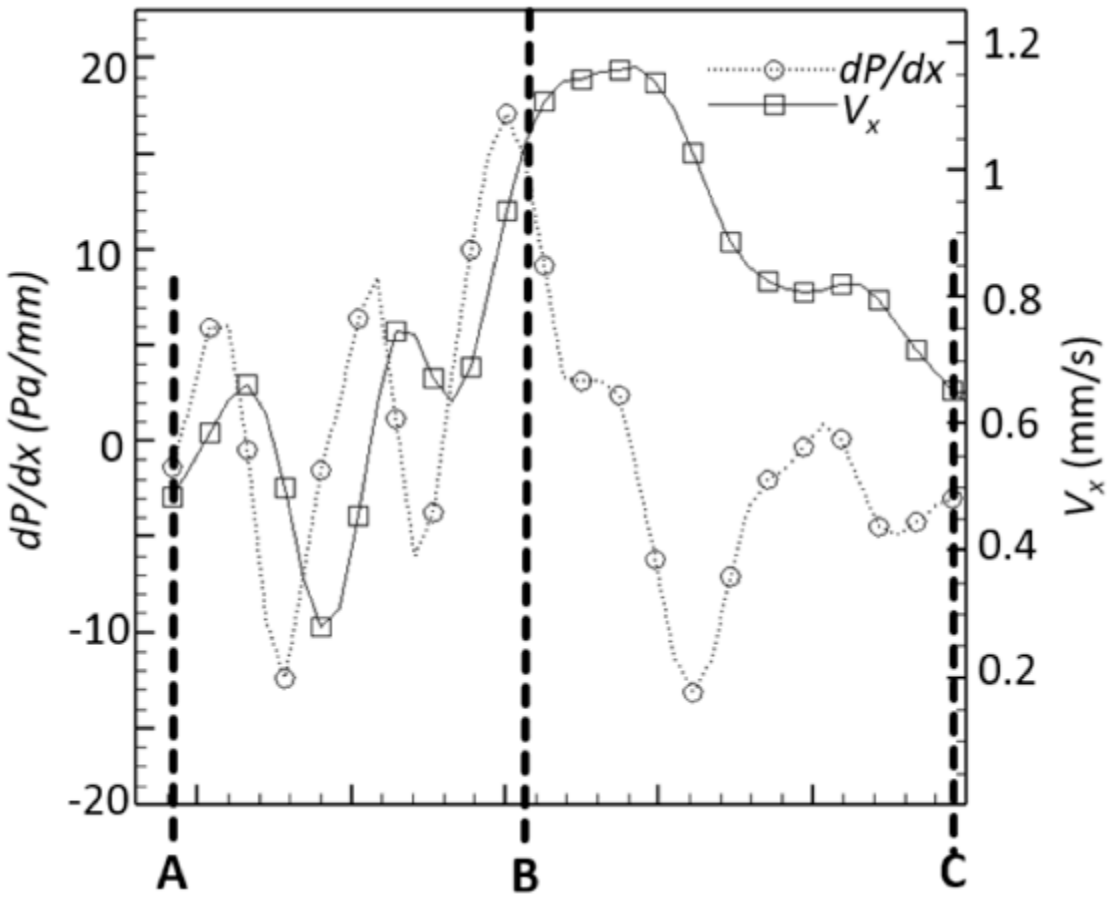

Figure 4.6. Axial velocity V_x and pressure gradient *dP/dx* along the central inflow streamline of the zebrafish oral aperture due to induced flow field during the suction feeding. Axial velocity and pressure gradient are area averaged around the central inflow centerline (shown with dashed line in Figure 4.2). Locations of points A, B, and C are labeled in Figure 4.2.

4.4. Limitations

In addition to fluid dynamics, the performance of larval fish feeding depends on physiological factors that change constantly as the fish grows, such as optimal ingestion, digestion, and absorption [82]. The present study focused exclusively on mechanical factors. Furthermore, as this study employed a stationary animal/prey model, which is typical for earlier larval stages, it also ignored the effect of external flow caused by body strike movement [83]. We captured the feeding cycle in our experiments, but other modes of operation and anatomy may play a role in the resulting flow fields [84]. In particular, differentiating the steady-stage respiration and feeding cycles was challenging when investigating younger fish. For the larger larvae group (Group 3), it was observed that in addition to normal jaw opening, the respiratory cycle caused ~1 mm/s of peak induced flow velocity. Respiration induced flow fields require more detailed studies in the future, though it seems clear that they create significantly lower velocities than those produced during the feeding cycle. In order to compare our results with those from earlier experiments we tried to capture velocity fields from the side; however, this also proved challenging, since the fish naturally lies on its belly and will often reorient itself. While we obtained good side view vector fields and verified flow both into and out of the fish, these results are not included in this research paper, as they required the use of tricaine (an anesthesia) to capture flat fish orientation under our microscope set-up. Finally, our group has recently developed a “true” OCT-PIV technique, which can track the intensities of the particles from the OCT data [77, 78]. However, the data acquisition rate of this technique only barely satisfies the imaging requirements for capturing the rapid feeding cycles encountered in the present larval stages. Thus, the present study was conducted using the traditional high-speed CMOS cameras.

4.5. Conclusion

In this study, the induced flow fields present during the suction feeding motions of zebrafish larvae together with the associated jaw movements are analyzed using high-speed μPIV and OCT, respectively. The quantitative results obtained can impact biological studies that focus on inactive predatory-prey interactions as well as on the evolution of the complex jaw protrusion mechanisms of bony fishes. The peak velocity of induced flows can soar to 8 mm/s for rapid capture when prey is nearby during a predatory strike from late-stage zebra fish larvae (L = 20 mm). Our results enhance the understanding of suction performance from kinematic and morphological perspectives. For the first time in the literature, the present experiments provide the baseline flow regime and the complete external flow fields of a common transgenic animal model at the creeping flow regime.

Chapter 5. Fluid Mechanics in the olfactory system of zebrafish embryo

5.1. Introduction

Cilia are microscopic hair like structure extending from the surface of almost all cells of the vertebrate body [25]. Motile cilia actively move and drive directional flow patterns across tissues, whereas primary cilia are enriched in receptors and play crucial sensory roles [26]. It is therefore not surprising that mutations affecting the structure, function or presence of cilia result in multiple human pathologies, collectively known as ciliopathies [85]. Throughout vertebrate evolution, the directional flow generated by the beating of motile cilia was utilized for diverse set of functions [86]. For example, in brain ventricles, cilia-mediated flow allows the delivery of nutrients and signaling molecules as well as the clearance of waste products, such as neurotoxins and molecular aggregates [27, 87]. Whereas in the respiratory tract motile cilia control the thickness of the protective mucus and clearance of toxic substances [28, 88, 89]. Despite the clear role of cilia mediated flow in all these vital processes, we still know very little about how coordinated ciliary beating generate complex hydrodynamic flow fields and what other important functions are mediated by this flow [86].

One of the main obstacles hampering the studies of motile cilia function is the difficulty of monitoring ciliary beating patterns and flow fields simultaneously, in living organisms. Here we introduce a new model for ciliary beating, the motile cilia of the nose, which can overcome the limitations of accessibility and facilitate in depth studies of motile ciliary function in vertebrates. The nasal epithelium is one of the most accessible tissue decorated with motile cilia, where they move liquid or mucus in the nasal cavity [90, 91]. While the presence of mucus is important for dissolving odors and shuttling them to olfactory receptor neurons (ORNs) [41], it is unclear

whether the motile cilia of the nose have a more direct sensory function and can facilitate the detection of odors or modulate olfactory computations by generating flow fields. In this study, by taking advantage of the accessible olfactory epithelium of zebrafish larvae, we characterized how ciliary beating generates robust stereotypical flow, regulates odor sampling and improves temporal resolution of olfactory computations in the brain.

5.2. Materials and Methods

Paralyzed larvae were embedded in agarose in a Fluorodish. Agarose was removed around the head to avoid any disturbance of the flow. 0.16um fluorescent particles (Spherotech, 1:200 dilution) were added to the AFW. Recordings of flow fields from salmon were done on decapitated fish heads, positioned on a Fluorodish (World Precision Instruments) coated with sylgard and fixed by an insect pin.

Time lapse images were acquired on a confocal microscopy (20x water immersion, NA 1) at either 512x512 pixel with 465ms/frame (big field of view) or 128x128 pixel, 3x zoom with 51.2ms/frame (small field of view). Particle images were processed in DaVis 8.2 (LaVision GmbH, Gottingen, Germany). All recordings included 1200 image frames, which was determined by perfectly converging running average. Multiple interrogation windows with decreasing size were used for vector calculations. Interrogation size from 128x128 to 48x48 pixels with 50% and 2 passes were used for flow recordings with 512x512 pixels resolution. Interrogation size from 64x64 to 12x12 pixels with 50% and 2 passes were used for flow recordings with 128x128 pixels resolution. During processing, masking was applied to fish body. Smoothing and median filter were used to smooth vectors and eliminate the neighboring bad vectors, respectively.

Residence time was obtained by the following equation: (length of particle path)/ average velocity. Average velocity is average of maximum velocities of inflow and outflow. Length of

particle path (38.48um) was determined upon fitting a curve (20 um above the surface of pit due to cilia) as path of flow particle in the pit by using the dimensions of pit.

5.3. Results

5.3.1. Multiciliated cells and beating cilia on the olfactory organ of zebrafish embryo

In 4 days old zebrafish larvae, the nose pits are hollow cup-like structures located in the snout (Fig 5.1A,A'). Multiple cell types constitute the olfactory epithelium (Fig 5.1A'') and can be differentiated according to their morphology[92]. Multiciliated cells (MCCs) are cuboidal cells, which harbor large bundles of acetyl tubulin positive motile cilia. They are arranged in a single layer surrounding the rim of the nose pit. In contrast, the ciliated ORNs have primary cilia with sensory function and are characterized by a pear shaped body [93]. ORNs are located below the MCCs at the bottom of the pit and exhibit dendritic knobs bearing fewer non-motile cilia decorated with the olfactory receptors (Fig 5.1A'', A'''). We observed that the ciliary beating of MCCs interferes with the transmission of light and can readily be measured as periodic oscillations of pixel intensity by using a simple microscope at relatively high spatial and temporal (>100Hz) resolution. In order to quantify the ciliary beating frequency (CBF) we performed Fourier transformation in every image pixel across 10 seconds and visualized the peak frequency as a heat map (Fig 5.1B, C). Regions with robust CBF overlap with the area where motile cilia extend into the cavity of the nose pit. No CBF was detected in the middle or outside the pit (Fig 5.1B). The average CBFs of a total of 130 larvae show a normal distribution ranging from 18.9 to 29.5 Hz with a mean value of 24.4 +/- 2.35 Hz (Fig 5.1C-D). Interestingly distinct patches with robust local peak beating frequencies can be distinguished and remain stable over time (Fig 5.1B,E).

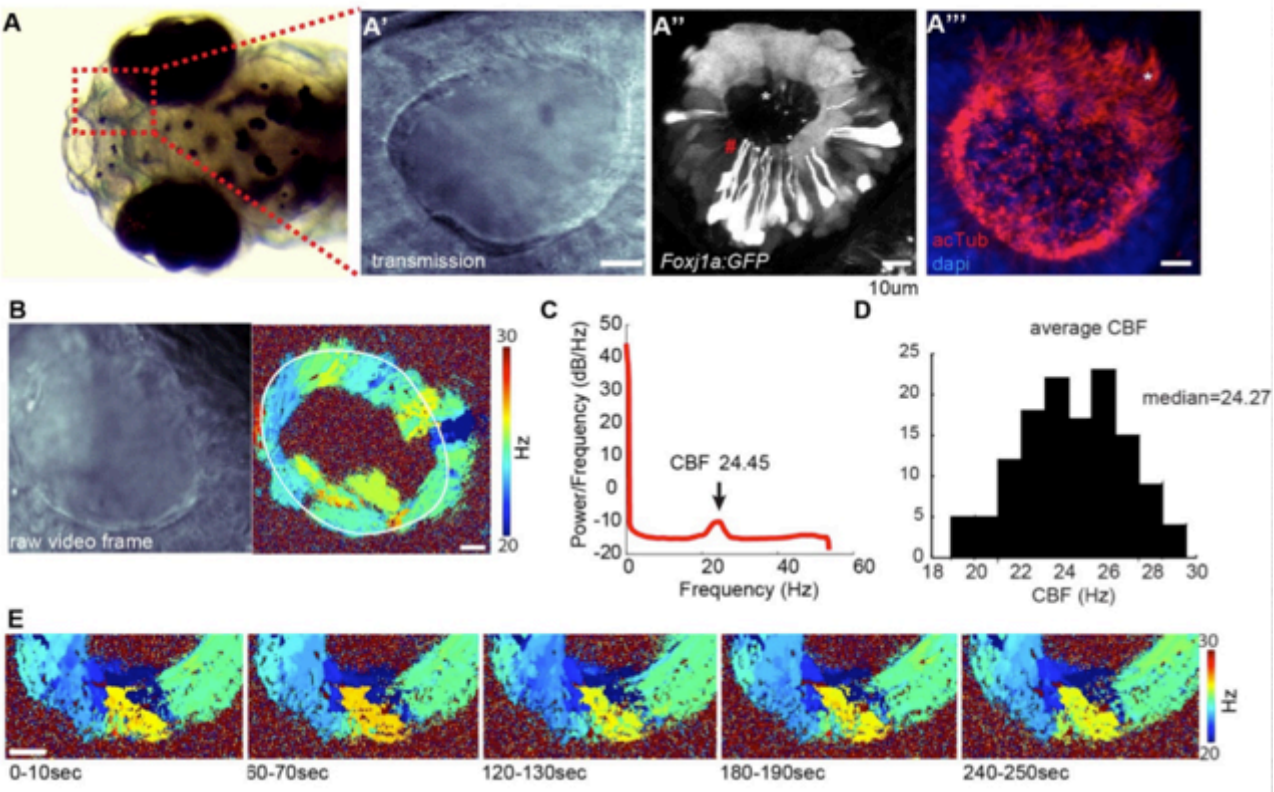

Figure 5.1. Multiciliated cells in the nose pit of 4 days old zebrafish larvae are spatially organized and beat their cilia at a distinct frequency. (A) Representative image of a 4 days old zebrafish larvae. The nose pit, indicated by the red dashed inlet, appears as a hollow cup in transmission microscopy (A'). (A'') Two photon microscopy image of the nose pit in *Foxj1a:GFP* zebrafish. Cuboidal-shaped multiciliated cell with motile cilia are indicated by "*" and pear-shaped ciliated olfactory receptor neurons are indicated by "#". (A''') Confocal microscopy image of the nose pit, where all cilia are labelled by acetyl tubulin staining (red) and cell nuclei are labelled with DAPI staining [67]. Note longer motile cilia indicated by "*". (B) Fast (100Hz) transmission microscopy recordings in the nose pit of a representative animal (left) showed that the patches of motile cilia beat at frequencies ranging from 20Hz to 30Hz (right, nose cavity is indicated with a white line) , with an average of 24.45 Hz as shown by power spectral density analysis (C). (D) Average ciliary beating frequency from 130 zebrafish larvae range from 19 to 29Hz, with a median of 24.27Hz. (E) Beating frequency is stable during 5 min, reported for one representative pit at 1min intervals. Scale bars are 10µm.

5.3.2. Stereotypical Flow generated by motile cilia

In order to further characterize the precise beating pattern, velocity and direction of motile cilia, we identified an enhancer trap line, that sparsely labels MCCs in the nose pit by green fluorescent

protein (*hspGGFF19b;UAS:GFP*). Light sheet microscopy recordings with high spatial and temporal resolution (900Hz) showed that motile cilia beat in an asymmetric manner (Fig 5.2A). This asymmetric beating is composed of a fast effective stroke and a slow recovery stroke, which is in line with other studies on motile cilia of MCCs [86]. We observed that during the effective stroke, cilia extend fully with a maximal velocity of 1.9 +/- 0.3mm/s (n=4 fishes, 9 cells). Later, during the slow recovery stroke, they retract by 180 degrees and stay close to the cell body, creating a whip-like motion (Fig 5.2A). This high resolution measurement showed that the complete ciliary stroke for an individual MCC lasts approximately 40ms which is in line with the mean CBF (24Hz) obtained by transmission light microscopy (Fig 5.1B).

Previous studies suggest that the asymmetric beating of motile cilia is important for generating complex flow patterns in brain ventricles [87] and in the mucosa of multiple tissues [86]. In order to visualize the flow generated by ciliary beating in zebrafish nose pit we imaged the flow fields from a dorsal view using fluorescent particles and confocal microscopy. We quantified the flow fields by using particle image velocimetry (PIV), an analytical method that is widely used in the field of fluid mechanics [94-96]. PIV measurements revealed that ciliary beating generates a strong and stereotypical flow around the snout that draws water medially from the heading direction of the larvae and ejects laterally towards both sides (Fig 5.2B). We observed that these microscopic jet turbines, powered by the motile cilia of only 8.7+/-2.2 μm in size, can attract water to the nose pits from more than 200 μm (Fig 5.2B). Measurements around the nose pits with faster time resolution revealed that the maximal flow velocities can go up to 120μm/s (mean is 98+/-32 μm/s) and are not significantly different at the inlet and the outlet of the olfactory pit (Fig 5.2C, E). We used these flow velocities to estimate the residence time of a given particle near the olfactory epithelium. Our calculation suggests that the content of the nose pit is fully exchanged within 0.41+/-0.09 sec due to the action of ciliary beating (Fig 5.1F). These flow fields are in line with the

arrangement of asymmetric beating from multiple individual MCCs around the nose pit obtained by light sheet microscopy, where MCCs located medially beats laterally toward the nose pit, and cells located laterally beats dorsally toward the eye (summarized in model Fig 5.2D). We also measured the flow fields at different depths along the medial-lateral axis. Our measurements revealed that the flow fields draw water from all directions at the medial positions of the snout (Fig 5.2G), and eject water dorsally at the lateral part of the snout (Fig 5.2H). Altogether, our analysis revealed that even though the nose pit is a rather homogenous cup at 4 days, the location and beating pattern of motile cilia allow already a medio-lateral and anterio-posterior current flow.

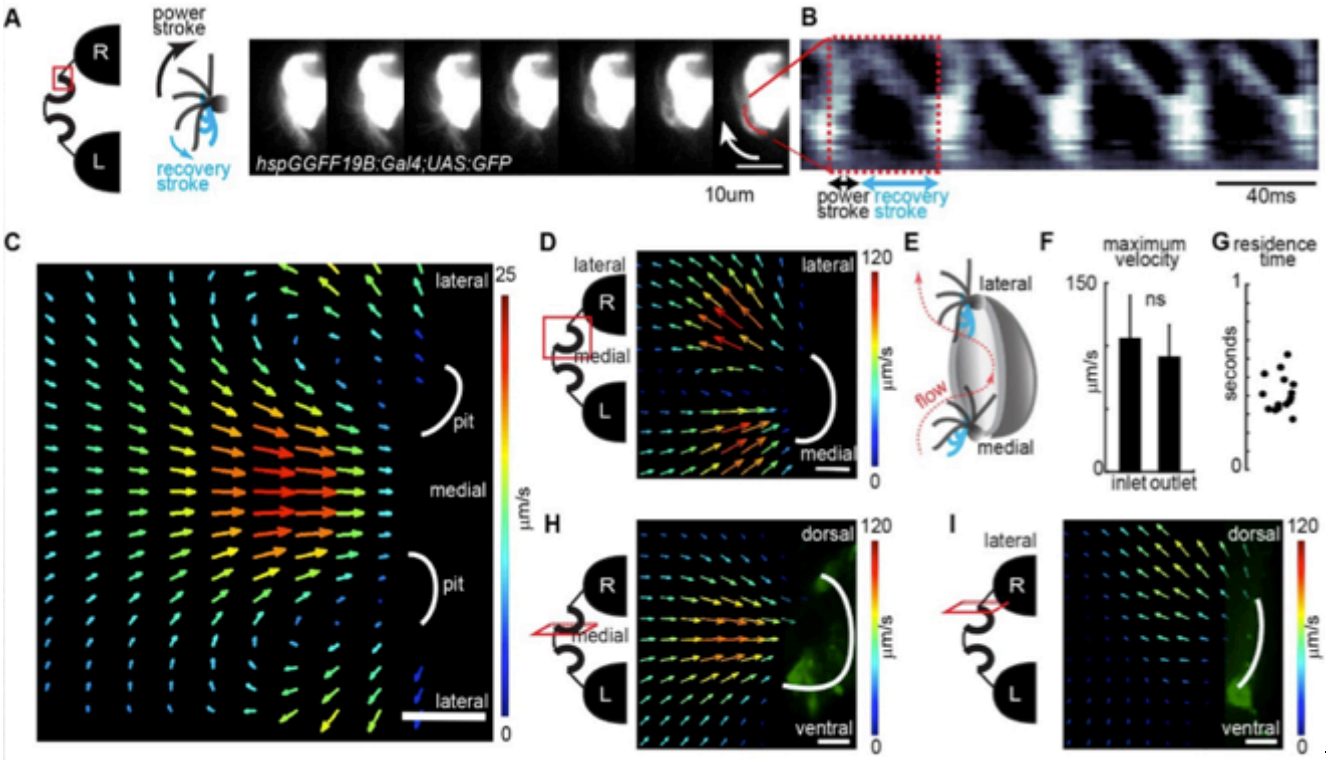

Figure 5.2. Motile cilia beat with an asymmetric stroke and generate stereotypical flow fields around the nose. (A) Beating pattern of two adjacent multiciliated cells, sparsely labelled with GFP (*hspGGFF19B:Gal4;UAS:GFP*), recorded by light sheet microscopy at 900 Hz. Red inlet on the left scheme marks the region of recording around the nose. Montage representing 7 images separated by 4.5ms on the right. Arrow marks the direction of beating. Note the asymmetric curvature of cilia during strokes as exemplified in the model on the left. (B) Kymogram of pixel intensity along the red line shows an asymmetric beating pattern composed of a fast power stroke and a slow recovery stroke. A complete beating cycle has a period of 40ms. (C) Flow fields are measured by particle image velocimetry using confocal microscopy images (2.15 Hz) of fluorescent particles around the nose pits (indicated by white lines) of 4 days old zebrafish larvae. Imaging plane viewed from dorsal. Warm colors and large arrows indicate strong flow.

Direction of the arrows indicate the direction of the flow. Note that the stereotypical flow fields generated by motile cilia attract water from medial regions into the nose pits and ejects it towards the lateral directions. (D) Close up and faster (19.6 Hz) measurements of the dorsally viewed flow fields near the right nose pit. Note high flow rates of inflow (medially) and outflow (laterally) near the nose pits. Red inlet in the scheme on the left depicts the imaged region. (E) Model summarizing the directional orientation of asymmetrically beating motile cilia along the nose pits based on light-sheet microscopy measurements of individual sparsely labelled cilia from 11 animals. Cells located medially beat towards the pit. Cells located laterally beat toward the outside of the pit. (F) Maximal flow velocities at the inlet and outlet of the nose pits are not significantly different (15 nostrils from 7 larvae). Error bars are std. (G) Residence times of particles in the nose pit measured in 15 nostrils from 7 larvae, calculated based on inflow, outflow and the volume of the nose pit. (H-I) Flow fields at the right nose pit laterally viewed at two different depths, medial (H) and lateral (I) as indicated by red inlets in the left scheme. *Foxj1a:GFP* larvae were used (n=4). Note that (H) at medial plane inflow attracts water from all directions, (I) at the lateral plane outflow ejects water mostly dorsally. Scale bars are 10µm (A), 100µm (C) and 20µm (D-I). p-value by signrank test, ns=non significant

Next, we set to verify the causal relationship between ciliary beating and the flow fields around the nose by using a zebrafish mutant line (*schmalhans, smh*) that displays ciliary motility defects in motile cilia of various tissues [97]. Importantly, this specific mutation was shown to retain the general structure and length of both primary and motile cilia, albeit the stasis in motile cilia [97]. In line with these findings, our acetyl-tubulin staining confirmed the presence of cilia in the nose pit of *smh-/-* homozygous mutant (Fig 5.3A, A'). Moreover we observed a complete paralysis of motile cilia in our transmission microscopy measurements in the nose (Fig 5.3B, B'). Consequently, the stasis in motile cilia of *smh-/-* zebrafish resulted in a loss of the flow fields around the nose pits and the snout (Fig 5.3C, C') in PIV measurements. Altogether, these results demonstrate a direct role of motile ciliary beating in the generation of the flow fields around the nose.

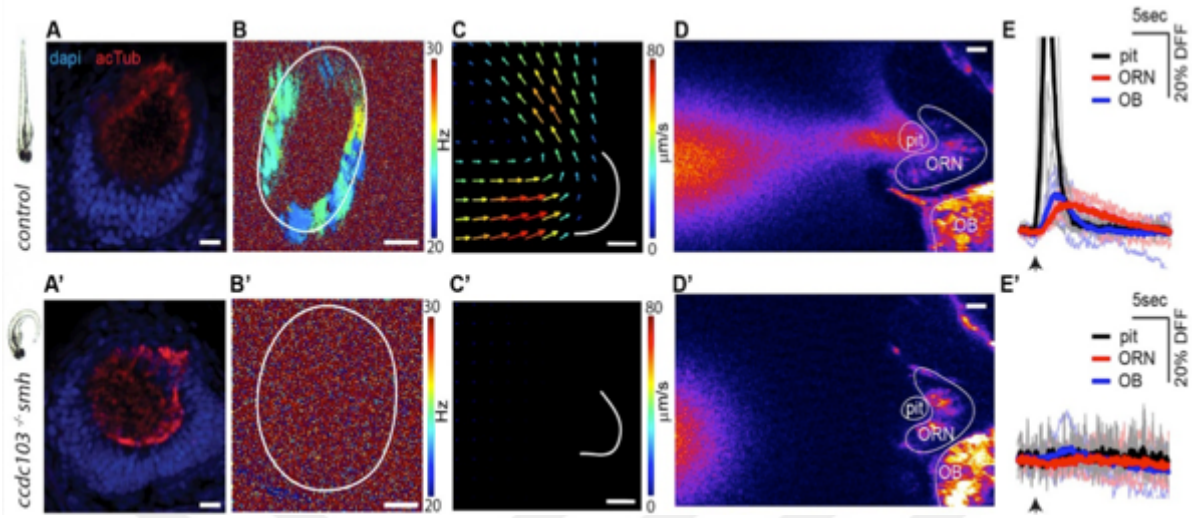

Figure 5.3. Lack of ciliary beating in the multiciliated cells of *smh-/-* zebrafish diminishes flow fields around the snout, hampers attraction of odors to nose pit and consequently impairs neural responses to odors in stagnant environments. (A-A') *Smh-/-* larvae that are identified by their bend body axis (left) have a normal ciliary distribution in the nose pit, confirmed by acetyl tubulin staining. (B-B') No ciliary beating (n=9 for *smh -/-* CBF=none, n=10 control CBF=23.9+/-1.2Hz) and (C-C') no flow fields (n=3 for *smh -/-* and controls) are detected in the nose pit of *smh-/-* larvae, when compared to control animals. (D-E) Fluorescently labelled food odor is released from a capillary using a microinjector and odor flow dynamics and neural responses to odors are imaged using two-photon microscopy in *HuC:GCamp6s* zebrafish expressing transgenic calcium indicators. Raw video frames following microinjection were averaged (D,D'). Note that the flow generated by motile cilia can attract odors to the nose pit in control zebrafish (D) and elicit odor responses in ORN and OB (E). Whereas *smh -/-* larvae fail to attract odors (D') and no odor responses are present at the level of ORNs and OB (E'). (E-E') Time course of odor dynamics in the nose pit and neural responses to odors in control (E) and *smh-/-* (E') larvae, represented as percentage change of fluorescence over time (ΔF/F). Note that the odor is rapidly attracted and ejected from the nose pit (black), which results in transient odor responses in ORNs (red) and OB [67]. In contrast , *smh-/-* larvae do not attract odor to the nose pit and thus ORN and OB do not display calcium activity. Light lines are individual traces, dark lines are average, black arrows mark the time of odor injections. n=7 (wt) & 6 (smh -/-). All scale bars are 20µm.

Motile cilia in the nose are conserved across most vertebrates from fish to rodents [91, 92, 98, 99]. In order to test whether motile-cilia driven flow exists in the nose of other teleost fish species, we performed similar experiments in another teleost fish, salmon. The olfactory pits of salmon larvae at 4 days post hatching are located at the snout and consist of a channel with one anterior and one posterior opening. Our acetyl-tubulin staining in salmon larvae revealed positively labelled cilia in various locations around the nose, with an enrichment at the posterior opening. Next we observed that cilia at the posterior opening are motile and beat at an average frequency of 26.5+/-2.0 Hz, in

line with the values obtained in zebrafish. Finally, PIV measurements revealed a strong anterio-posterior current through the nose with higher velocities at the inlet than the outlet. Altogether, our results revealed that the motile cilia in the nose of several aquatic vertebrates have similar properties and generate robust and stereotyped flow fields around the nose, which indicates an important function for this highly conserved phenomenon.

5.3.3. Lack of ciliary beating

The overall shape and direction of the flow fields around the nose pits suggest that the motile cilia of the nose may attract odors to the olfactory pit. We hypothesized that this phenomenon can facilitate detection of odors especially in stagnant aquatic environments, for example a zebrafish larvae at rest in a pond. In order to test this hypothesis, we delivered a fluorescently labelled odor using a pressure injector and we simultaneously measured the odor dynamics and the odor evoked neural responses using two-photon microscopy, in zebrafish expressing calcium indicator GCamp6s panneuronally (*HuC:Gcamp6s*) [100]. Our results showed that flow fields generated by the beating of motile cilia can attract odors from over 200µm away from the nose pit (Fig 5.3E). Moreover, we observed that these flow fields facilitate odor detection and elicit odor responses at ORNs and at the first relay of odor information in the brain, the olfactory bulb (OB). On the contrary, *smh-/-* zebrafish failed to attract odors to the nose and showed no detectable odor responses in ORNs or in OB (Fig 5.3E'). Altogether, our data shows that the motile ciliary beating generates flow and attracts odors to the nose pit facilitating odor detection especially in stagnant aquatic environments, when the fish is at rest.

5.4. Discussion

Altogether, our results showed that detecting odors in stagnant and turbulent environments

depends on the fluid dynamics properties of the nose pit. This is particularly important for aquatic vertebrates since their olfactory cavity is often not connected to respiration and the passive diffusion of odorant molecules in water is slow. In aquatic animals, odors can be driven into the nose by various mechanisms [98, 99]. For example, differential water pressure between incurrent and excurrent nostrils can result from the forward motion of the fish or incoming flow. As an alternative solution few aquatic vertebrates evolved accessory sacs in their olfactory organs which can be expended and compressed. Lobsters were shown to move their antennules to draw water into the olfactory epithelium [101]. In addition to these potential solutions that are evolved to improve aquatic olfaction, here we propose motile cilia-driven flow as an efficient and fast olfactory sampling method that is used by teleost fishes. A similar mechanism may potentially be utilized in mammalian nose. Our data showed for the first time how the motile cilia decorating the nose pit act as a very powerful water turbine and generate strong and robust flow fields that allow fish to quickly exchange the content of the nose. Importantly, this mechanism increases the sensitivity and temporal resolution of odor computations both in stagnant and running aquatic environments and does not require muscle contraction. Interestingly in hagfish and lampreys, which are considered evolutionary primitive fish species, the respiratory flow initiated by the velum contraction passes through the olfactory chamber toward the gills and thus draw odors [102]. Thus, from an evolutionary perspective, it appears that cilia driven flow in the nose pit is rather novel and may underlie a powerful and energy efficient mechanism to draw odors in the nose. Altogether, we propose that this mechanism has evolved to facilitate better sampling of dynamically changing odor plumes and thereby enhancing the temporal resolution of olfactory computations. It is an intriguing correlation that the motile cilia in the nose of most vertebrates and in the airways of mammals generate ciliary beating with similar principles, highlighting a possible evolutionary relationship between these structures.

Thanks to the optical accessibility of zebrafish nose pit, here, we could fully characterize how motile cilia beat to generate a robust flow in an intact organism. First, the asymmetric beating pattern that we show for the motile cilia of the nose is conserved across many MCCs located along the brain ventricles, spinal cord and respiratory tract [86]. Second, the average CBF of zebrafish and salmon olfactory MCCs is rather uniform across individuals and lies between 20 and 30Hz. In contrast, big variations in CBF from 10 to 40Hz were reported for epithelia depending on the specimen preparation in past studies. Third, we showed that flow characteristics resulting from the specific location and asymmetric beating of motile cilia are tailored to the organ's need. In the brain ventricles, beating cilia can concentrate molecules locally or prevent entry to other ventricular area by generating boundaries [87]. Our findings suggest here that the robust and directional flow, generated by motile cilia in the nose pit, guarantees an efficient exposure of ORNs to odors but for a restricted time. Even though it is now clear that fluid dynamics are regulated by the power and directionality of ciliary beating, the cellular and molecular mechanisms underlying the establishment of asymmetric ciliary beating remain to be fully understood. Altogether, having such a conserved ciliary function outside the body of a living vertebrate provides a plethora of methods to image and interfere with ciliary function, and thus could serve as model to better understand the chemical, physical and genetic factors regulating ciliary beating.

Conclusion

I have shown that investigation of biological flows revealed mysteries of species in nature. The mysteries might be about cardiovascular systems, pumping system, feeding system, or olfaction system of the species in nature as I discussed in previous chapters. These findings are crucial for engineers and scientists since the mysteries that we found can be used for bio-inspired design of engineering products. To explore biological flows, I have used diverse methods for imaging such as confocal microscopy, OCT, light sheet microscopy, light microscopy, or fluorescent microscopy. I used DaVis PIV algorithm for vector calculation. I used velocity information of biological flows to calculate the pressure and force exposed by the flow. Then we used the flow results to find out its relation with other systems of the species such as neural system of zebrafish or gene expressions in cardiovascular system of chicken embryo.

In cardiovascular system of chicken embryo, OCT images were used to visualize the pulsatile flow of the RBCs and velocity vectors were calculated by using OCT images of RBCs for three different embryonic stages. Then I calculated peak WSS during cardiac cycles for the stages. We compared my hemodynamics results with gene expressions of mechano-sensitive genes. KLF-2 and NOS-3 showed similar behavior with hemodynamic peak WSS between three different stages. We investigated genetic expressions, vascular growth, and hemodynamics together in three different stages for the first time in the literature.

I have used planar PIV to explore the external flow structures of mussels. We found that mussels can robustly control their exhalant and inhalant flows. Mussels can change their exhalant flow from single potential core region to double or vice versa. For the first time in literature, we measure the inhalant flow at coronal plane and explored the suction performance of mussels in detail. Energy dissipation map in sagittal plane showed that there is no interference

between inhalant and exhalant flows, which may decrease the pumping efficiency of mussels.

To investigate the suction flow of zebrafish embryo, we used OCT for imaging of fish mouth and fluorescent stereomicroscope for imaging fluorescent PIV particles. Morphology of mouth and feeding performance of zebrafish embryo was investigated at the same time. As in the suction performance, olfaction of zebrafish embryo is explored with fluid dynamics in olfactory organ. Flow is visualized with confocal microscopy, light sheet microscopy, and two-photon microscopy. We investigated that asymmetric beating of motile cilia on the nose of zebrafish embryos generates three-dimensional flows. The flow helps zebrafish to quickly exchange the odor in the nose. Temporal resolution and sensitivity is controlled and improved by the flow. This research put a new research field on the stage: Neuro-fluid dynamics.

References

1. Conway, E.M., D. Collen, and P. Carmeliet, *Molecular mechanisms of blood vessel growth.* Cardiovasc Res, 2001. **49**(3): p. 507-21.
2. Anwar, M.A., et al., *The effect of pressure-induced mechanical stretch on vascular wall differential gene expression.* J Vasc Res, 2012. **49**(6): p. 463-78.
3. Davis, A., J. Izatt, and F. Rothenberg, *Quantitative measurement of blood flow dynamics in embryonic vasculature using spectral Doppler velocimetry.* The Anatomical Record, 2009. **292**(3): p. 311-319.
4. Poelma, C., et al., *In vivo blood flow and wall shear stress measurements in the vitelline network.* Experiments in fluids, 2008. **45**(4): p. 703-713.
5. Poelma, C., et al., *Accurate blood flow measurements: are artificial tracers necessary?* PloS one, 2012. **7**(9): p. e45247.
6. Garcia, M.D. and I.V. Larina, *Vascular development and hemodynamic force in the mouse yolk sac.* Front Physiol, 2014. **5**: p. 308.
7. Yelbuz, T.M., et al., *Optical coherence tomography: a new high-resolution imaging technology to study cardiac development in chick embryos.* Circulation, 2002. **106**(22): p. 2771-4.
8. Chen, C.-Y., Menon PG, Kowalski W, Pekkan K. , *Time-resolved OCT-uPIV: a new microscopic PIV technique for non-invasive depth-resolved pulsatile flow profile acquisition* Exp Fluids 2013. **54**: p. 1426-x.
9. Jørgensen, C.B., *Quantitative aspects of filter feeding in invertebrates.* Biological Reviews, 1955. **30**(4): p. 391-453.
10. Jørgensen, C.B., *Fluid mechanics of the mussel gill: the lateral cilia.* Marine Biology, 1982. **70**(3): p. 275-281.
11. Jørgensen, C.B., *Fluid mechanical aspects of suspension feeding.* Mar. Ecol. Prog. Ser, 1983. **11**: p. 89-103.
12. Bach, D., et al., *A review of selected pumping systems in nature and engineering—potential biomimetic concepts for improving displacement pumps and pulsation damping.* Bioinspiration & biomimetics, 2015. **10**(5): p. 051001.
13. Riisgård, H.U. and P.S. Larsen, *Minireview: Ciliary filter feeding and bio-fluid mechanics—present understanding and unsolved problems.* Limnology and Oceanography, 2001. **46**(4): p. 882-891.
14. Riisgård, H.U., P.S. Larsen, and N.F. Nielsen, *Particle capture in the musselMytilus edulis: The role of latero-frontal cirri.* Marine Biology, 1996. **127**(2): p. 259-266.
15. Seo, E., et al., *Magnetic resonance imaging analysis of water flow in the mantle cavity of live Mytilus galloprovincialis.* The Journal of experimental biology, 2014. **217**(13): p. 2277-2287.
16. Frank, D.M., et al., *Application of particle image velocimetry to the study of suspension feeding in marine invertebrates.* Marine and Freshwater behaviour and physiology, 2008. **41**(1): p. 1-18.
17. Troost, K., et al., *Feeding current characteristics of three morphologically different bivalve suspension feeders, Crassostrea gigas, Mytilus edulis and Cerastoderma edule, in relation to food competition.* Marine Biology, 2009. **156**(3): p. 355-372.
18. Riisgård, H.U., et al., *The exhalant jet of mussels Mytilus edulis.* Marine Ecology Progress Series, 2011. **437**: p. 147-164.
19. China, V. and R. Holzman, *Hydrodynamic starvation in first-feeding larval fishes.* Proceedings of the National Academy of Sciences, 2014. **111**(22): p. 8083-8088
20. Holzman, R., et al., *Hydrodynamic constraints of suction feeding in low Reynolds numbers, and the critical period of larval fishes.* Integr. Comp. Biol., 2015. **55**(1): p. 48-61.
21. Yaniv, S., D. Elad, and R. Holzman, *Suction-feeding across fish life stages: Flow dynamics from larvae to adults and implications for prey capture.* Journal of Experimental Biology, 2014. **217**: p. 3748-3757.

22. Day, S.W., et al., *Morphology, kinematics, and dynamics: The mechanics of suction feeding in fishes.* Integr. Comp. Biol., 2015. **55**(1): p. 21-35.
23. Day, S.W., et al., *Spatial and temporal patterns of water flow generated by suction-feeding bluegill sunfish Lepomis macrochirus resolved by Particle Image Velocimetry.* Journal of Experimental Biology, 2005. **208**(14): p. 2661-2671.
24. Holzman, R., et al., *Scaling of suction-induced flows in bluegill: morphological and kinematic predictors for the ontogeny of feeding performance.* Journal of Experimental Biology, 2008. **211**: p. 2658-2668.
25. Fliegauf, M., T. Benzing, and H. Omran, *When cilia go bad: cilia defects and ciliopathies.* Nat Rev Mol Cell Biol, 2007. **8**(11): p. 880-93.
26. Berbari, N.F., et al., *The primary cilium as a complex signaling center.* Curr Biol, 2009. **19**(13): p. R526-35.
27. Veening, J.G. and H.P. Barendregt, *The regulation of brain states by neuroactive substances distributed via the cerebrospinal fluid; a review.* Cerebrospinal Fluid Res, 2010. **7**: p. 1.
28. Stannard, W. and C. O'Callaghan, *Ciliary function and the role of cilia in clearance.* J Aerosol Med, 2006. **19**(1): p. 110-5.
29. le Noble, F., et al., *Control of arterial branching morphogenesis in embryogenesis: go with the flow.* Cardiovasc Res, 2005. **65**(3): p. 619-28.
30. Coultas, L., K. Chawengsaksophak, and J. Rossant, *Endothelial cells and VEGF in vascular development.* Nature, 2005. **438**(7070): p. 937-45.
31. Burridge, K.A. and M.H. Friedman, *Environment and vascular bed origin influence differences in endothelial transcriptional profiles of coronary and iliac arteries.* Am J Physiol Heart Circ Physiol, 2010. **299**(3): p. H837-46.
32. Buschmann, I., et al., *Pulsatile shear and Gja5 modulate arterial identity and remodeling events during flow-driven arteriogenesis.* Development, 2010. **137**(13): p. 2187-96.
33. Hierck, B.P., et al., *Primary cilia sensitize endothelial cells for fluid shear stress.* Dev Dyn, 2008. **237**(3): p. 725-35.
34. Fujimoto, J.G., *Optical coherence tomography for ultrahigh resolution in vivo imaging.* Nat Biotechnol, 2003. **21**(11): p. 1361-7.
35. Yap, C.H., X. Liu, and K. Pekkan, *Characterization of the vessel geometry, flow mechanics and wall shear stress in the great arteries of wildtype prenatal mouse.* PLoS One, 2014. **9**(1): p. e86878.
36. Banjo, T., et al., *Haemodynamically dependent valvulogenesis of zebrafish heart is mediated by flow-dependent expression of miR-21.* Nat Commun, 2013. **4**: p. 1978.
37. Hove, J.R., et al., *Intracardiac fluid forces are an essential epigenetic factor for embryonic cardiogenesis.* Nature, 2003. **421**(6919): p. 172-7.
38. Kowalski WJ, T.N., Chen C-Y, Keller BB, Pekkan K. . *Simultaneous real-time quantification of blood flow and vascular growth in the chick embryo using optical coherence tomography* in *SPIE* 2014.
39. Goktas, S., et al., *Hemodynamic flow visualization of early embryonic great vessels using muPIV.* Methods Mol Biol, 2015. **1189**: p. 17-30.
40. Al-Roubaie, S., et al., *Rheology of embryonic avian blood.* Am J Physiol Heart Circ Physiol, 2011. **301**(6): p. H2473-81.
41. Pelosi, P., *The role of perireceptor events in vertebrate olfaction.* Cell Mol Life Sci, 2001. **58**(4): p. 503-9.
42. Hu, N. and B.B. Keller, *Relationship of simultaneous atrial and ventricular pressures in stage 16-27 chick embryos.* Am J Physiol, 1995. **269**(4 Pt 2): p. H1359-62.
43. Ursem, N.T., et al., *Dorsal aortic flow velocity in chick embryos of stage 16 to 28.* Ultrasound Med Biol, 2001. **27**(7): p. 919-24.
44. Midgett, M., S. Goenezen, and S. Rugonyi, *Blood flow dynamics reflect degree of outflow tract banding in Hamburger-Hamilton stage 18 chicken embryos.* J R Soc Interface, 2014. **11**(100): p. 20140643.
45. Groenendijk, B.C., et al., *The role of shear stress on ET-1, KLF2, and NOS-3 expression in the*

developing cardiovascular system of chicken embryos in a venous ligation model. Physiology (Bethesda), 2007. **22**: p. 380-9.
46. Kowalski, W.J., et al., *Critical transitions in early embryonic aortic arch patterning and hemodynamics.* PLoS One, 2013. **8**(3): p. e60271.
47. Jørgenson, C.B., *Biology of suspension feeding.* 1966.
48. Wright, R.T., et al., *Field and laboratory measurements of bivalve filtration of natural marine bacterioplankton1*. Limnology and oceanography, 1982. **27**(1): p. 91-98.
49. Meyhöfer, E., *Comparative pumping rates in suspension-feeding bivalves.* Marine Biology, 1985. **85**(2): p. 137-142.
50. Riisgård, H.U. and P.S. Larsen, *Filter-feeding in marine macro-invertebrates: pump characteristics, modelling and energy cost.* Biological Reviews of the Cambridge Philosophical Society, 1995. **70**(1): p. 67-106.
51. Riisgård, H.U. and P.S. Larsen, *Comparative ecophysiology of active zoobenthic filter feeding, essence of current knowledge.* Journal of Sea Research, 2000. **44**(3): p. 169-193.
52. Riisgård, H.U., P. Funch, and P.S. Larsen, *The mussel filter–pump–present understanding, with a re-examination of gill preparations.* Acta Zoologica, 2015. **96**(3): p. 273-282.
53. Nielsen, N.F., et al., *Fluid motion and particle retention in the gill of Mytilus edulis: video recordings and numerical modelling.* Marine Biology, 1993. **116**(1): p. 61-71.
54. Brennen, C. and H. Winet, *Fluid mechanics of propulsion by cilia and flagella.* Annual Review of Fluid Mechanics, 1977. **9**(1): p. 339-398.
55. Jørgensen, C.B., et al., *Ciliary and mucus-net filter feeding, with special reference to fluid mechanical characteristics.* Mar. Ecol. Prog. Ser, 1984. **15**(3): p. 283-292.
56. Gueron, S. and N. Liron, *Ciliary motion modeling, and dynamic multicilia interactions.* Biophysical journal, 1992. **63**(4): p. 1045.
57. Cannuel, R., et al., *Gill development and its functional and evolutionary implications in the blue mussel Mytilus edulis (Bivalvia: Mytilidae).* The Biological Bulletin, 2009. **217**(2): p. 173-188.
58. Aksit, D. and B.F. Mutaf, *The gill morphology of the date mussel Lithophaga lithophaga (Bivalvia: Mytilidae).* Turkish Journal of Zoology, 2014. **38**(1): p. 61-67.
59. Jonas, S., et al., *Microfluidic characterization of cilia-driven fluid flow using optical coherence tomography-based particle tracking velocimetry.* Biomedical optics express, 2011. **2**(7): p. 2022-2034.
60. Chen, C.-Y., C.-Y. Lin, and Y.-T. Hu, *Inducing 3D vortical flow patterns with 2D asymmetric actuation of artificial cilia for high-performance active micromixing.* Experiments in Fluids, 2014. **55**(7): p. 1-9.
61. Monismith, S.G., et al., *A study of model bivalve siphonal currents.* Limnology and Oceanography, 1990. **35**(3): p. 680-696.
62. O'Riordan, C., S. Monismith, and J. Koseff, *The effect of bivalve excurrent jet dynamics on mass transfer in a benthic boundary layer.* Limnology and Oceanography, 1995. **40**(2): p. 330-344.
63. Chen, C.-Y., et al., *Analysis of early embryonic great-vessel microcirculation in zebrafish using high-speed confocal μPIV*. Biorheology, 2011. **48**(5-6): p. 305-321.
64. Chen, C.-Y., et al., *Time-resolved OCT-μPIV: a new microscopic PIV technique for noninvasive depth-resolved pulsatile flow profile acquisition.* Experiments in fluids, 2013. **54**(1): p. 1-9.
65. Pekkan, K., et al., *Characterization of zebrafish larvae suction feeding flow using μPIV and optical coherence tomography.* Experiments in Fluids, 2016. **57**(7): p. 1-7.
66. Dabiri, J.O., et al., *An algorithm to estimate unsteady and quasi-steady pressure fields from velocity field measurements.* Journal of Experimental Biology, 2014: p. jeb. 092767.
67. Bluestein, M. and L. Mockros, *Hemolytic effects of energy dissipation in flowing blood.* Medical and biological engineering, 1969. **7**(1): p. 1-16.
68. Menon, P.G., et al., *Characterization of neonatal aortic cannula jet flow regimes for improved cardiopulmonary bypass.* Journal of biomechanics, 2013. **46**(2): p. 362-372.
69. Zhang, Y., et al., *A microstructural hyperelastic model of pulmonary arteries under normo- and hypertensive conditions.* Ann Biomed Eng, 2005. **33**(8): p. 1042-52.

70. Yaniv, S., D. Elad, and R. Holzman, *Suction feeding across fish life stages: flow dynamics from larvae to adults and implications for prey capture.* The Journal of experimental biology, 2014. **217**(20): p. 3748-3757.
71. Vahl, O., *Efficiency of particle retention in Mytilus edulis L.* Ophelia, 1972. **10**(1): p. 17-25.
72. Parra, G. and M. Yúfera, *Feeding, physiology and growth responses in first-feeding gilthead seabream (Sparus aurata L.) larvae in relation to prey density.* Journal of Experimental Marine Biology and Ecology, 2000. **243**(1): p. 1-15.
73. Higham, T.E., S.W. Day, and P.C. Wainwright, *Multidimensional analysis of suction feeding performance in fishes: fluid speed, acceleration, strike accuracy and the ingested volume of water.* Journal of Experimental Biology, 2006. **209**(14): p. 2713-2725.
74. Staab, K.L., et al., *Independently evolved upper jaw protrusion mechanisms show convergent hydrodynamic function in teleost fishes.* The Journal of experimental biology, 2012. **215**(9): p. 1456-1463.
75. Day, S.W., T.E. Higham, and P.C. Wainwright, *Time resolved measurements of the flow generated by suction feeding fish.* Experiments in Fluids, 2007. **43**(5): p. 713-724.
76. Chen, C.A. and K. Pekkan, *High-speed three-dimensional characterization of fluid flows induced by micro-objects in deep microchannels.* BioChip Journal, 2013. **7**(2): p. 95-103.
77. Kowalski, W.J., et al., *Left atrial ligation alters intracardiac flow patterns and the biomechanical landscape in the chick embryo.* Dev Dyn, 2014. **243**(5): p. 652-62.
78. Chen, C.Y., et al., *Time-resolved OCT-μPIV: a new microscopic PIV technique for noninvasive depth-resolved pulsatile flow profile acquisition.* Experiments in Fluids, 2013. **54**(1): p. 1-9.
79. Hernandez, L.U., *Intraspecific scaling of feeding mechanics in an ontogenic series of zebrafish, Danio rerio.* The Journal of Experimental Biology, 2000. **203**: p. 3033-3043.
80. Gemmell, B.J., D. Adhikari, and E.K. Longmire, *Volumetric quantification of fluid flow reveals fish's use of hydrodynamic stealth to capture evasive prey.* J R Soc Interface, 2014. **11**(90): p. 20130880.
81. Dabiri, J.O., et al., *An algorithm to estimate unsteady and quasi-steady pressure fields from velocity field measurements.* The Journal of Experimental Biology, 2014. **217**: p. 331-336.
82. Rønnestad, I., et al., *Feeding behaviour and digestive physiology in larval fish: current knowledge, and gaps and bottlenecks in research.* Reviews in Aquaculture, 2013. **5**(Supplement s1): p. S59–S98.
83. Fuiman, L.A. and P.A. Webb, *Ontogeny of routine swimming activity and performance in zebra danios (Teleostei: Cyprinidae).* Anim. Behav., 1988. **36**: p. 250–261.
84. Gibb, A.C., *Do flatfish feed like other fishes? A comparative study of percomorph prey-capture kinematics.* J. Exp. Biol., 1997. **200**: p. 2841–2859.
85. Hildebrandt, F., T. Benzing, and N. Katsanis, *Ciliopathies.* N Engl J Med, 2011. **364**(16): p. 1533-43.
86. Brooks, E.R. and J.B. Wallingford, *Multiciliated cells.* Curr Biol, 2014. **24**(19): p. R973-82.
87. Faubel, R., et al., *Cilia-based flow network in the brain ventricles.* Science, 2016. **353**(6295): p. 176-8.
88. Shah, A.S., et al., *Motile cilia of human airway epithelia are chemosensory.* Science, 2009. **325**(5944): p. 1131-4.
89. Johanson, C.E., et al., *Multiplicity of cerebrospinal fluid functions: New challenges in health and disease.* Cerebrospinal Fluid Res, 2008. **5**: p. 10.
90. Getchell, T.V., F.L. Margolis, and M.L. Getchell, *Perireceptor and receptor events in vertebrate olfaction.* Prog Neurobiol, 1984. **23**(4): p. 317-45.
91. Harkema, J.R., S.A. Carey, and J.G. Wagner, *The nose revisited: a brief review of the comparative structure, function, and toxicologic pathology of the nasal epithelium.* Toxicol Pathol, 2006. **34**(3): p. 252-69.
92. Hansen, A. and E. Zeiske, *The peripheral olfactory organ of the zebrafish, Danio rerio: an ultrastructural study.* Chem Senses, 1998. **23**(1): p. 39-48.
93. Kermen, F., et al., *Neural circuits mediating olfactory-driven behavior in fish.* Front Neural

Circuits, 2013. **7**: p. 62.
94. Adrian, R.J., *Twenty years of particle image velocimetry.* Experiments in Fluids, 2005. **39**(2): p. 159-169.
95. Chen, C.Y., et al., *Analysis of early embryonic great-vessel microcirculation in zebrafish using high-speed confocal muPIV.* Biorheology, 2011. **48**(5): p. 305-21.
96. Pekkan, K., et al., *Characterization of zebrafish larvae suction feeding flow using mu PIV and optical coherence tomography.* Experiments in Fluids, 2016. **57**(7).
97. Panizzi, J.R., et al., *CCDC103 mutations cause primary ciliary dyskinesia by disrupting assembly of ciliary dynein arms.* Nat Genet, 2012. **44**(6): p. 714-9.
98. Kasumyan, A., *The olfactory system in fish: structure, function, and role in behavior.* Journal of Ichthyology, 2004. **44**(2): p. S180.
99. Cox, J.P., *Hydrodynamic aspects of fish olfaction.* J R Soc Interface, 2008. **5**(23): p. 575-93.
100. Quirin, S., et al., *Calcium imaging of neural circuits with extended depth-of-field light-sheet microscopy.* Opt Lett, 2016. **41**(5): p. 855-8.
101. Koehl, M.A., et al., *Lobster sniffing: antennule design and hydrodynamic filtering of information in an odor plume.* Science, 2001. **294**(5548): p. 1948-51.
102. Holmes, W.M., et al., *Three-dimensional structure of the nasal passageway of a hagfish and its implications for olfaction.* Anat Rec (Hoboken), 2011. **294**(6): p. 1045-56.

Appendix A. PIV Processing Protocols

Protocol E1 - Creating Mask by Using Existing Image Sets for PIV Analyses – With application example

We have RGB image set including 2 fluorescent channels as red (blood cells) and green (tissue). In this application, we want to perform PIV analyses on red channel and use green channel as a mask. Details of PIV analyses are not explained in this protocol but preparation of green channel as a mask is explained.

We can use ImageJ in the first stage for splitting channels. We are going to split channels in ImageJ and export them as TIFF image sequences. Then we are going to use DaVis for converting green channel to mask images.

1) Open ImageJ and import data set with "File => Open => *directory of data set*". We will get images with red and green channel (see Fig. A.1A). To split the red and green channel, we use "Image => Color => Split Channels". This step gives us separate two image sets, one for red channel (blood cells) and one for green channels (tissue), see Fig A.1B. Use "File => Save as => Image Sequences…" to export TIFF image sequences.

Figure A.1A. Raw data. Channels can be changed by scroll bar denoted by "C". Image sequences can be altered by lower scroll bar.

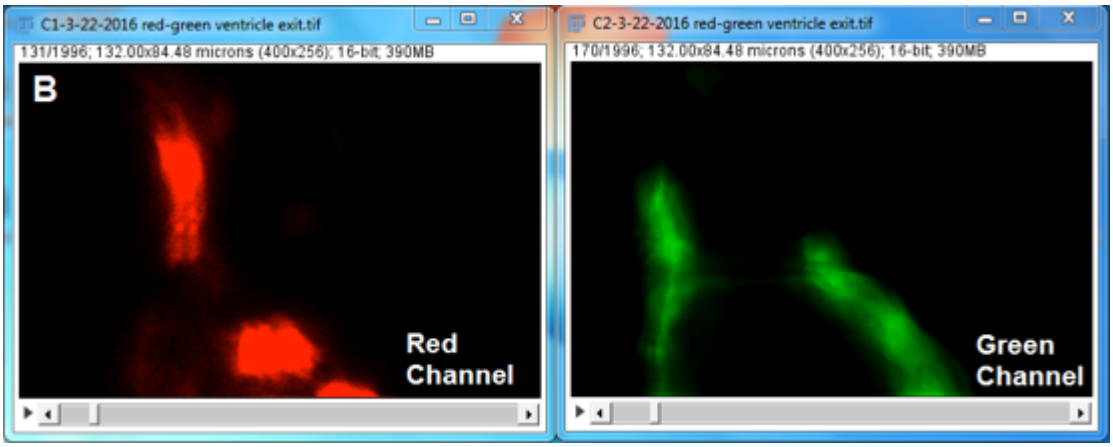

Figure A.1B. Two channels after splitting.

2) Red channel is going to be used as particle image data for PIV. We want to use green channel as mask of red channel to prevent from irrelevant velocity vectors and strain vectors. Open DaVis and import image sequences of red and green channels. Open Processing dialog for green channel.

The image set (green channel in this case) that should be used for masking needs to be processed in a manner that it contains zero intensity at those positions that should be masked out in the particle images. Adjust the intensity levels of masking regions in green channel to 0 intensity.

This can be done using following function the processing:

- Group: basic image arithmetic
- Operation: set above (below) to constant (specify the constant = 0)

3) The processed image set that should be used for masking needs to be moved into the subdirectory of the corresponding PIV particle image set (using the right mouse click on the data set and using the COPY / MOVE TO option) and renamed to MASK (using the right mouse click on the data set and using the RENAME option).

4) While PIV analyses of red channels;

For vector calculation of the particle images (red channel in this case) you need to activate the 'Use Mask' option on the 'Vector calculation parameter' card, to activate the 'Load mask from file' option on the 'Define mask' card and to select the 'Individual mask for each image from subfolder MASK.SET' option on the 'Load mask from file' card.

Protocol E2 - Image Recording via PIV Davis Software and Leica Stereo microscope

1) Move blue button from off to on before starting the computer

Figure A.2. Blue power button of PIV computer

2) Push the button to start computer

Figure A.3. Start button of PIV computer

3) Wait for opening computer (Fig. A.4A), move the button of the camera from off to on (Fig. A.4B)

A B

Figure A.4. (A) Desktop of PIV computer (B) Power button of sCMOS

4) Take the dongle (USB – Fig. A.5A) which is kind of key of the Davis software from the folder (Fig. A.5B) , plug it to computer (Fig. A.5C)

A B

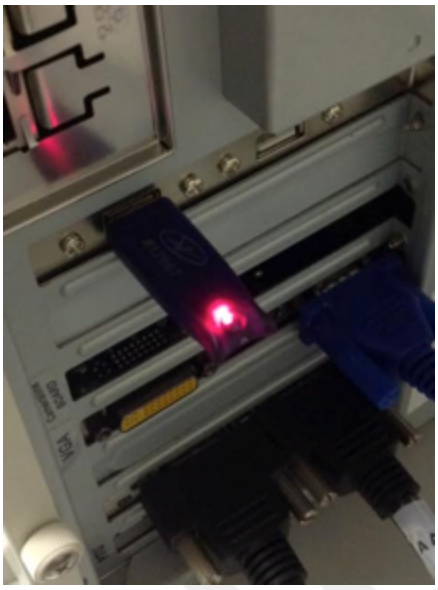

C

Figure A.5. (A) USB dongle of DaVis (B) the file where the dongle is located (C) The dongle is located

5) We are ready to start Davis click on Davis icon on the desktop

Figure A.6. DaVis icon on the desktop

6) After a few seconds, the notification appears. Click “Login”

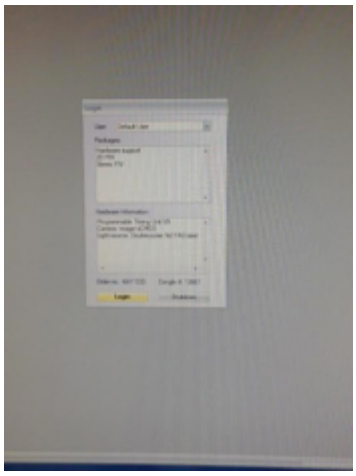

Figure A.7. Login subwindow of DaVis

7) Welcome to Davis. Click "New" to open your project file (Fig. A.8A). Then the notification appears, adjust "Imaging" and click "OK"(Fig. A.8B)

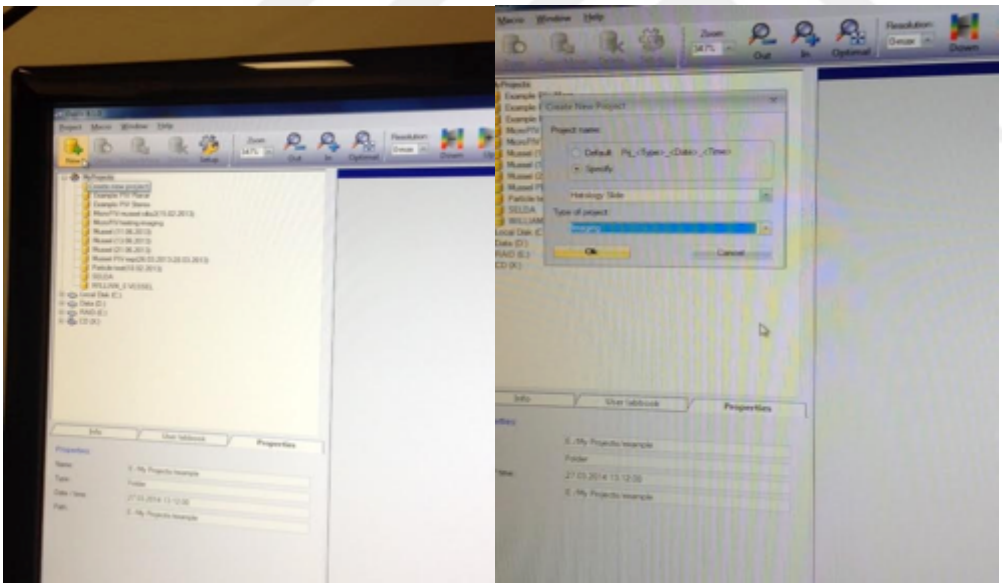

A **B**

Figure A.8. (A) New project button in DaVis (B) Subwindow for naming the project

8) Before starting the recording, you should set up your experiment and start the microscope. Study the user manual of the microscope before operation with microscope.

9) You are in your folder. Click "recording" to initiate recording operation

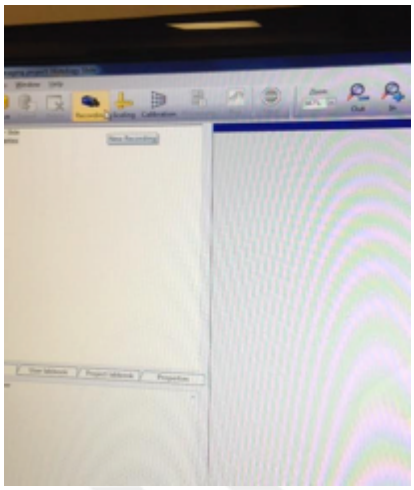

Figure A.9. Recording icon in DaVis

10) You are going to see two icons under "Live Mode". Click on the icon on the left to take just one image via camera. Click on the icon on the right to take live sequential images just before the recording (Fig. A.10A). Click on "STOP" button to stop live mode (Fig. A.10B). Live mode does not save any images, it is just pre-view of the recording.

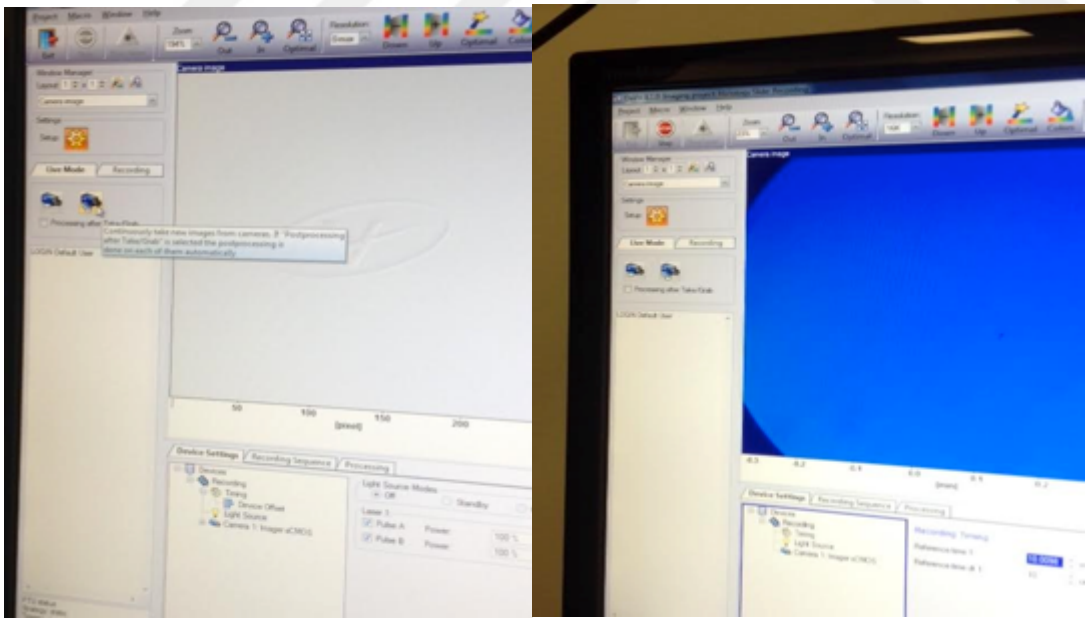

A **B**

Figure A.10. (A) Recording button for sequential live mode (B) Red stop button to stop live mode recording

11) After adjusting your set up for imaging by live mode, click on "Recording" just next to "Live Mode". Then adjust the "number of the images" to record by "Recording sequence" part of the

setup under the camera image (Fig. A.11A). Note that time difference between two adjacent images is about camera imaging speed. Speed of our camera(Lavision sCMOS camera) is 50 fps. Finally click “start recording” to start recording (Fig. A11B) ☺

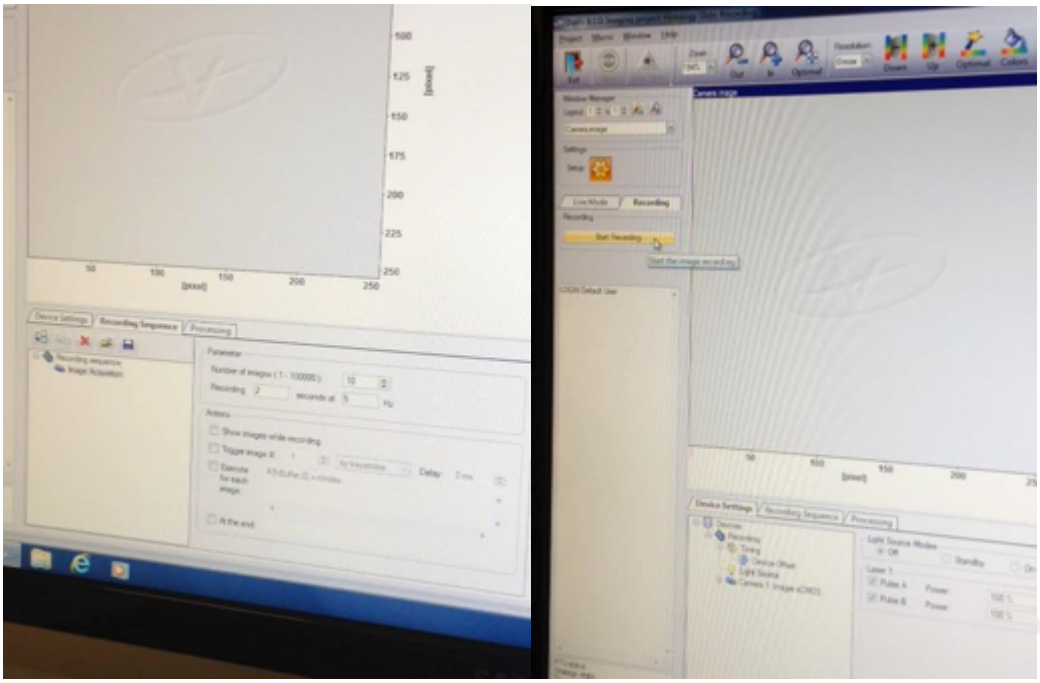

A B

Figure A.11. (A) Setup subwindow for adjusting the number of sequence (B) Recording button

12) Wait for completion of recording(Fig. A.12A). After recording you can find your recording file under the “properties” option of the project. You can change the name of the recording by right mouse button and clicking on “rename”. To export your recording, click right mouse button and choose “Export”(Fig. A.12B). After choosing “export”, export page appears on the left side of the screen. Choose “Movie AVI” or other types depending on your application from “Export Type” section. Also choose the place where the recording will be exported into from “Export Path” (Fig. A.12C).

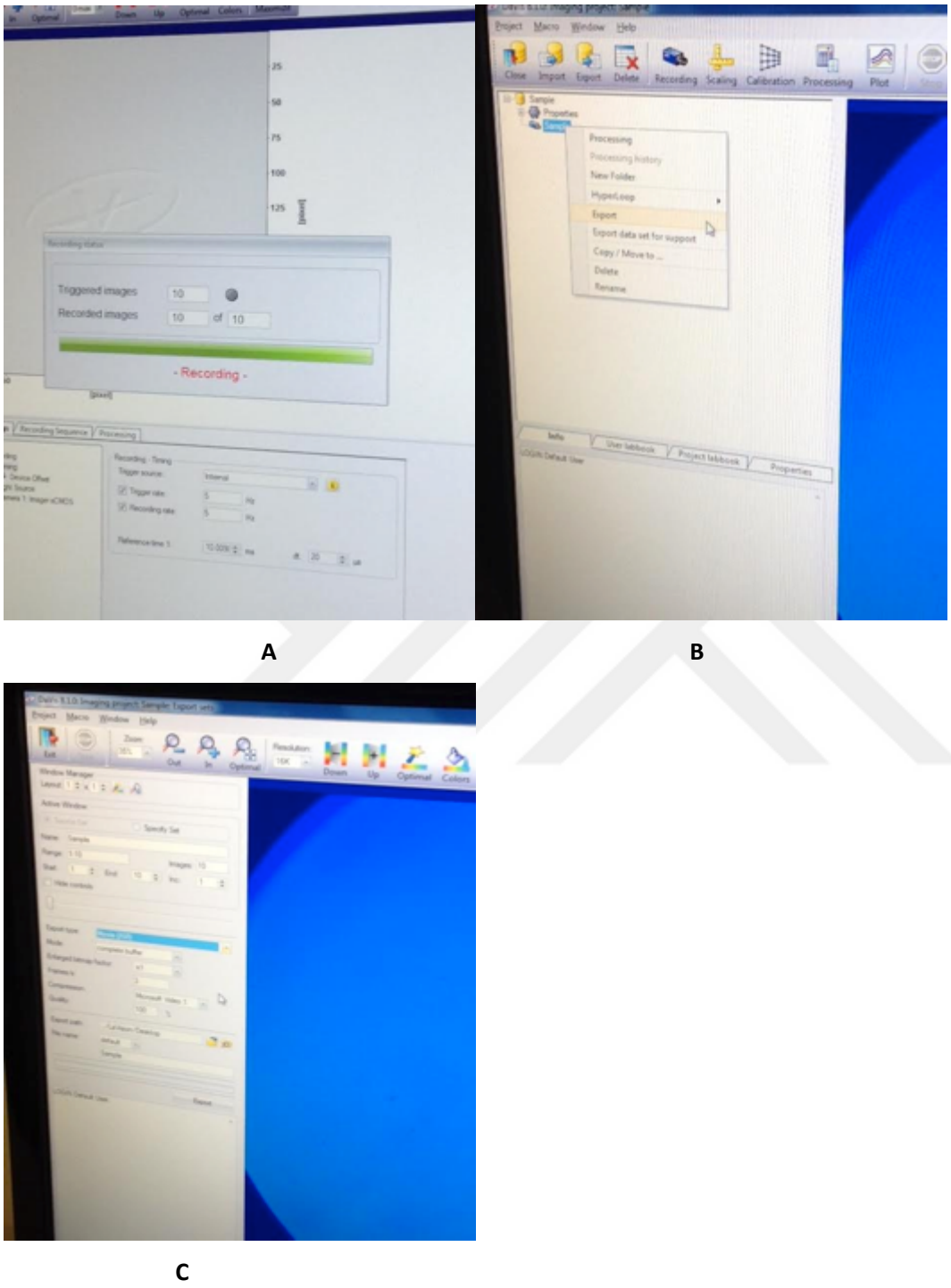

Figure A.12. (A) Recording is performing (B) export button by right click (C) Choosing export path

13) After exporting, click on the "Exit" to move your project where you can see your recordings. If you want to record new images, follow the steps from STEP 9. If you do not, click "Close" to exit your project. When you come to main menu of the Davis, just click on the "cross sign" at the right

upper corner to exit Davis software.

14) When you came to desktop, close the camera as in the STEP 3-figure b. Then remove the dongle as in the STEP 4 and put the dongle into its folder.

15) Then you can shut down the computer and microscope.

- **You should work on the user manual of the microscope before operation with the microscope.**

Protocol E3 - Special Case: Processing of previously recorded mussel flow data

In this special case, processing steps of the recorded flow data of mussels will be presented. Davis software of LaVision is used for processing steps. The problem for these data is that first frame of the images are not useful due to lack of light, so we need extraction of second frame from data and filter operations.

1. Open the PIV computer and plug the PIV dongle as in the Fig. A.13. Then start Davis Low Speed software from desktop.

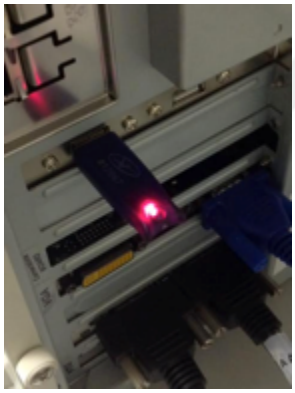

Figure A.13. Plugging dongle

2. Select the project and double click to project. Select the recorded data and click "Processing" from top of the page.

EXTRACTING FRAME AND FILTER OPERATIONS

3. First processing operation is to extract frame 1(or frame 0 can be selected, best frame which gives well focused particle image shift with good illumination should be selected). While selecting frames, change resolution (from top of the page) to see particles for each frames(see Fig. A.14). Click "Start Processing" when the proper frame is selected.

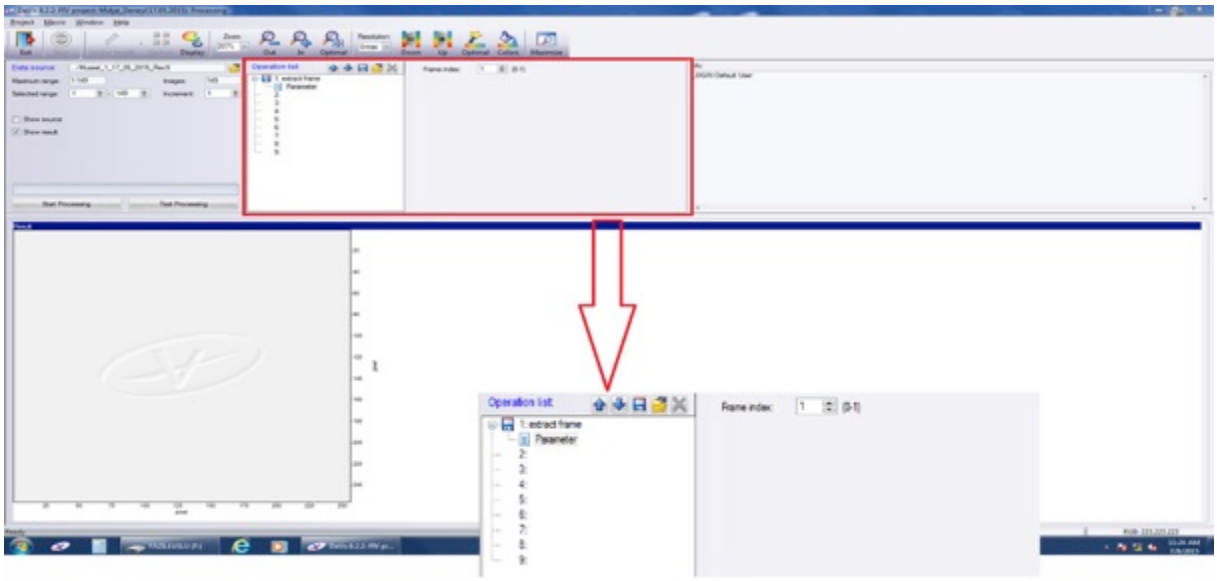

Figure A.14. Extracting frame

4. As second operation, click right on the 2. operation in list and select Subtract Sliding Minimum from non-linear filters . Then select 5 pixel (see Fig. A.15). Finally, click "Test Processing" to see result and click "Start Processing" when you find scale length.

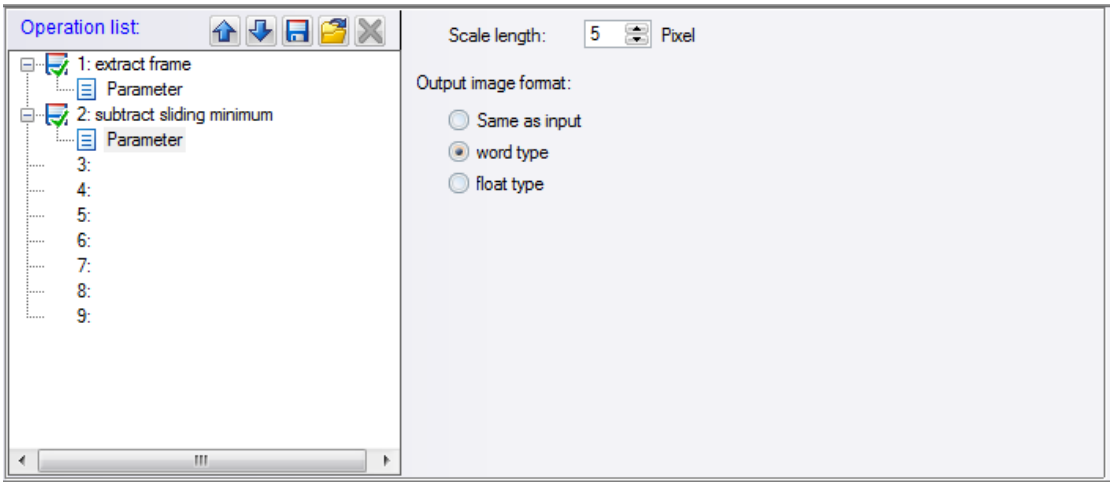

Figure A.15. Applying "subtract sliding minimum"

5. As third operation, click right on the 3. operation in list and select Substract Sliding average(gaussian profile) from Non-linear filters. Then select 30 pixel (see Fig. A.16).

Finally, click “Test Processing” to see result and click “Start Processing” when you find optimal filter length.

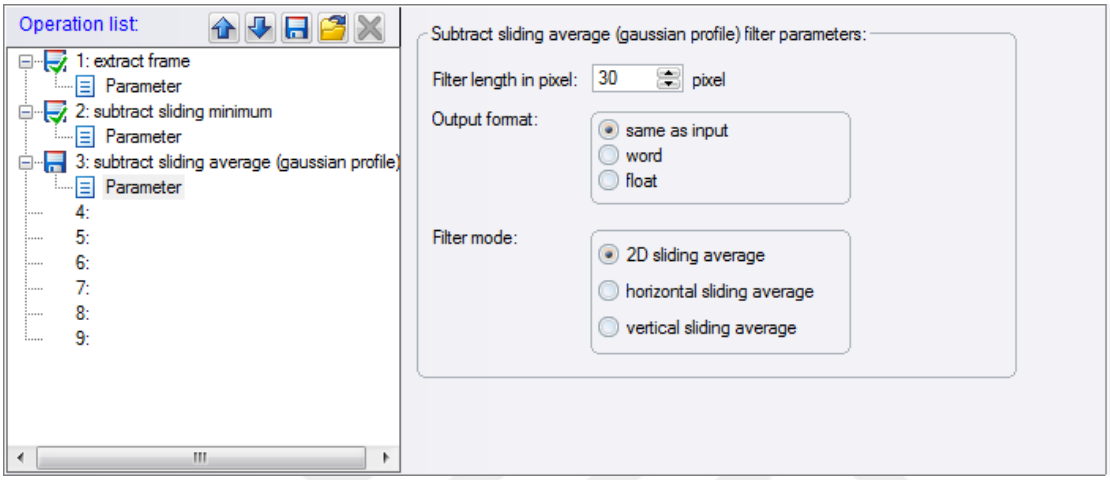

Figure A.16. Applying “Subtract Sliding Average (gaussian profile) filter

PIV PROCESSING STEPS

6. The last operation is selecting PIV operation type to get velocity vectors. *PIV time series of single frames* is selected as PIV operation because one of the double frame is previously (step 3) extracted and we have single frame.

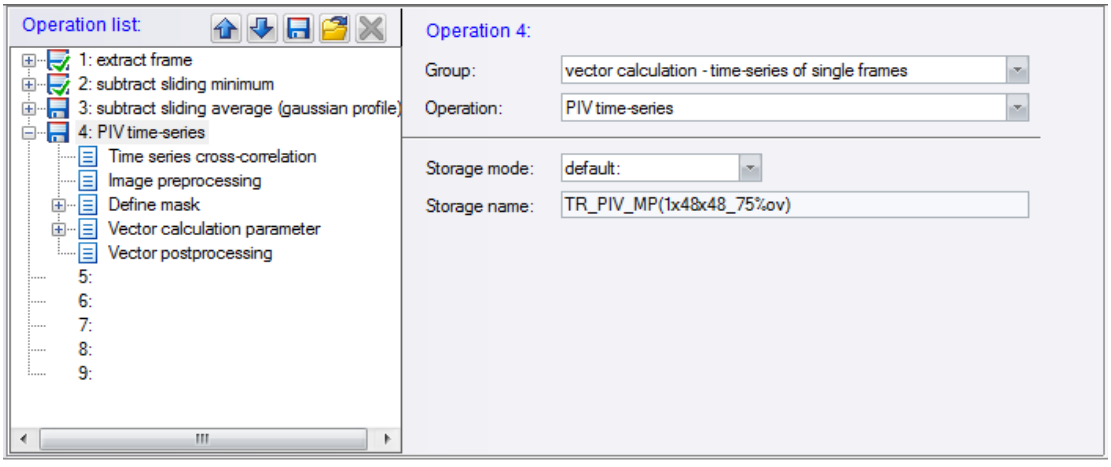

Figure A.17. Selecting PIV method

7. In image preprocessing, substract sliding background is selected as 50 pixel to eliminate background noise (see Fig. A.18). Also substract offset. counts is used with 10 counts and normalization is 15 pixel.

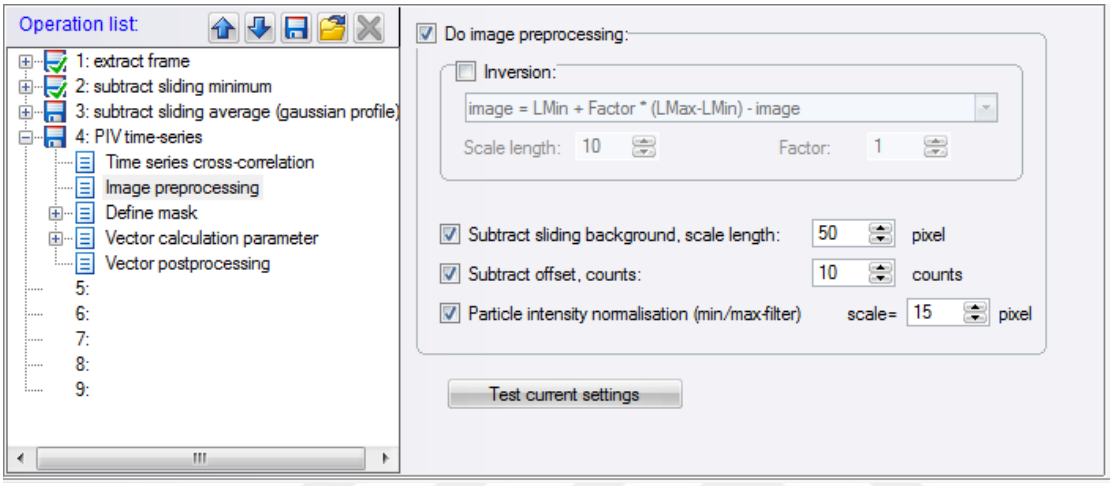

Figure A.18. Selecting Image Preprocessing settings

8. Click "Use mask" then click on "Define geometric mask" as in Fig. A.19. Then Click on "Geometric Mask" and select the region which is the intended area for vector calculation in Fig. A.20.

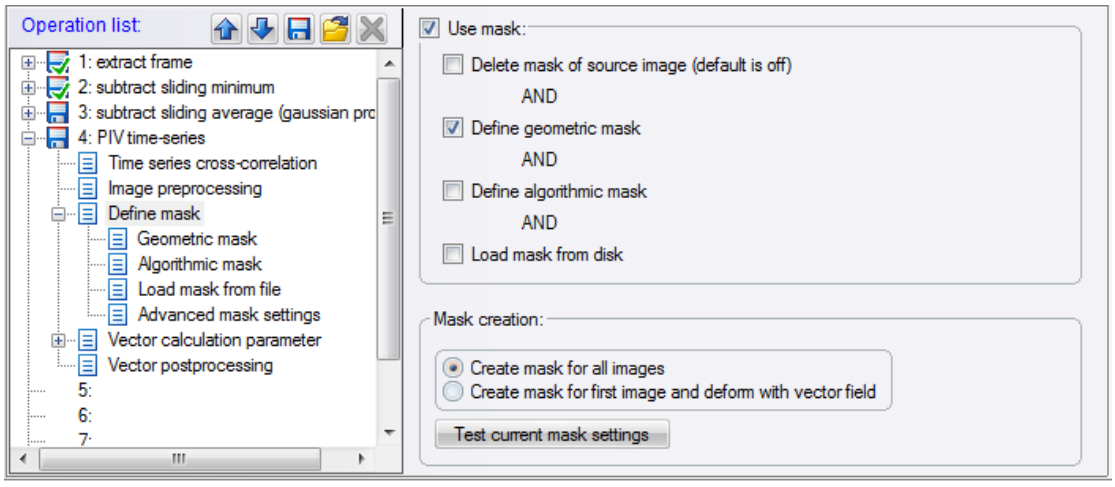

Figure A.19. Activating mask operation

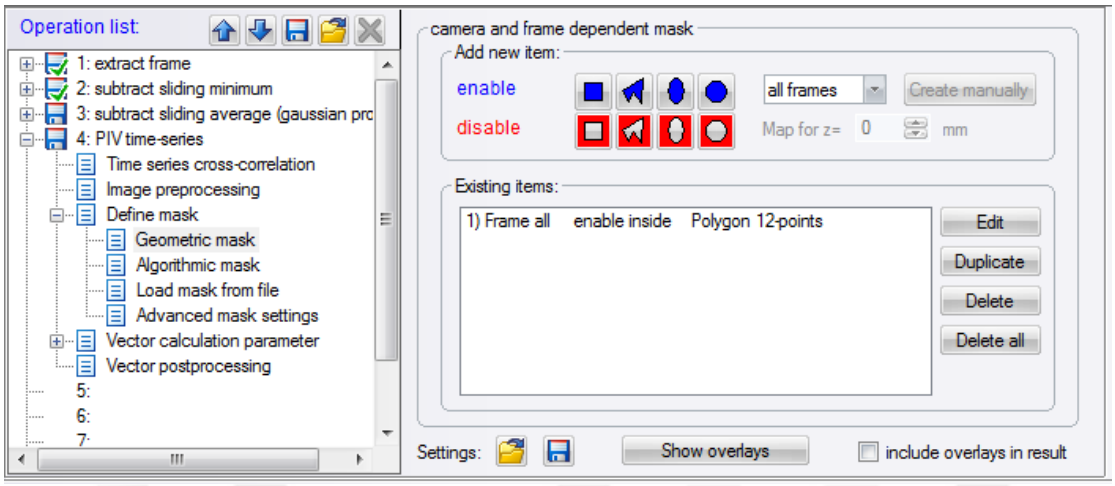

Figure A.20. Selecting Region for vector calculation by masking

9. Then Click on "Vector calculation parameter". First click on "cross-correlation", then click on "Multi-pass (decreasing size)" as iteration. Select window size to 96x96 to 48x48 as interrogation window. Then select 75 for overlap to increase validation of correlation.

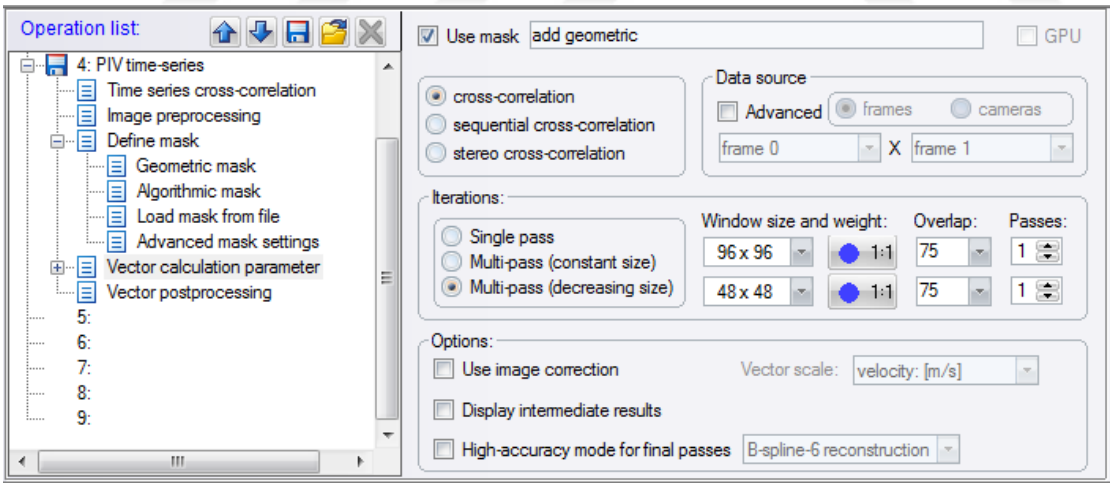

Figure A.21. Selecting calculation parameters

10. First click "Do vector postprocessing". Delete vector if its "peak ratio Q < 1 ", spurious vectors can be eliminated with this option. Select median filter as "universal outlier detection", select "remove if residual > 1" and "(re)insert if residual < 3". Then activate "remove groups with < 50 vectors" and use smoothing as in Fig. A.22.

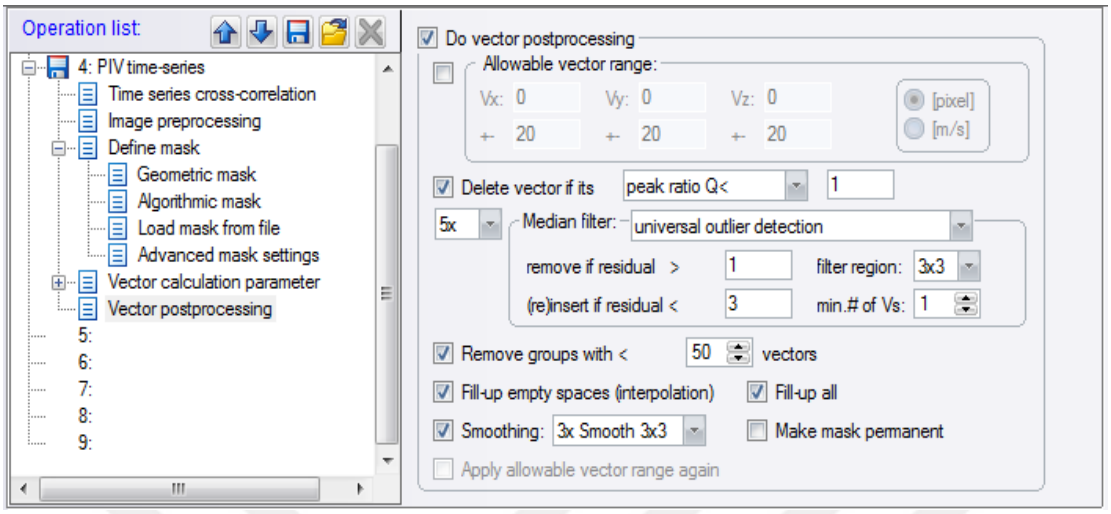

Figure A.22. Postprocessing steps

Then click “Test Processing” to see results fast. Finally, click “Start Processing” to get results for all images. Please note that the parameters at each step might be different even for different recordings so functions of the filters and steps should be known. At the next version of this protocol, all properties of the filters will be presented.

Protocol E4 - PIV Analysis Steps for Recorded Images

In this protocol, PIV analyses of recorded images by different imaging techniques such as confocal microscopes (other than PIV setup and cameras) will be presented step by step from image preparation to PIV post processing.

Image Preparation

Image preparation includes converting images from .lsm (or other file formats) to Tiff image sequences by using FiJi. Note that FiJi is one of the most useful software used for image processing with multiple operations and filters.

1. Open FiJi and import data set with "File => Open => *directory of data set*".
2. Use "File => Save as => Image Sequences…" to export TIFF image sequences (see Fig. A.23). Select Tiff as file format and give appropriate name for the folders. I suggest giving 4 digits if your image stack has thousand of images.

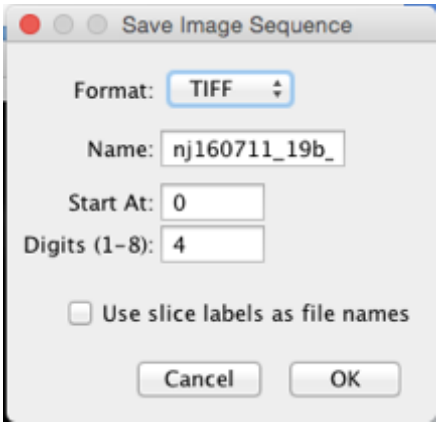

Figure A.23. Exporting Tiff image sequences by ImageJ.

3. Open DaVis software (do not forget to plug in LaVision USB dongle) and create a new project (Fig. A.24A). After clicking "New" button, window to characterize the created project (Fig. A.24B). Specify the project name and select "PIV" as type of project otherwise it is not possible to do PIV processing.

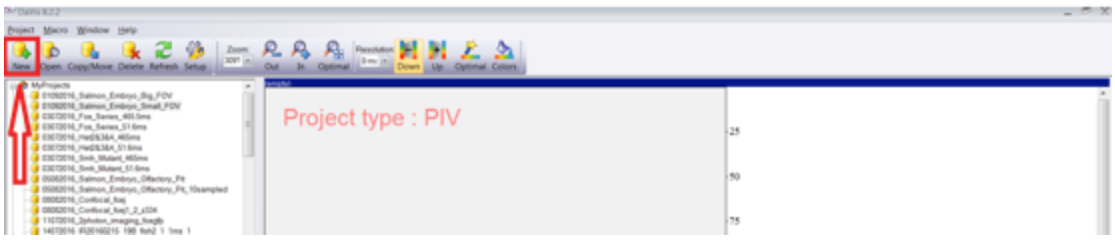

Figure A.24A. Icon for new project

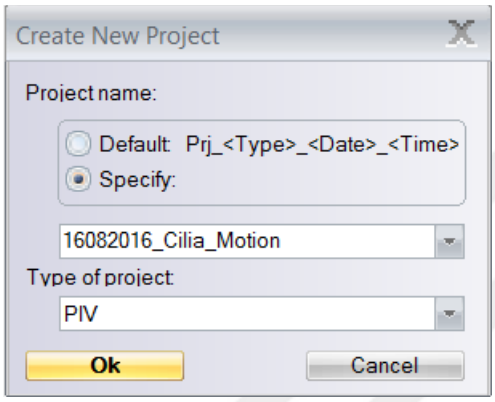

Figure A.24B. New project subwindow

4. Get into project and click “Import” button (Fig. A.25A). Find the directory of folder, which includes Tiff sequences (created in step 2), from “Select Path” sub window at left top (Fig. A.25B). Select all Tiff files from “Import” sub window at next to “Select Path” sub window (Fig. A.25B).

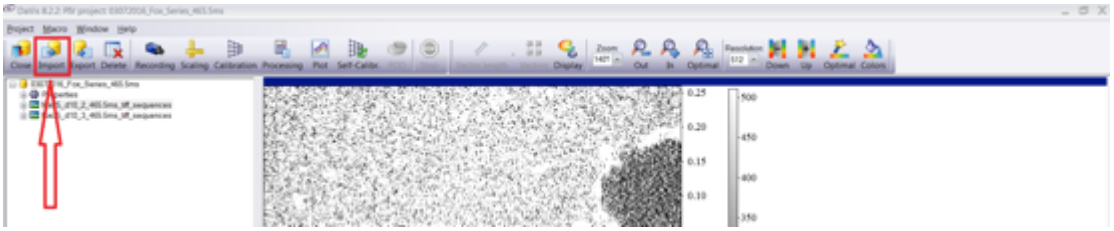

Figure A.25A. Icon for importing data set

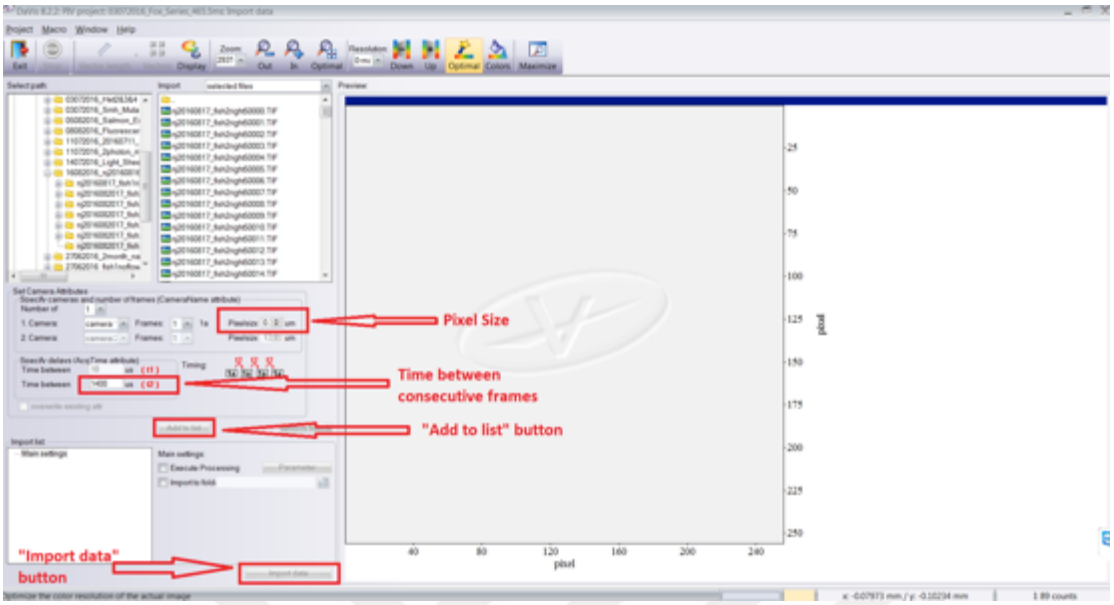

Figure A.25B. Import window where we insert the camera and frame attributes

5. Important to note that we need to know time between consecutive frames (acquisition time) and pixel size of images. We should insert these two values to import window (see Fig. A.25B). Then click "Add to list" and "Import Data" (Fig. A.25B).

PIV Scaling (Calibration)

6. Now data (images) are ready for PIV calibration. First step is calibration of images by using "Scaling" function (Fig. A.26). "Scaling" is appropriate for calibration of two-dimensional data. Click on the data and then click "Scaling".

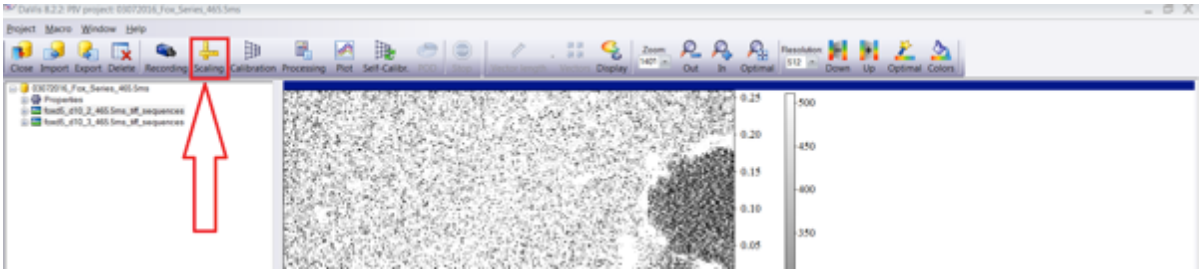

Figure A.26. Icon for scaling

7. When we get into the scaling menu, click on the import button represented by folder sign (Fig. A.27A). Window will appear to select source image for calibration. Find the imported

tiff images. They will appear in ".im7", which image format of LaVision DaVis. Select just any one of them and click "Open" (Fig. A.27B).

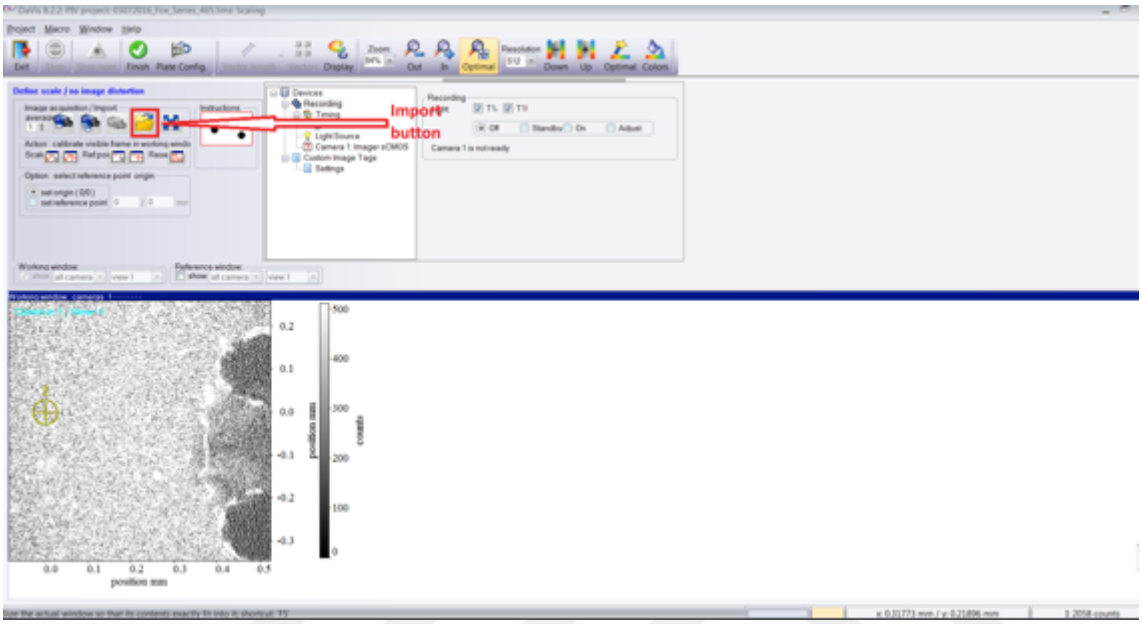

Figure A.27A. Import icon to import data sets for scaling (calibration)

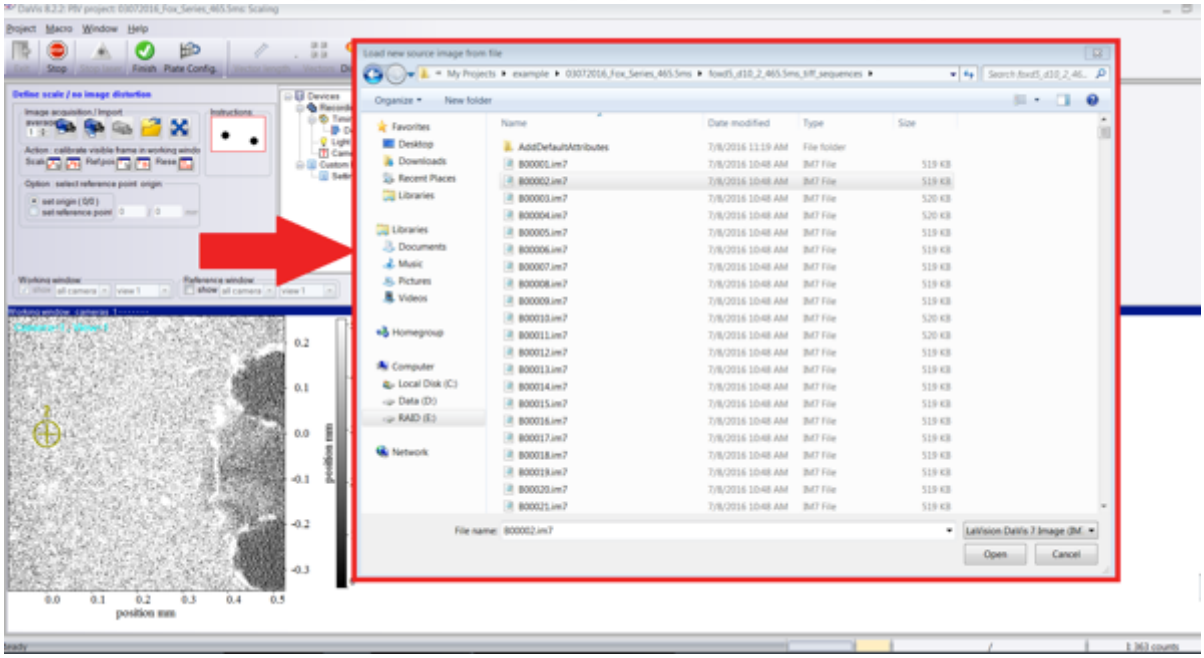

Figure A.27B. im7 format data images for scaling

8. A new window will appear that is asking "Which frames do we want to import?" (Fig. A.28). After checking all the settings are same as in the Fig. A.28, click "OK".

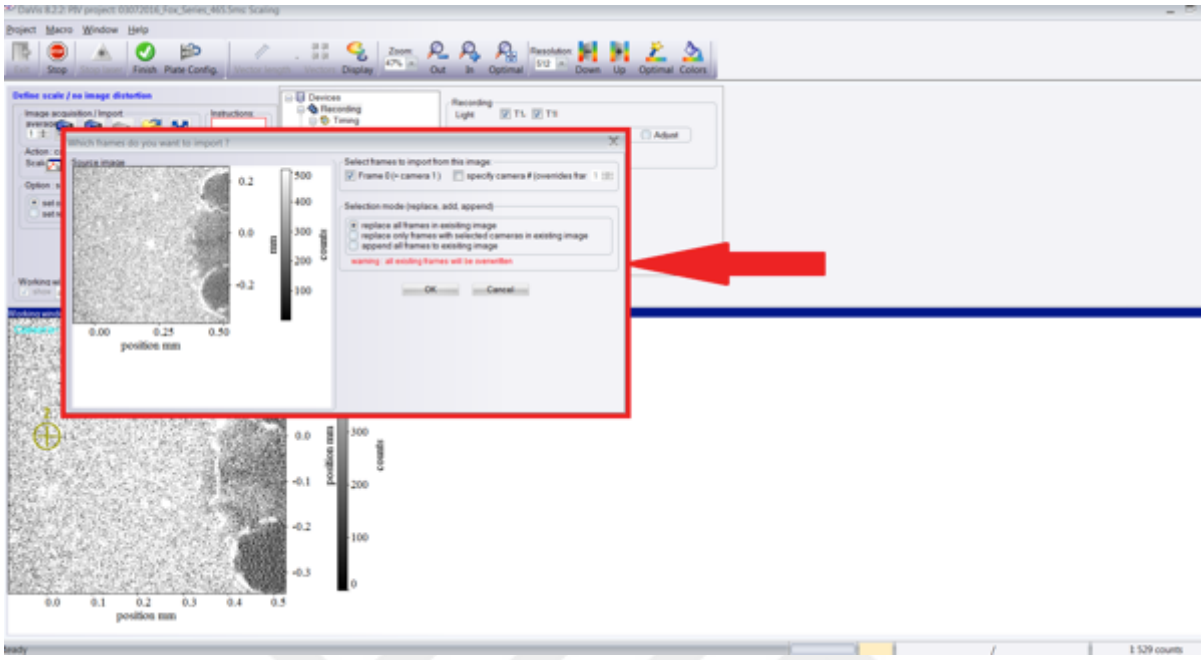

Figure A.28. Importing window for scaling

9. Selected image will be loaded to working window at left bottom. To scale the images, click the scale button shown in Fig. A.29A with red arrow. Your cursor will turn to plus shape. Select two arbitrary pixels and insert the distance between the pixels (Fig. A.29B). Click "OK". To start scaling, click "Finish" (Fig. A.29C). Progress of scaling can be seen at the left bottom of window. After scaling is finished, exit from the scaling window.

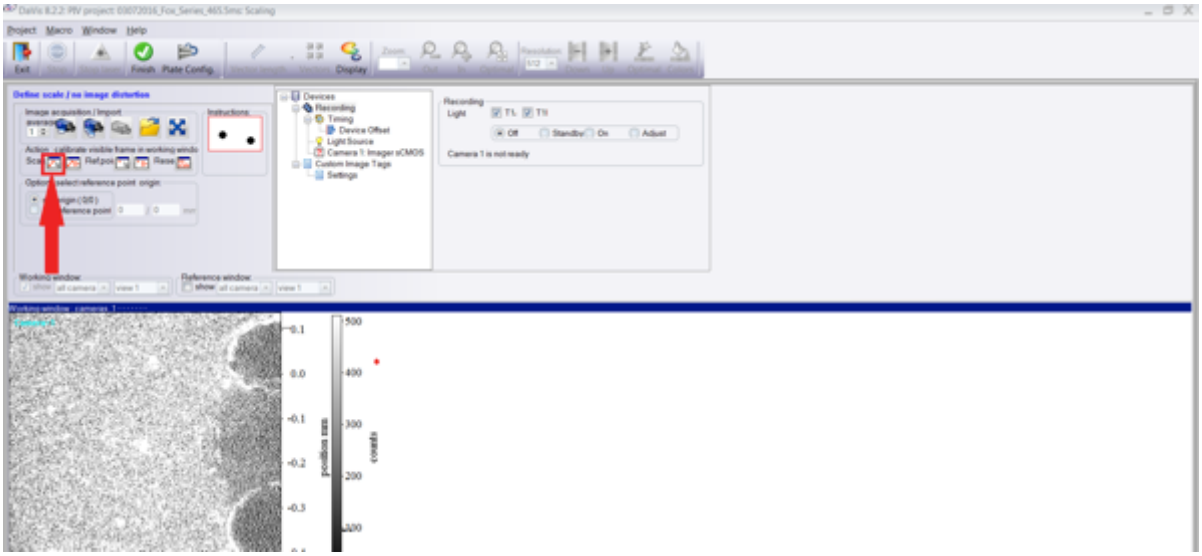

Figure A.29A. Icon for marking pixels for scaling

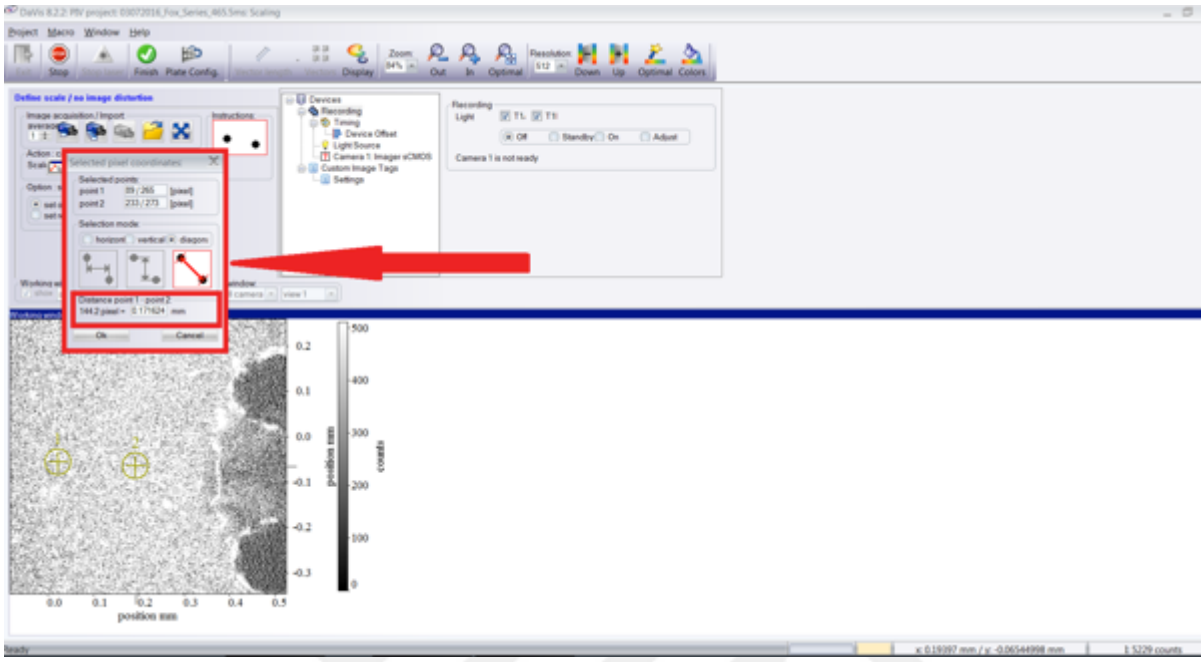

Figure A.29B. Pixel scaling window where we determine the distance

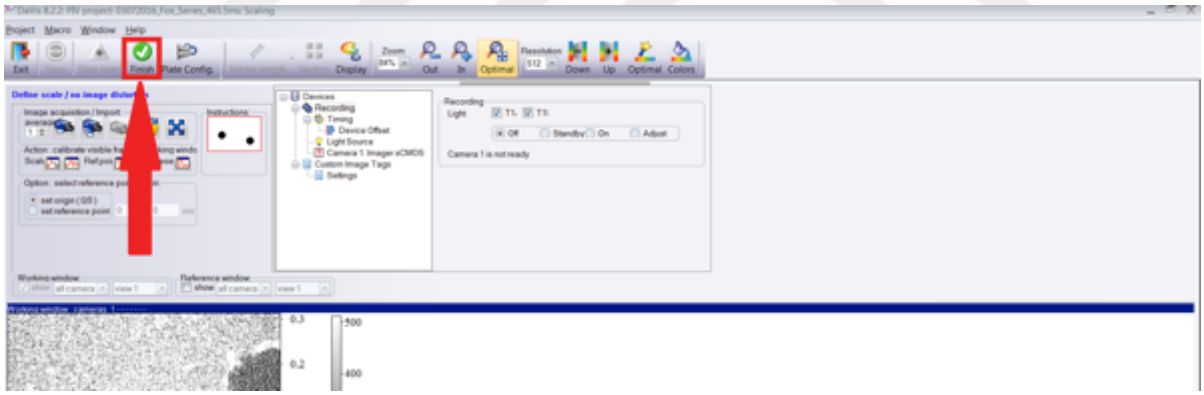

Figure A.29C. Finish icon to start scaling

PIV Processing

10. From now on, we will go through the PIV processing operations where pre-processing, vector calculation, and post processing operations are implemented. Click on the data and then click “Processing” (Fig. A.30).

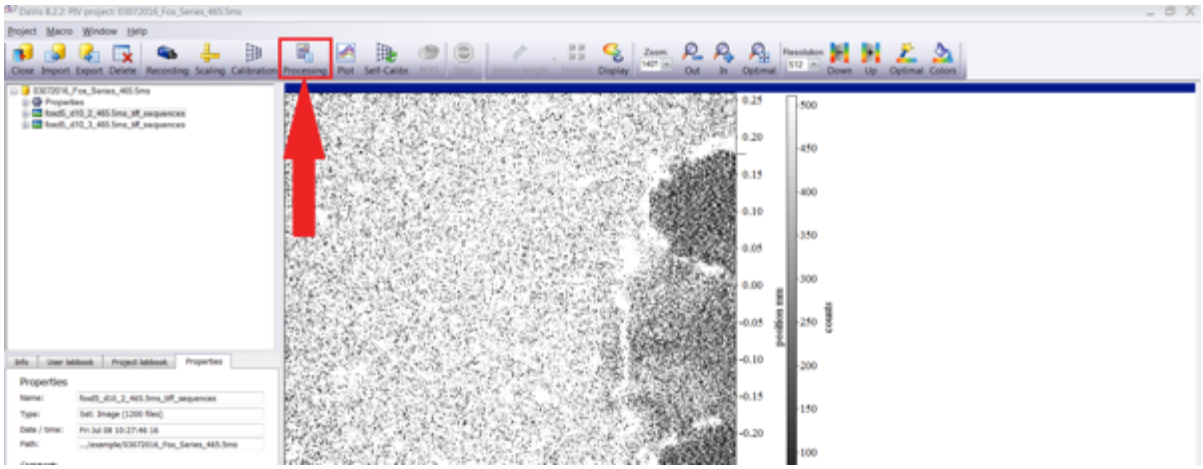

Figure A.30. Processing icon to open processing window

11. In Processing window, data range and increment within the range can be determined for any processing operation by the boxes at left top. Most important part of processing window is “Operation list” shown in Fig. A.31. We can apply different operation by this list. Order of operations can be changed by the “⇑” and “⇓” icons. Operation list can be saved to a specific folder by the disk icon. Also we can load an existing operation list by folder icon. Finally, whole operation list can be deleted by the cross icon.

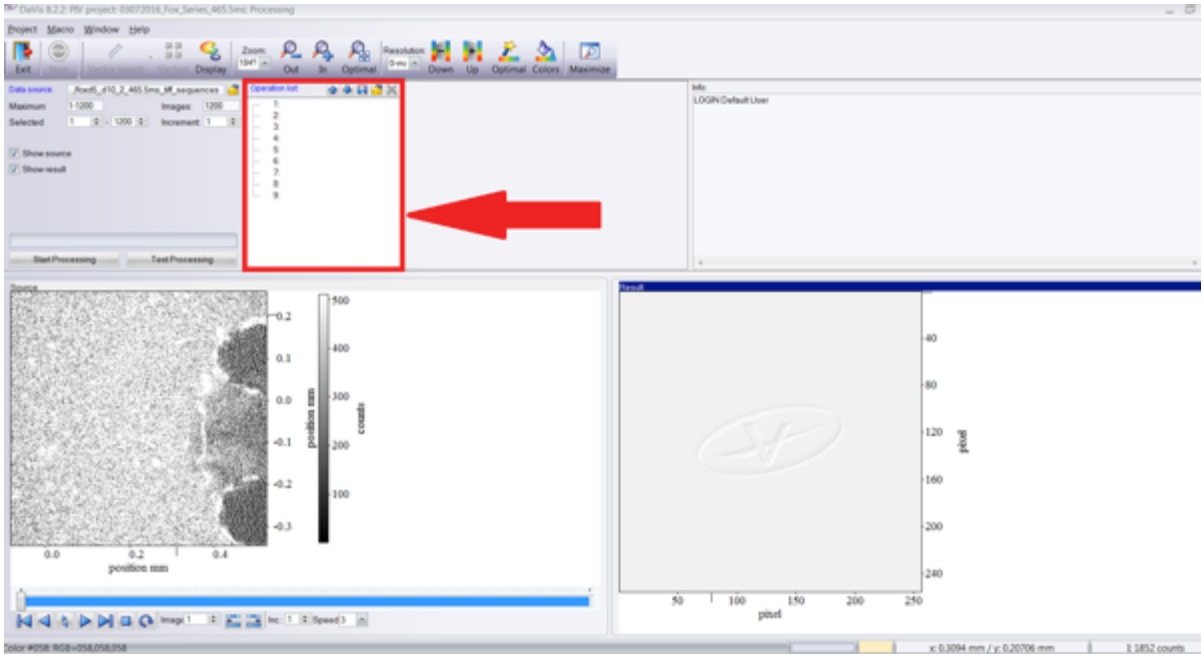

Figure A.31. Operation list

12. First operation is “add default attributes” under the group of “attributes” (Fig. A.32A). Click on the “Parameter” under “add default attributes”, and insert the pixel size and time difference between frames (Fig. A.32B).

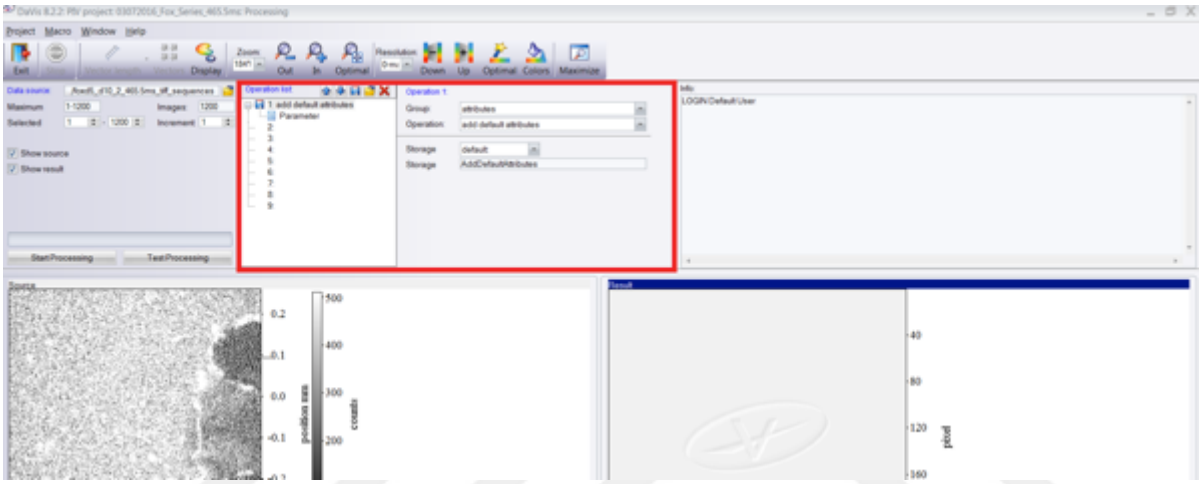

Figure A.32A. Add default attributes subwindow

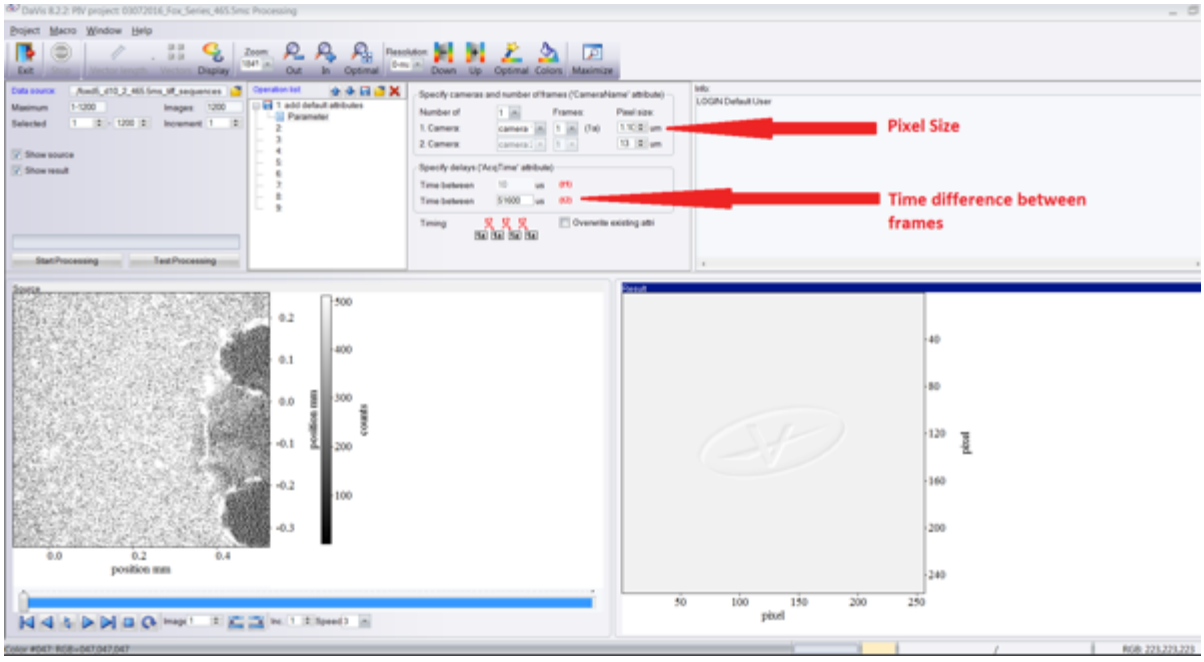

Figure A.32B. Camera and frame attributes

13. Second and the most important operation is PIV processing operation, which is “PIV time-series” (Fig. A.33A). This operation is used for single frame recordings. “PIV time-series” operation includes preprocessing, mask operation, vector calculation, and postprocessing.

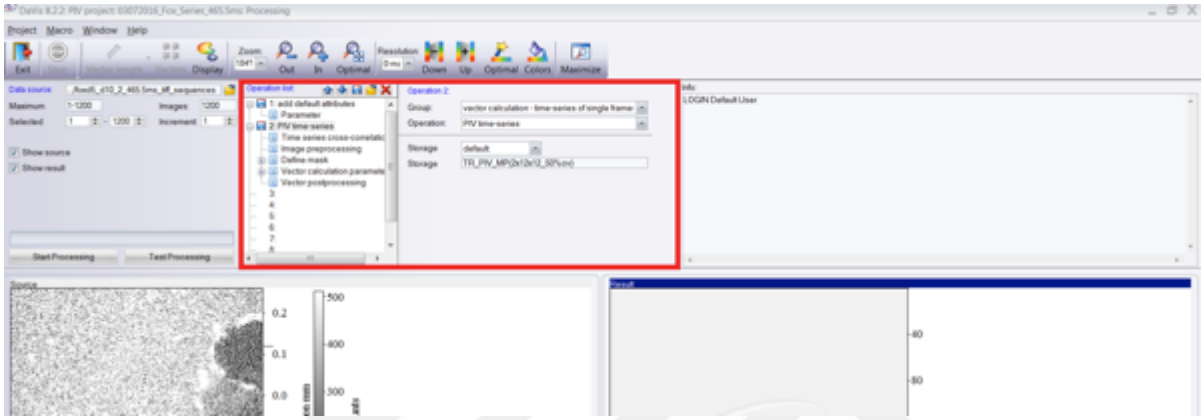

Figure A.33A. PIV time-series

Purpose of PIV preprocessing is to get better and clear particle images (real signal for PIV cross-correlation). Click “Do image preprocessing” at the top of preprocessing subwindow, if it was not done. Then start with defining preprocessing parameters. Preprocessing includes three filters to improve the quality of raw images such as eliminating different kinds of defects from the images by using filters (Fig. A.33B). Click on the little boxes at the left of filters to activate them and define filter dimensions by the boxes at the right of the filters. To test filter configuration, click on “Test current settings” at the bottom of preprocessing subwindow (Fig. A.33B).

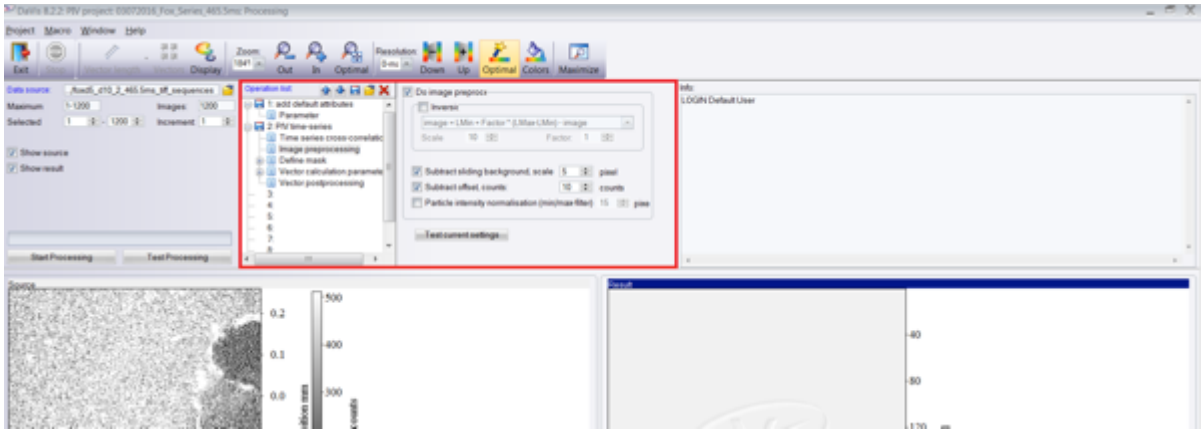

Figure A.33B. PIV preprocessing subwindow

Other than the filters in preprocessing, we can apply several filters such as linear, non-linear and time series filters as separate operation before PIV processing. I strongly suggest reading DaVis software manuals to get into details about filters because different filters can enhance different defects.

14. Now, it is time to apply masking on the raw images. It is used to exclude the regions that are irrelevant for flow such as pipe wall for pipe flow. Under "PIV time-series" operation, click on "define mask". We will see 3 different types of mask (Fig. A.34A).

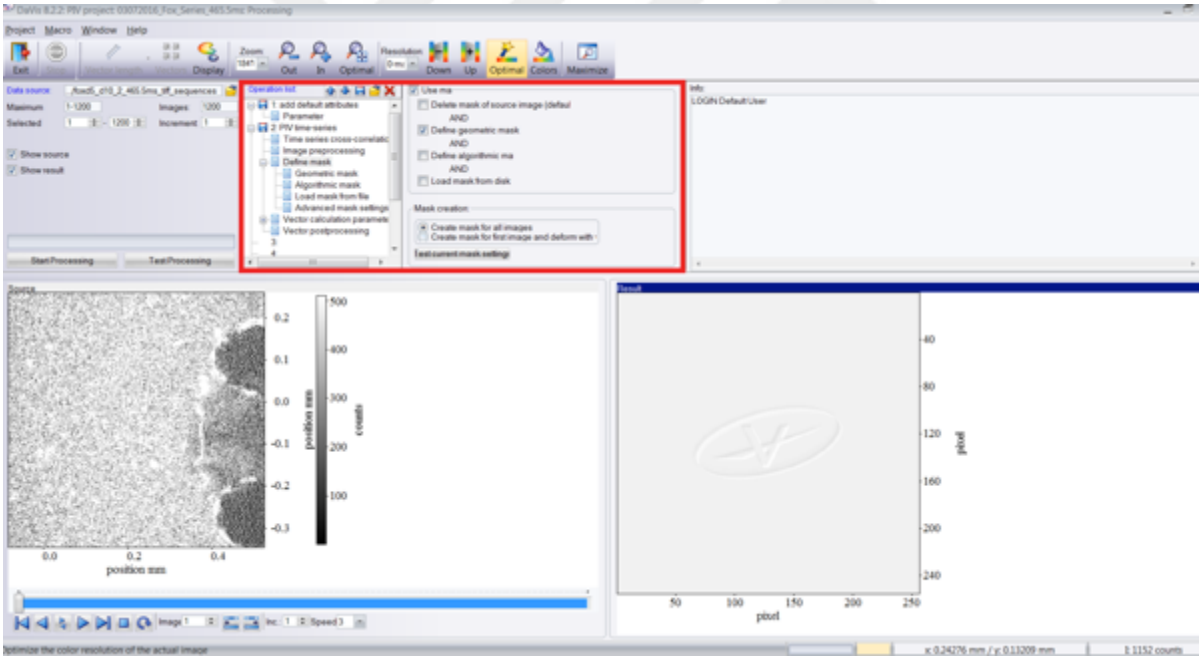

Figure A.34A. Mask subwindow

- Geometric mask is used by manually drawing mask on the images. Most frequently used mask is Geometric mask. To create mask, first click on "Define geometric mask" (Fig. A.34A). Then click on "Geometric mask" in operation list. We can draw masks in different shapes (Fig. A.34B).

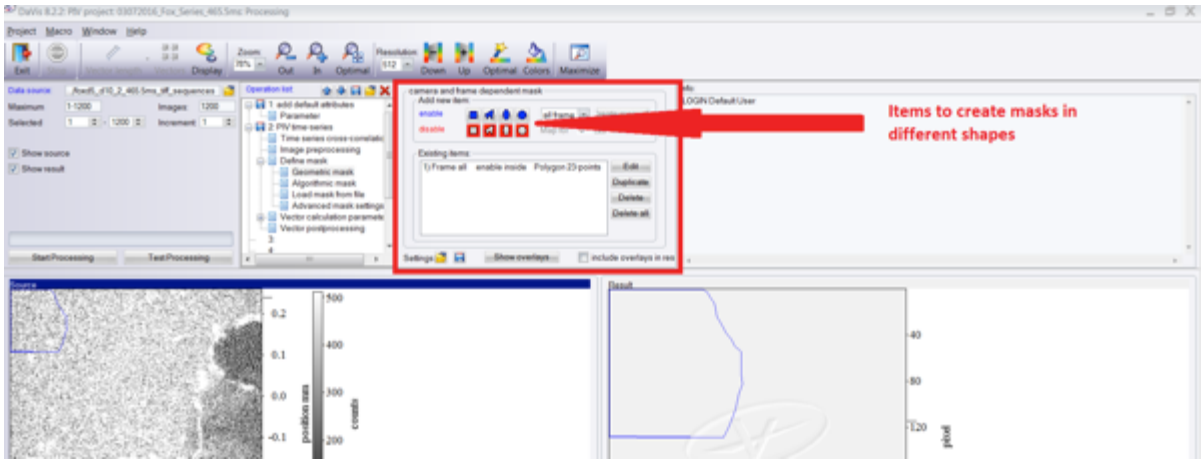

Figure A.34B. Creating mask with different geometries

- Algorithmic mask is another mask and it is very useful in some cases. We can create masks by mostly using intensity operations such as pixel conversion or elimination of some pixels (Fig. A.34C).

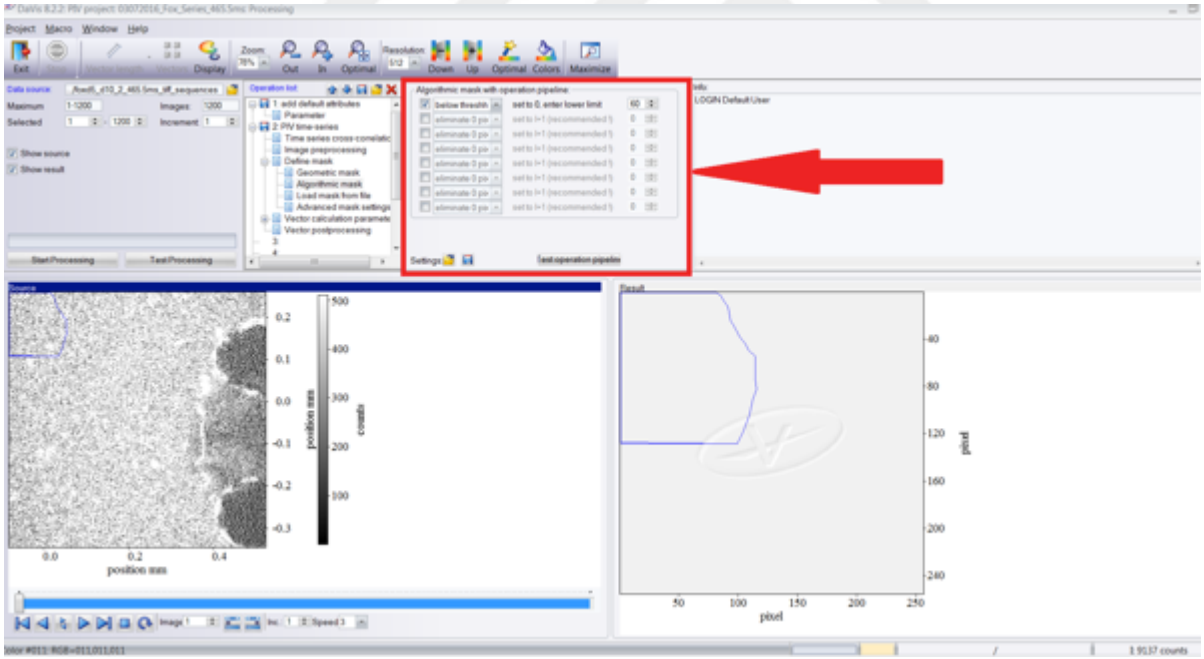

Figure A.34C. Algorithmic mask

- Loading mask is another option. We can import masks from outside of DaVis software. This option might be required because we may need to use different masks for consecutive images. I strongly suggest reading protocol named as "Creating mask by using existing image sets for PIV analyses with application

example". We can create your own masks by using this protocol and load it to your processing (Fig. A.34D).

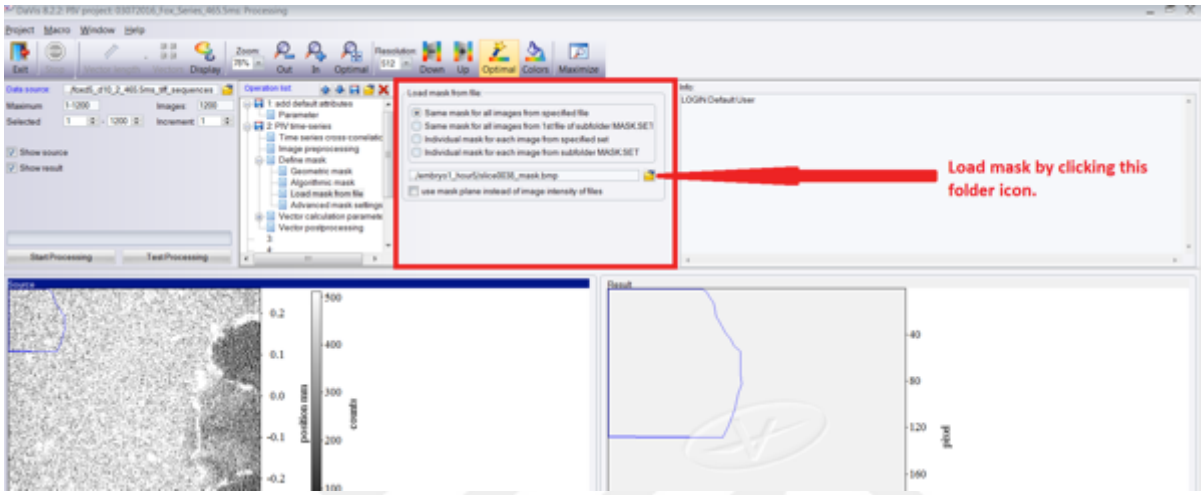

Figure A.34D. Loading mask subwindow

15. After completing mask, we need to adjust "vector calculation parameter" (Fig. A.35). It is very important step because we determine the size of interrogation window, which also corresponds to resolution of PIV analyses. Please note that maximum particle displacement should be ¼ of interrogation window size. If maximum particle displacement is 12 pixels, interrogation window should be 48x48 pixels. Also I suggest using "Multi-pass (decreasing size)". This method may increase computation time but will increase quality of results.

    In Fig. A.35, vector calculation subwindow is shown with red rectangle. Green rectangle indicates the place in which interrogation size and weighting function is determined. Weighting function should be chosen corresponding to direction of flow. "Auto" weighting function is suitable for most of the flows but the most time consuming function. I suggest using square weighting function for first trials. For other parameters in the subwindow, I do suggest reading LaVision Product Manual of DaVis software and other protocols for more details. Manuals can be found at "Help" menu at the top of DaVis

interface.

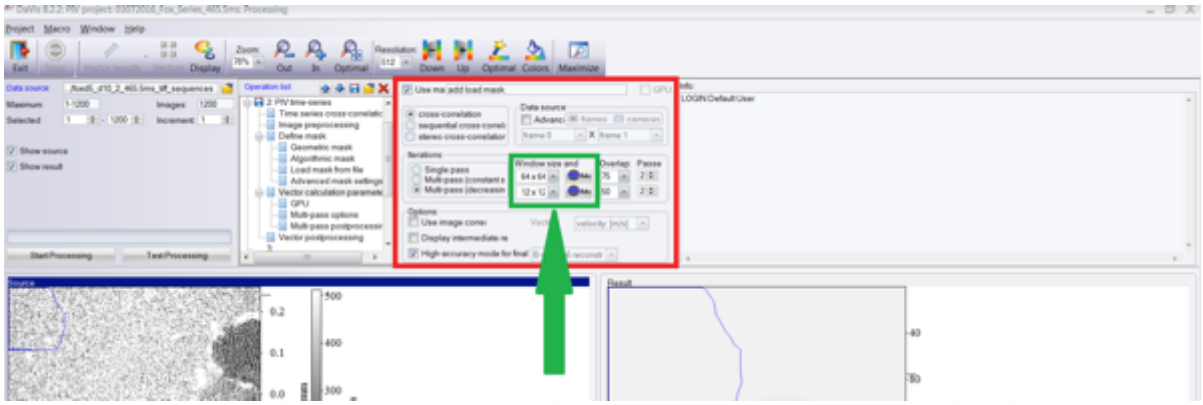

Figure A.35. Vector calculation subwindow

16. Last operation is “Vector Postprocessing”. “Vector postprocessing” contains different tools and filters to improve results (Fig. A.36). “Allowable vector range” enables us to select a range of velocity vectors to include in resuts. “Delete vector” is used for eliminating vectors depending on correlation value of vectors or peak ratio in interrogation windows. “Median filter” has 3 different applications of median filter to eliminate irrelevant vector (For details, please read LaVision Software manual and online sources to understand how median filter works). “Remove groups with” removes group of wrong vectors. “Fill-up empty spaces” is used for filling empty subwindows (due to elimination during filter operation or vector calculation) by interpolation. “Smoothing” is used to smooth the vectors by evaluating neighbor vectors.

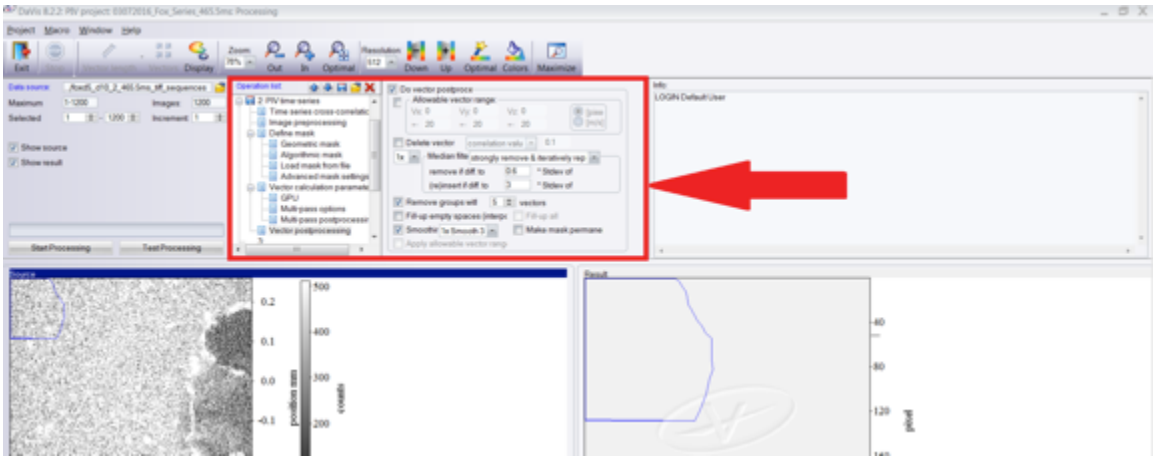

Figure A.36. Vector postprocessing

17. Now we are ready to start processing but we need to optimize our all operation to get the best vectors. Click on “Test Processing” to test results. Computation time of “Test Processing” is less than actual processing, so optimize your operation list by changing filter parameters or vector calculation parameters. “Test Processing” can be performed again and again until obtaining best parameters and filters for the best performance. When you get obtain the best parameters, click on “Start Processing” (Fig. A.37). Processing may finish in minutes or hours depending on PIV processing method, filters, and parameters.

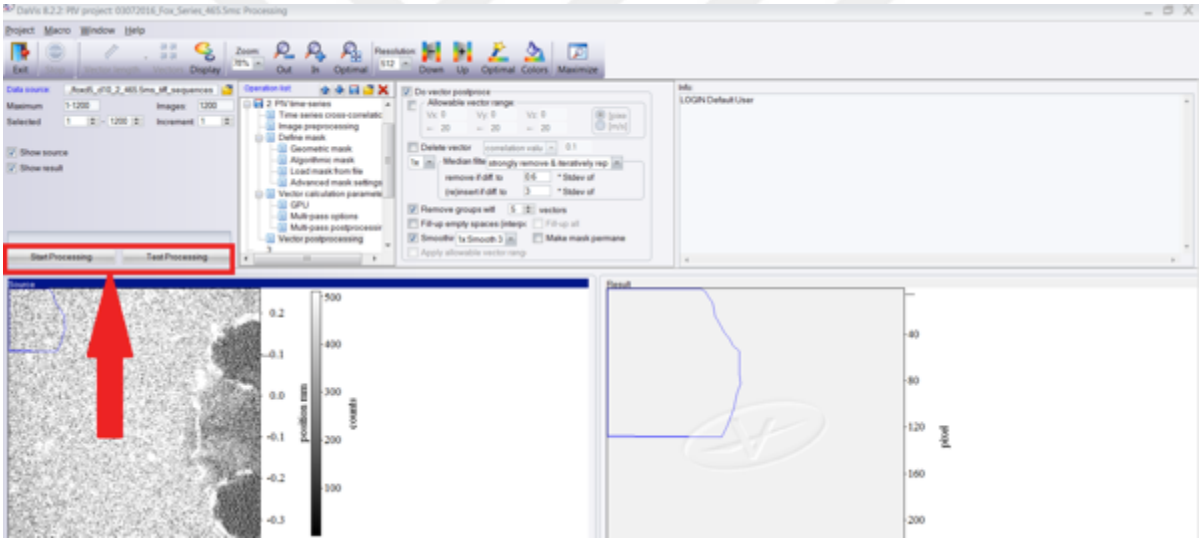

Figure A.37. Starting processing

18. Processing steps are finished but what if we have tens of data sets and we want to process them together. “Batch processing” is one of the best options to tackle this challenge. By using batch processing option, we can process up to 10 data sets together even if they have different sizes and processing lists. First, I suggest importing data sets first and scaling (calibration) them together (steps from 1 to 9). After scaling, what we need to do is to establish the processing list (steps from 10 to 16) for each data set and saving them in a folder by using disk icon (at the top of operation list). Then:

• Right click on any data set and click on Batch Processing. Then Batch Processing window appears (Fig. A.38). Import the data set folders and operation lists as it can be seen at Fig. A.38. After these steps are performed, click on “Check consistency” and then click “Start Processing”. You would prefer to start the processing at night ☺

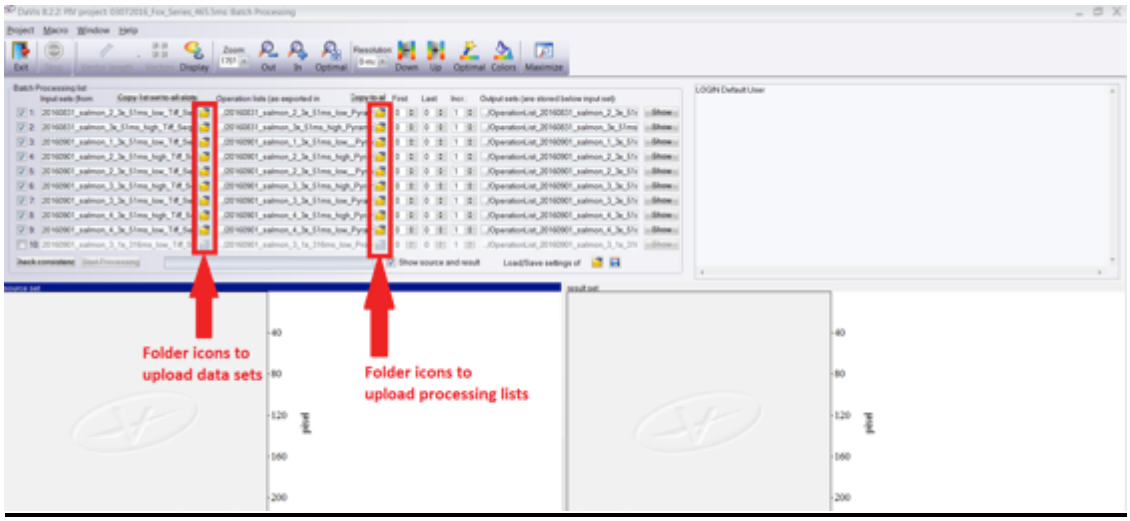

Figure A.38. Batch processing window

Have a good PIV processings ☺ and do not forget to improve this protocol

Appendix B. Projet 3D printer protocol

1) Firstly, you should create your geometry and export it as .STL format from any CAD program. Before operation of printing, please check the followings that;
    - Usb cable is connected to computer.
    - Power supply is connected.
    - Build platform is present and locked (see Fig. B.1A and Fig. B.1B).
    - Visijet FTX green print cartridge is present and locked (see Fig. B.1A and Fig. B.1B).

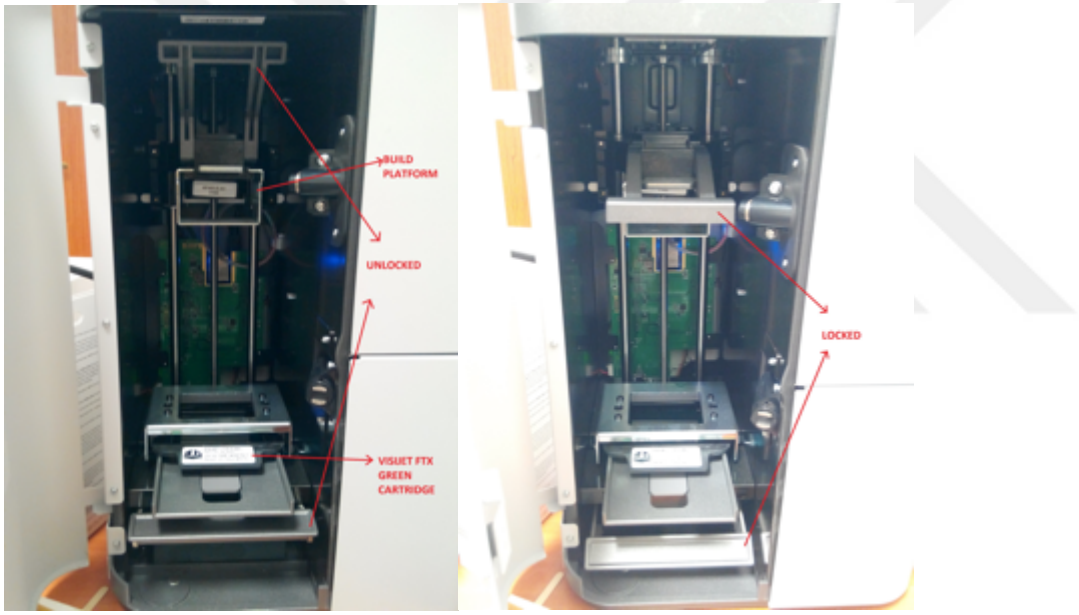

A **B**

Figure B.1. (A) Build platform and Visijet FTX green cartridge are unlocked. (B) Build platform and Visijet FTX green cartridge are locked.

2) Open the *Geomagic Print for ProJet 1200* sofware.
    - Check that the printer is connected to computer and software by clicking "Printer" button.
    - Import the part (which is in .STL format) by clicking "Import" button (see Fig. B.2).
    - Suggested to use "Auto Arrange" button to optimize the printing time and material use (see Fig. B.3).

- To create supports, use “Auto Support” button (see Fig. B.3). Also you can add supports by clicking “Manual Support”, if necessary.

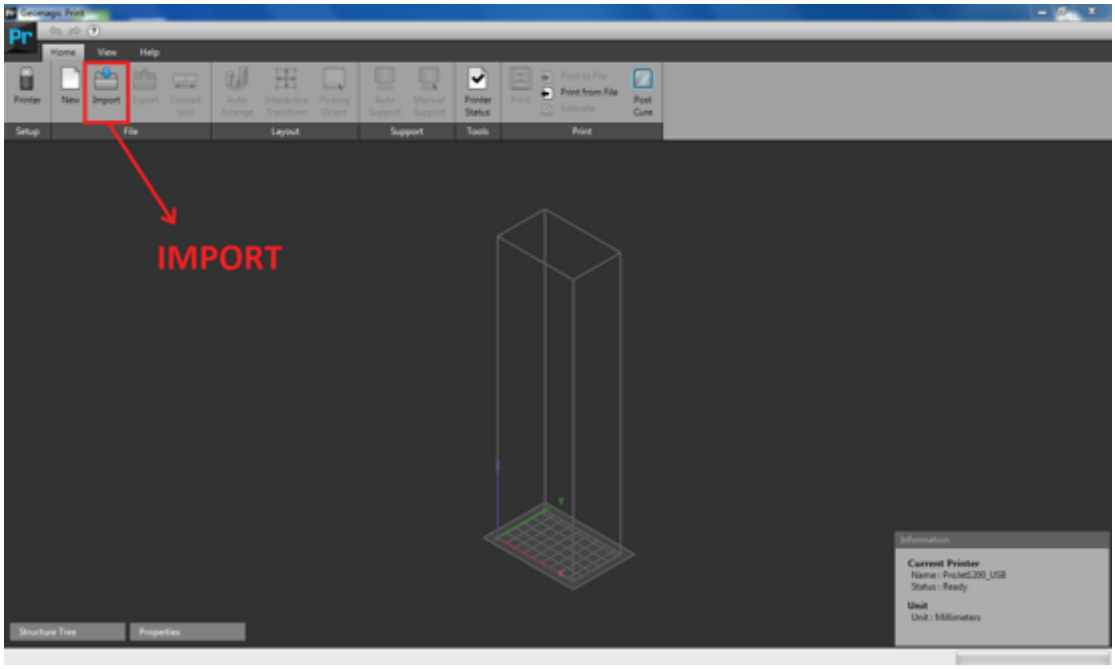

Figure B.2. Importing .STL parts to *Geomagic Print for ProJet 1200* sofware

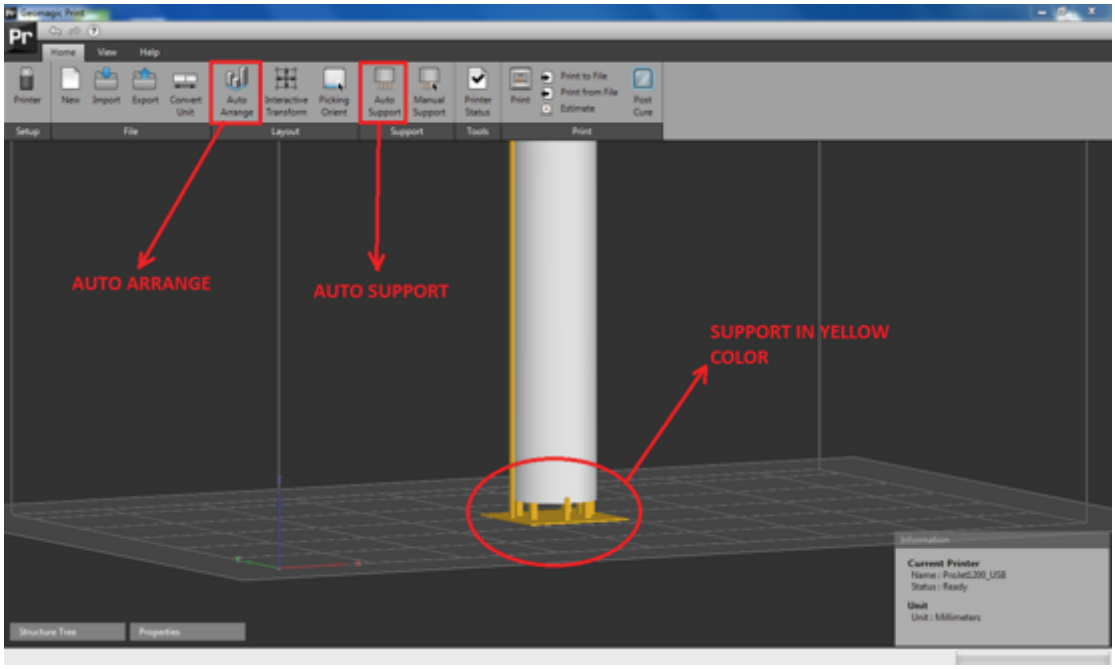

Figure B.3. Auto Arrange tool to arrange the part for optimization of material and time, Auto Support tool to create supports automatically.

3) After all the previous steps are performed, click “Print” button (see Fig. B.4). Software will generate build file and send the geometry of the part to printer (see Fig. B.5). You can track the printing procedure from “Printer Status” (see Fig. B.6).

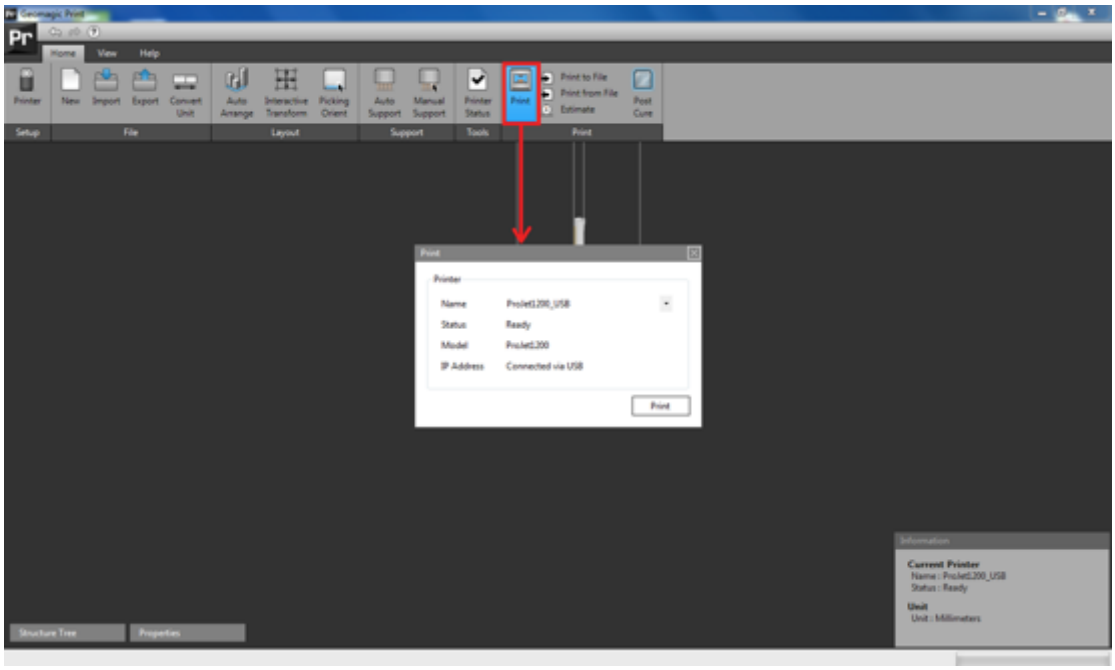

Figure B.4. Print button to start printing

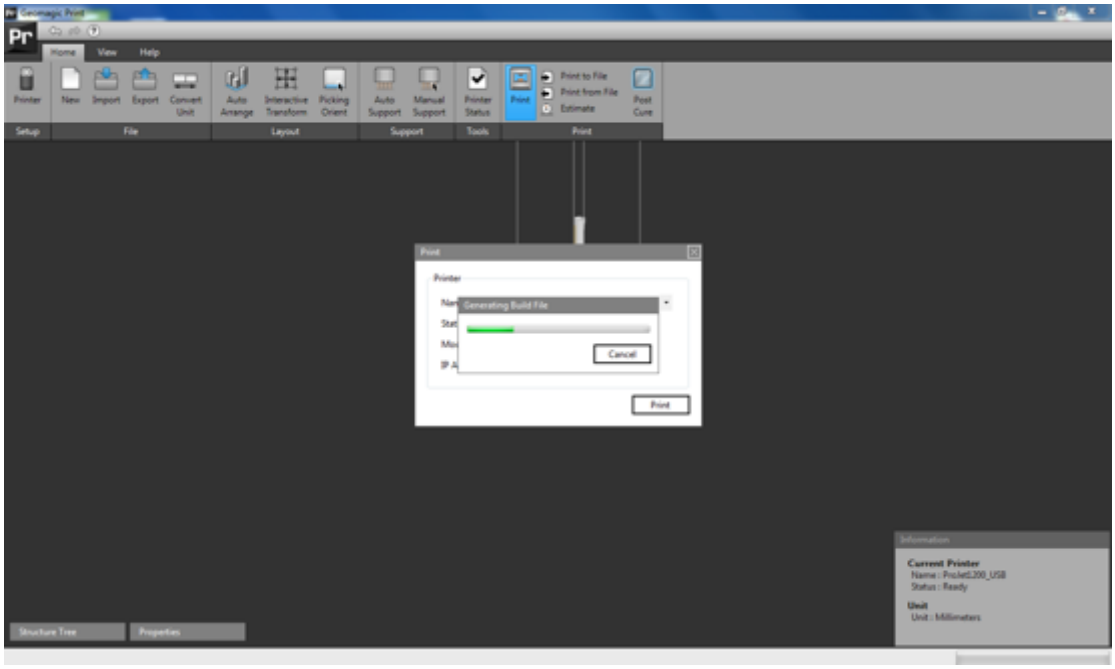

Figure B.5. Software is generating build file for printing

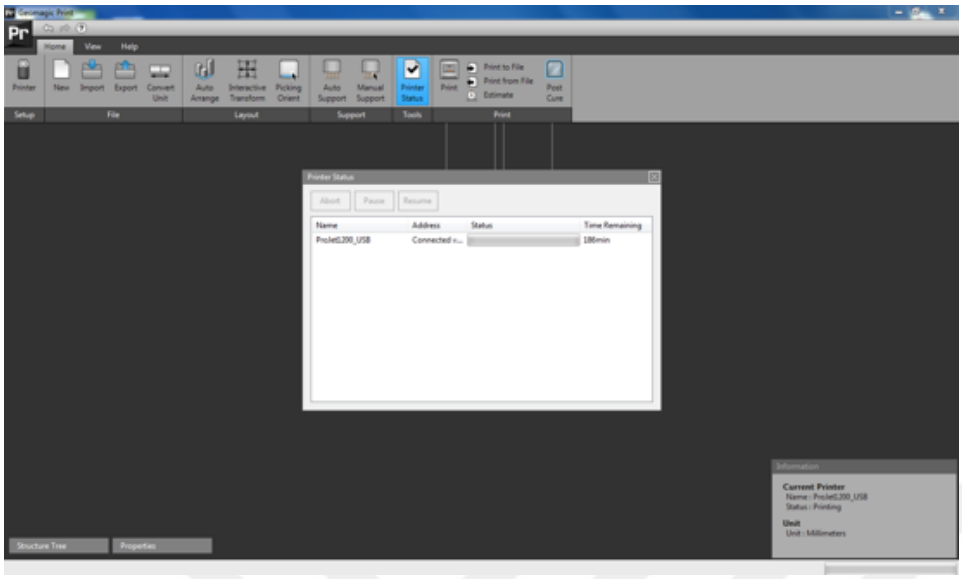

Figure B.6. Printer Status window

4) When the printing is finished, hold the build platform without touching your hand.

- Continuously dip and remove the part into container which contains IPA (Isopropyl Alcohol) for 60 seconds (see Fig. B.7A). Then spray air to remove the alcohol from the part (see Fig. B.7B).
- Repeat the same step for 90 seconds.

Note: Always wear the protective gloves during cleaning parts and post process.

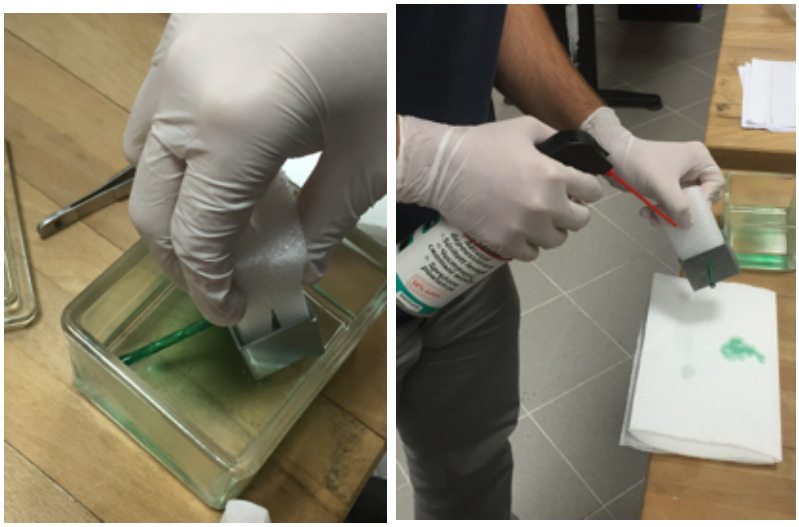

A **B**

Figure B.7. (A) Cleaning part from resin (B) Air spray to remove alcohol with IPA

5) Put the part into the Post Curing chamber (see Fig. B.8) and start Post Curing (see Fig. B.9).

Figure B.8. Putting the part in post curing chamber

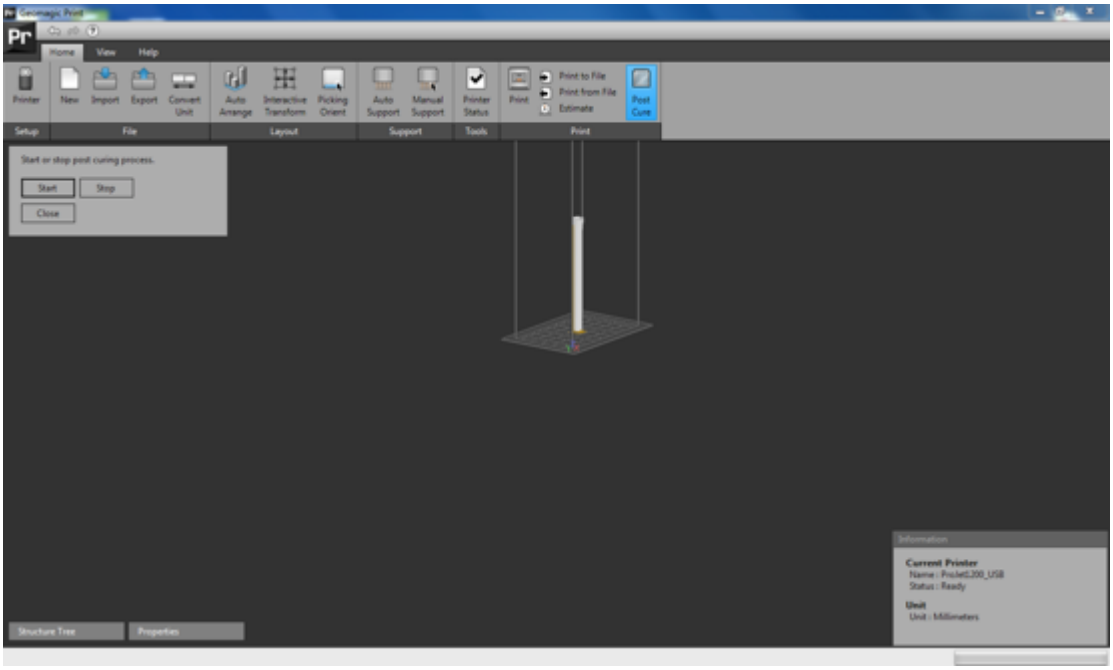

Figure B.9. Starting post curing by clicking “Post Cure” and click START

6) After 10-15 minutes, take the part from Post Curing Chamber. Then the part is READY. You can cut the supports and use your part.

Appendix C. Liquid Tricaine (Ethyl 3 aminobenzoate methanesulfonate) Preparation Protocol

This brief recipe explains how to prepare liquid tricane from powder tricaine (Sigma-Aldrich). Tricaine is used for anesthesia of zebrafish embryo.

400 mg tricaine powder

97.9 ml distilled water

~ 2.1 ml 1M Tris (ph 9). Adjust ph to ~7. (Please note that you can use Sodium Bicarbonate or Sodium Hyroxide. It is important to get ph to ~7.)

Store this solution in the freezer. To use tricane as an anesthetic combine the following in a 250 ml beaker:

4.2 ml tricaine solution

~100 ml clean tank water where the fish lives

During experiments, you can use the table below for different stages of fish.

Length of Fry/Stage	Number of Drops
< 4000 µm	2-3
< 8000 µm	4-6
Juvenile	8-10
Adult	10-12

(Table is taken from Zebrafish Breeding and Imaging Protocol written by Brian Chang)

Appendix D. Publications and Conference Proceedings Resulting from this thesis

Publications

1. Pekkan K., Chang B., **Uslu F. E.,** Mani K., Chen C.Y., Holzman R., " Characterization of zebrafish larvae suction feeding flow using micro-PIV and Optical Coherence Tomography", *Experiments in Fluids,* doi: 10.1007/s00348-016-2197-6, 2016

2. Goktas S., **Uslu F. E.,** Kowalski W., Ermek E., Bradley B.K., Pekkan K., "Time-series Interactions of Gene Expression, Vascular Growth and Hemodynamics during Early Embryonic Arterial Development", *PlosONE,* doi:10.1371/journal.pone.0161611, 2016

3. **Uslu F. E.,** Pekkan K., " Mytilus Galloprovincialis as a smart micro-pump", *Biology Open,* doi: 10.1242/bio.021048, 2016

4. Reiten I., **Uslu F. E.**, Fore S., Pelgrims R., Ringers C., Verdugo C. D., Hoffman M., Kawakami K., Pekkan K., Yaksi E., Jurisch-Yaksi N., "Motile cilia mediated flow improves sensitivity and temporal resolution of olfactory computations", *Current Biology,* doi: 10.1016/j.cub.2016.11.036, 2016

Conference Proceedings

1. Chen C.Y., **Uslu F. E.***, Pekkan K.*, " Three-dimensional characterization of fluid flows induced by micro-objects in microfluidics" , 10th International Symposium on Particle Image Velocimetry – PIV 2013, Delft, The Netherlands, July 1-3, 2013 (Poster Presentation)

2. **Uslu F. E.***, Goktas S., Kowalski W., Bradley B.K., Pekkan K., "Characterization of pulsatile wall shear stress at the vitelline artery during early embryonic development" , 11th International Symposium on Particle Image Velocimetry – PIV 2015, Santa Barbara, USA, September 14-16, 2015 (Oral Presentation)

3. Seyedehsamaneh L., Piskin S., Goktas S., **Uslu F. E.**, Pekkan K.*, "Microstructural analysis of early embryonic aortic arch morphogenesis", Summer Biomechanics, Bioengineering, and Biotransport Conference, Maryland, USA, June 29-July 2, 2016 (Oral Presentation)

4. **Uslu F. E.,** Pekkan K.*, " Flow Dynamics of a smart pump: Mytilus Galloprovincialis", American Physical Society (APS) Division of Fluid Dynamics (DFD) 2016, Portland, USA, November 20 - 22, 2016 (Oral Presentation)

(* presented by)